

A grating interferometer for materials science imaging at a second-generation synchrotron radiation source

(Vom Department Physik der Universität Hamburg im Jahr 2010 als Dissertation angenommene Arbeit)

J. Herzen

A grating interferometer for materials science imaging at a second-generation synchrotron radiation source

(Vom Department Physik der Universität Hamburg im Jahr 2010 als Dissertation angenommene Arbeit)

Julia Herzen

Die HZG Reporte werden kostenlos abgegeben.
HZG Reports are available free of charge.

Anforderungen/Requests:

Helmholtz-Zentrum Geesthacht
Zentrum für Material- und Küstenforschung GmbH
Bibliothek/Library
Max-Planck-Straße 1
21502 Geesthacht
Germany
Fax.: +49 4152 87-1717

Druck: HZG-Hausdruckerei

Als Manuskript vervielfältigt.
Für diesen Bericht behalten wir uns alle Rechte vor.

ISSN 2191-7833

Helmholtz-Zentrum Geesthacht
Zentrum für Material- und Küstenforschung GmbH
Max-Planck-Straße 1
21502 Geesthacht
www.hzg.de

A grating interferometer for materials science imaging at a second-generation synchrotron radiation source

Julia Herzen

Abstract

X-ray phase-contrast radiography and tomography enables to increase contrast for weakly absorbing materials. Recently, x-ray grating interferometers were developed which extend the possibility of phase-contrast imaging from highly brilliant radiation sources like third-generation synchrotron to non-coherent conventional x-ray tube sources. During this work an x-ray grating interferometer was designed and installed at low-coherence wiggler source at the GKSS beamline W2 (HARWI II) of the second-generation synchrotron storage ring DORIS at the Deutsches Elektronen-Synchrotron (DESY, Hamburg, Germany). The beamline is dedicated to imaging in materials science. Equipped with the grating interferometer, it is the first synchrotron radiation beamline with a three-grating setup combining the advantages of phase-contrast imaging with monochromatic radiation with very high flux and a sufficiently large field of view for centimetre sized objects. A simple method was implemented to reliably determine the spatial resolution of the grating-based setup. Furthermore, the quantitative-ness of the setup was analysed by a tomography scan of a specially constructed phantom consisting of chemically well defined fluids. The results of this scan using the new setup are compared to a similar scan carried out using a grating interferometer with a conventional laboratory x-ray tube source. Both measurements demonstrate the accurate determination of the complex refractive index of the different fluids in three dimensions. Examples of radiography on laser-welded aluminium and magnesium joints are presented to demonstrate the high potential of the new grating-based setup in the field of materials science. In addition, the results of tomographic scans of biological soft tissue samples like the brain and heart of a mouse are presented.

Zusammenfassung

Phasenkontrastradiographie und -tomographie mit Röntgenstrahlung wird sehr erfolgreich eingesetzt, um den Kontrast für schwach absorbierende Materialien zu erhöhen. Vor Kurzem wurden Gitterinterferometer entwickelt, die die Phasenkontrastbildgebung von hoch brillanten Strahlungsquellen wie die Synchrotron Quellen der dritten Generation auf nicht kohärente konventionelle Röntgenröhren ausweiten. Während dieser Arbeit wurde ein Röntgengitterinterferometer für den GKSS Wiggler-Messplatz W2 (HARWI II) mit sehr geringer Kohärenz am Speicherring der zweiten Generation DORIS am Deutschen Elektronen Synchrotron (DESY, Hamburg, Deutschland) entworfen und aufgebaut. Der Messplatz ist optimiert für Bildgebung im Bereich der Materialforschung. Ausgestattet mit einem Röntgengitterinterferometer stellt er den ersten Synchrotronmessplatz dar, der einen Drei-Gitter-Interferometer verwendet, um die Vorteile der Phasenkontrastbildgebung mit monochromatischer Strahlung und hohem Fluss mit einem großen Sichtfeld zur Untersuchung von Objekten mit Kantenlängen im Zentimeterbereich zu kombinieren. Ein einfaches Verfahren wurde implementiert, das eine verlässliche Angabe der erreichten Ortsauflösung des Gitterinterferometers ermöglicht. Darüberhinaus wurde die Quantitativität des Aufbaus mit Hilfe einer tomographischen Untersuchung eines selbst-entwickelten Phantoms demonstriert, das aus verschiedenen chemisch gut definierten Flüssigkeiten besteht. Die Ergebnisse dieser Messung am neuen Aufbau wurden mit einer ähnlichen Messung verglichen, die an einer konventionellen Röntgenröhre aufgenommen wurde. Beide Messungen zeigen eindrucksvoll, wie präzise mit diesem Verfahren der komplexe Brechungsindex der unterschiedlichen Flüssigkeiten in drei Dimensionen bestimmt werden kann. Beispiele von Radiographieaufnahmen von Laser-geschweißten Aluminium- und Magnesiumschweißnähten werden präsentiert, um das Potenzial des neuen Gitter-basierten Aufbaus auf dem Feld der Materialforschung zu demonstrieren. Zusätzlich werden die Ergebnisse von Tomographieaufnahmen von biologischen Weichgewebeproben, wie Gehirn und Herz einer Maus, präsentiert.

Acknowledgements

First of all I would like to thank my supervisor Prof. Dr. Andreas Schreyer for the opportunity to work on my PhD thesis in his group at the GKSS Research Centre Geesthacht, for always finding the time for discussions, and for his support during the whole work.

I want to thank Felix Beckmann for mentoring this work, and for introducing me to microtomography. Without your support, Felix, this work would not be possible, and without your unique laughing it would be half the fun it was for me.

Tilman Donath shared the office with me in the beginning of my work before he finished his PhD and went to Switzerland. Thank you, Tilman, for being always there for me, for answering any type of questions, and for your excellent corrections of all writings. I really enjoyed working with you in Hamburg and in Switzerland.

Many colleagues from GKSS contributed to this work. I would like to thank Malte Ogurcek for proof-reading, for helping me setting up the interferometer, and for not giving up to improve the software. Thank you, Lars Lottermoser, for listening to my problems and for your encouragements when everything seemed to go wrong. Thank you Andrew King for your great help as native speaker and for the nice climbing sessions. Torben Fischer shared the office with me for the rest of my time at GKSS. Thank you very much, Torben, for making our office a lively and enjoyable place. I really enjoyed hiking with you in the Alps and I'm looking forward to a next tour. I'd like to thank René Kirchhof, Hilmar Burmester, Thomas Dose, Astrid Haibel, Thomas Lippmann, and Stefan Riekehr for your help and support during my work. Without you the "chauvi box" would never contain enough money for a barbecue and I had never learned the "real men's barbecue"! I'm deeply grateful for the wonderful atmosphere that all of you together with the other colleagues from GKSS and DESY created at the DESY campus.

Furthermore, I would like to thank the colleagues from PSI, Christian David, Oliver Bunk, Martin Bech, Marco Stampanoni and Franz Pfeiffer, who welcomed me warmly during my stay in Switzerland, and introduced me to phase contrast. Thank you very much for your kindness and your help. I'd like to express my special thanks to Franz for agreeing to be a referee of this work and for giving me the opportunity to continue my work in his group at the TU München. Thanks a lot to Martin, who is now my colleague in Munich, for proof-reading of this work.

In particular I want to thank my family, my parents and my sisters Katharina, Elena, and Anna for their support. Thank you so much that you are always there when I need you!

Most of all I want to thank my husband Volker for his patience and support. You are the most important part of my life! I love you!

Contents

1. Introduction	1
2. Instruments and methods	5
2.1. X-ray imaging	5
2.1.1. Absorption contrast	5
2.1.2. Phase contrast	8
2.2. Tomographical principle	9
2.2.1. Radon transform and Fourier slice theorem	9
2.2.2. Backprojection of filtered projections	10
2.3. X-ray sources	11
2.3.1. X-ray tube	12
2.3.2. Synchrotron radiation sources	13
2.3.3. Beamline W2 (HARWI II)	15
2.4. X-ray detector	17
3. Grating-based interferometry	19
3.1. Principle of grating-based imaging	19
3.1.1. The Talbot self-imaging effect	19
3.1.2. Grating interferometer formulas for a phase grating	20
3.1.3. Phase scanning and processing	22
3.1.4. Tomographic reconstruction	26
3.1.5. The case of incoherent illumination - The Lau effect	27
3.1.6. Achromaticity	28
3.2. Experimental implementation of the interferometer	29
3.2.1. Interferometer geometries	29
3.2.2. Mechanical components	31
3.3. Influence of an extended, distant wiggler source	32
3.3.1. Wavefield propagation formulas	32
3.3.2. Simulations of visibility	34
3.3.3. Measurement of visibility	35
3.4. Spatial resolution	36
3.4.1. MTF and spatial resolution	38
3.4.2. MTF calculation using a silicon cuboid	39
4. Quantitative phase-contrast computed tomography of a liquid phantom	45
4.1. Motivation	45
4.2. Calculation of the liquid signals from tabulated data	45
4.3. Measurement at a synchrotron radiation source	47
4.3.1. Introduction	47
4.3.2. Methods and materials	47

Contents

4.3.3. Results and Discussion	49
4.3.4. Contrast-to-noise ratios	50
4.3.5. Conclusions	53
4.4. Measurement at a conventional x-ray tube	55
4.4.1. Introduction	55
4.4.2. Methods and materials	55
4.4.3. Results and Discussion	58
4.4.4. Conclusions	60
4.5. Summary	60
5. Applications	63
5.1. Introduction	63
5.2. Imaging of welded materials	63
5.2.1. Imaging laser-welded T-joints in absorption mode	63
5.2.2. Imaging laser-welded butt-joints in phase-contrast mode	67
5.3. Phase-contrast tomography of biological samples	71
5.3.1. Introduction	71
5.3.2. Tomography of mouse heart and brain	72
5.4. Summary	74
6. Summary and outlook	77
A. Huygens-Fresnel principle and Talbot images	79
B. Alignment procedure	81
C. Grating production	83
D. Publications related to the work	89
Bibliography	91
List of Publications	99

1. Introduction

Synchrotron radiation based x-ray micro computed tomography (SR μ CT) in conventional absorption mode is an established 3-dimensional x-ray imaging method yielding excellent spatial and density resolution in a wide field of applications. In this mode good contrast between different materials inside an object for photon energies greater than 20 keV can only be achieved for highly absorbing elements. To image materials consisting of weakly absorbing elements, especially organic materials, different contrast media or staining procedures are often required. However, such treatments are time consuming, difficult, and in some cases may not be possible or cause structural changes. Detecting the changes in the x-ray wave front caused by the object, in so-called *phase-contrast imaging*, the contrast for weakly absorbing materials can be significantly enhanced using the phase shift introduced to the x-ray wave by the object as a contrast mechanism in the same energy range.

Since no phase information is contained in the measured intensities, different methods have been developed to determine the x-ray phase-shift. The phase-shift information can then be used for 3-dimensional phase-contrast tomographic reconstructions. For a long time, these methods have been practically limited to highly brilliant radiation as it is available at e. g. third generation synchrotron radiation sources. Recently, the development of grating interferometers extend x-ray phase-contrast imaging even to conventional x-ray tube sources. Therefore, grating-based x-ray phase-contrast imaging became feasible also at the second generation synchrotron radiation sources like the storage ring DORIS at DESY (Hamburg, Germany). DORIS provides several orders of magnitude more flux than conventional x-ray tubes of a much lower brilliance than third generation sources (PETRA III). But unlike these sources the beam size is suitable for characterising centimetre sized objects using monochromatic radiation.

The aim of this work was to design and setup a grating interferometer at the materials science beamline W2 operated by GKSS Research Centre Geesthacht at DORIS. In cooperation with PSI, TU München and Karlsruhe Institute of Technology (KIT) the three-grating interferometer for the beamline W2 was built and its functionality was demonstrated. This is the first grating interferometer setup at a second generation synchrotron storage ring utilising three gratings and serves as proof of principle of this geometry using a large and distant source point.

Various examples of different studies will be presented demonstrating the performance of the new setup. In the following, a review of different phase-contrast methods will give the reader a short overview of the existing techniques.

Review of phase-contrast imaging

Since the discovery of x-rays by Röntgen in 1895 their power to non-destructively penetrate objects has been used in many fields including medicine, biology and engineering materials science. The first attempts to expand the optical methods known from the visible light regime to the x-ray regime started with microscopic applications in 1896 as described by J. Kirz *et al.* [55]. Since the 1950's optical components like mirrors or lenses for x-rays have been designed [54] and enhanced that pushed the spatial resolution of x-ray microscopy to below one micrometre. Both, absorption-contrast and phase-contrast imaging methods were developed during the following decades. In 1965 Bonse and Hart succeeded in recording phase-contrast projections using a silicon mono-crystal interferometer [17]. Despite of proof-of-principle experiments with tube sources, for a long time x-ray phase-contrast computed microtomography (PC μ CT) practically was limited to highly brilliant synchrotron radiation sources as reported by Momose *et al.* [70, 71], Beckmann *et al.* [13], Cloetens *et al.* [21], Gureyev *et al.* [40], and Weitkamp *et al.* [96]. Quantitative phase-contrast measurements¹ were only possible using synchrotron radiation, and reported by Bonse *et al.* [16] and Momose *et al.* [69] and verified in a few cases for example in combination with diffraction enhanced imaging (DEI) by Dilmanian *et al.* [27], propagation-based phase-contrast imaging by Nugent *et al.* [76], and phase-contrast microscopy using zone plates by Koyama *et al.* [59], and by McMahon *et al.* [68].

Only a few years ago, the use of low-brilliance x-ray sources like laboratory x-ray tubes for phase-contrast imaging has become feasible and the grating interferometer approach by Pfeiffer *et al.* [80, 82, 83], by Engelhardt *et al.* [29], and by Kottler *et al.* [58] has been demonstrated to provide excellent results for macroscopic specimens.

A review article by Momose [71] gives a detailed overview of all common phase-contrast imaging methods and the recent developments in x-ray phase imaging. Here, a short overview of the methods is presented divided into three main groups: (1.) the direct methods measuring the phase shift (Bonse-Hart interferometer), (2.) the propagation based methods measuring the 2nd derivative of the phase shift, and (3.) the differential methods measuring the 1st derivative of the phase shift by using e.g. the grating-based or the analyser-based method.

The principal of the **crystal interferometer** as used by Bonse and Hart [17] is to separate the incoming beam into two different beams with spatially separated paths. One of the beams penetrates the investigated object and the second serves as a reference beam. By joining both coherent beams behind the sample an interference pattern is produced that can be observed with a detector. By shifting the phase of the reference beam several times by a defined value and analysing the interference pattern in the detector plane, information about the absolute phase-shift of the beam caused by the sample can be obtained. The Bonse-Hart crystal interferometer consists of three parallel lamellae of a fixed spacing cut out from one silicon single crystal. The high sensitivity of this method to phase shifts was demonstrated on several biological specimens [8, 9, 69, 70] visualising density changes of down to about 1 mg/cm³.

¹Meaning quantitative measurement: precise determination of the object-induced phase shift of the x-ray wave front.

This high sensitivity limits the possible applications to only very weakly absorbing materials and at the same time it demands a very high mechanical stability. The sample size is also limited by the separation of the beam paths. Since the silicon crystals serve as monochromators, the flux is significantly reduced, as only a narrow spectral width is selected by the crystals. Thus, the crystal interferometer can only be efficiently used in combination with a synchrotron radiation source providing a high enough beam brilliance.

Propagation-based imaging relies on the fact, that under spatially coherent illumination Fresnel or Fraunhofer diffraction occurs as the beam propagates from the object to the detector [20, 76, 92, 97]. The detector is placed in an increased distance from the object, in contrast to most other kinds of imaging, in which one tries to minimize this distance to avoid blur. Propagation-based methods do not use any optical components, which makes image acquisition very simple.

A simple projection recorded in a certain distance downstream the object gives a so-called *edge-enhanced image* that contains information about the phase gradient, but not a complete phase map of the object [20]. For a complete phase map, several images at varying object-to-detector distances are required from which the phase in each point can be retrieved. Quantitative results from this technique called *holotomography* were reported by Cloetens *et al.* [21]. Holotomography demands spatially coherent illumination and, therefore, is only suitable for third generation synchrotron radiation sources like e. g. the ESRF (Grenoble, France) or PETRA III (Hamburg, Germany).

Analyser-based imaging (ABI) as the name implies makes use of an analyser crystal to generate the contrast. The x-ray beam has to be parallel, which is achieved by collimating it with a crystal using Bragg diffraction condition. Illuminating the sample with the parallel beam the refracted part of it is reflected by the analyser crystal onto the detector. By scanning the analyser crystal different refraction angles can be analysed. The measured refraction angle α is related to the first derivative of the phase front [26]. Additionally, a signal related to the small-angle scattering signal can be extracted from the data [100].

Dilmanian *et al.* [27] presented the tomographic reconstruction of both ABI signals, the first derivative of the phase front and the small-angle scattering signal. The method shows a high phase sensitivity and the potential to provide good contrast even at high x-ray energies (60-90 keV) using the small-angle scattering signal. But this method suffers from the same effect already mentioned in the case of crystal interferometry, which is that the flux is significantly reduced by the monochromatising crystals. Thus, sufficiently short exposure times can only be achieved at a synchrotron radiation source.

The **grating interferometer method** applied in this work uses a beam-splitter grating and an analyser grating to detect the x-ray refraction in the sample. The refraction angle is related to the first derivative of the x-ray phase shift produced by the sample. Like the analyser-based method it additionally provides information that is related to the small-angle scattering signal.

In the case of sufficiently coherent illumination (criteria described by Weitkamp *et al.* [95]) the beam-splitter grating splits the incoming x-ray beam into spatially not separated, over-

1. Introduction

lapping diffraction orders. This overlap leads to interference and causes a periodic intensity pattern in certain distances downstream the beam-splitter grating. A sample refracts the beam producing a transverse shift of the interference pattern perpendicular to the beam direction. This pattern can be detected directly with a high resolution detector or indirectly using an analyser grating.

Recently, a method was developed to expand the use of the grating-based phase-contrast method to polychromatic radiation sources like x-ray tubes or low-brilliance radiation sources like second generation synchrotron sources. By utilising an additional attenuation grating the incoming beam is divided in many small sources of higher transverse coherence as described by Pfeiffer *et al.* [82]. The grating interferometer provides less phase sensitivity than the one of the crystal interferometer, which is advantageous in many cases.

The quantitiveness of the method was demonstrated by a measurement of a specially constructed fluid phantom using the newly design setup. A similar measurement was performed with a conventional x-ray tube source during a three-month research stay at the Laboratory for Micro- and Nanotechnology at Paul Scherrer Institut (PSI) in Switzerland, where the grating-based phase-contrast method was studied on laboratory radiation sources. An approach demonstrating the quantitiveness of the grating-based method in combination with laboratory x-ray tubes was published during this work [49]. As examples, two studies are presented to demonstrate the performance of the new setup: 1. on aluminium and magnesium joints produced by laser welding, representing an important research topic studied at GKSS, and 2. on biological samples being an other important class of specimens characterised using x-ray imaging.

Several SR μ CT studies in absorption mode on different materials were performed at the beamlines W2 and BW2 at DORIS during user support of GKSS internal and external research groups. A selection of publications in reviewed journals, several selected conference proceedings based on these studies, and HASYLAB reports will be presented in the Appendix D and as a list of publications without the reports in the end of the bibliography.

2. Instruments and methods

In the present chapter the theoretical background required for the discussions in the following chapters is presented. For details concerning those aspects which are only discussed very briefly or left out completely, the reader will be referred to the according literature. The first section deals with the basics of imaging including the image formation in absorption and phase-contrast imaging and the explanation of the tomographical principle. The second section of this chapter presents the two different x-ray sources used during this work, the second-generation synchrotron radiation source DORIS at DESY (Hamburg, Germany), and a laboratory x-ray tube at Paul Scherrer Institut (Villigen-PSI, Switzerland). The implications of the two source types for x-ray imaging will be discussed in detail.

2.1. X-ray imaging

In general, x-ray imaging means making the structure of an object visible using x-rays and different contrast mechanisms. As the electromagnetic wave is influenced on its way through the object, the changes can be detected and used for imaging. Measuring the transmitted intensity detects the amplitude decrease of the electromagnetic wave. This is used as contrast mechanism in case of conventional absorption contrast imaging. With interferometric techniques the phase shift can also be detected and used as signal for phase-contrast imaging. Looking to the object's complex refractive index

$$n = 1 - \delta + i\beta \quad (2.1)$$

the absorption is related to the imaginary part β and the phase shift to the real part δ . In the following two sections the signal formation of the two contrasts is explained and the last section deals with the generally valid tomographical principle.

2.1.1. Absorption contrast

Total linear attenuation coefficient

Absorption contrast is based on the fact that the x-ray photons interact with electrons as they propagate through matter. The relation of the *linear attenuation coefficient* μ to the imaginary part β of the complex refractive index n is given by

$$\mu = \frac{4\pi}{\lambda}\beta, \quad (2.2)$$

with λ representing the wave length. In the energy range between 10 keV and 100 keV used in this work there are two main effects contributing to the attenuation: the photoelectric effect, and Compton scattering. They linearly contribute to the total linear attenuation coefficient μ_{tot}

$$\mu_{tot} = \mu_{PE} + \mu_C, \quad (2.3)$$

2. Instruments and methods

with μ_{PE} representing the attenuation coefficient related to the photoelectric effect and μ_C to Compton scattering. The influence of the two effects scales strongly with the photon energy. Two additional effects contribute to the total linear attenuation coefficient: the pair production and the coherent (or elastic) scattering. While the coherent scattering can be neglected at photon energies up to 30 keV the pair production does not occur below 1 MeV and only becomes important for the imaging in MeV range.

Assumption of small sample size and influence of scattering

The relative importance of the photoelectric effect and Compton scattering as competing interactions for tomographic imaging in absorption contrast mode has been discussed by many authors [8, 28, 34, 53]. In the PhD works by Beckmann [8, Chapter 2.4] and by Donath [28, Appendix A] the significance of each effect for imaging in the photon energy range from 10-30 keV is discussed. Both came to the conclusion that for small samples (about 1 cm thick)¹ the photoelectric effect is the dominant effect. Thus, they considered the attenuation coefficient to be approximately equivalent to the photoelectric coefficient ($\mu = \mu_{tot} \approx \mu_{PE}$).

As the samples investigated in this work were in the range of 1-6 cm (in the photon energy range from 22 to 30 keV) we should discuss whether the assumption made by Beckmann and Donath is still valid for our approach. Compton scattering is the dominant interaction of x-rays especially in soft tissue. The interacting photon transfers a part of its energy to a scattering electron and leaves the object in a different angle to the incident direction. In comparison to the photoelectric effect the scattered photons do not contain any 'useful' information about the specimen but decrease the image contrast (by increasing the background signal) when hitting the detector [4].

In the book by Barrett and Swindell [4] the authors describe the influence of scattering on the signal of transmitted intensity projected on the detector. They mention the following parameters, that influence the amount of Compton scattering hitting the detector (see [4, Chapter 11.4]):

1. The Compton scattering increases with sample size, as multiple scattering increases with the sample size
2. It increases with the photon energy
3. It decreases with sufficient collimation of the incident beam, as the incoming beam can already scatter on air and the collimation can stop the scattered part from hitting the detector
4. It decreases with the increasing distance between sample and detector, since x-rays scattered at higher angles (e.g. from multiple scattering) do not hit the detector anymore.

The grating interferometer setup is described in detail in Chapter 3. Its three main differences to the conventional absorption contrast setup described by Beckmann and Donath [8, 28] are

¹The sample thickness influences both, the required photon energy - the thicker the sample, the higher the energy to penetrate it, and the amount of multiple scattering - more material produces more scattering.

larger specimens, the larger distance between sample and detector due to the distance requirements of the Talbot distance, and an absorbing grating in front of the detector acting as anti-scatter grid. Thus, in the case of specimen sizes of $d \leq 1$ cm we should have even less Compton scatter hitting the detector than considered by Beckmann and Donath. According to Barrett and Swindell [4], for increasing sample diameter L (up to 60 mm) the large sample-to-detector distance s in our setup (about 40 cm) will decrease the amount of scattered photons reaching the detector by a factor of $1/(s + L/2)^2$. Using this argument and the fact that an absorbing anti-scatter grid is used in front of the detector, we can conclude that most of the direction-changing scatter will not hit the detector. Therefore this scatter can also be neglected for the grating interferometer setup. The reader is referred to the work by Yao *et al.* [99], who observed the effects of radiation field size, air gap, thickness of the layer of scattering medium and x-ray energy on the amount of scattering.

Neglecting scattering, we can relate the sample composition to the image formed on the detector. In the following we will consider the attenuation coefficient to be approximately equivalent to the photoelectric coefficient ($\mu = \mu_{tot} \approx \mu_{PE}$).

An experimentally determined dependence of the photoelectric part of the linear attenuation coefficient μ_{PE} on photon energy E and atomic number of the material Z outside the absorption edges in the energy range from 10 to 100 keV is

$$\mu_{PE} \approx K \frac{\rho}{m_{at}} \frac{Z^4}{E^3}, \quad (2.4)$$

where K is a constant depending on the atomic shell, ρ the material density, and m_{at} the atomic mass [4].

Beer's law

In case of monochromatic photons the attenuation of a one-dimensional beam in a homogeneous medium follows Beer's law

$$I = I_0 \cdot \exp[-\mu d], \quad (2.5)$$

with I representing the intensity behind a sample of thickness d , I_0 the incoming intensity, and μ the linear attenuation coefficient of the homogeneous medium in [mm^{-1}]. Real samples usually are not homogeneous, so the attenuation coefficient $\mu(y')$ may vary along the beam trajectory through the medium in y -direction and the resulting flux will be given by integration:

$$I(y) = I_0 \cdot \exp \left[- \int_0^y \mu(y') dy' \right]. \quad (2.6)$$

The projected attenuation is then the integral in the exponential function

$$a = \int_0^d \mu(y') dy', \quad (2.7)$$

and when fulfilling the condition $a \approx 2$ the optimum contrast in tomographic reconstructions [37, 38] is reached.

2. Instruments and methods

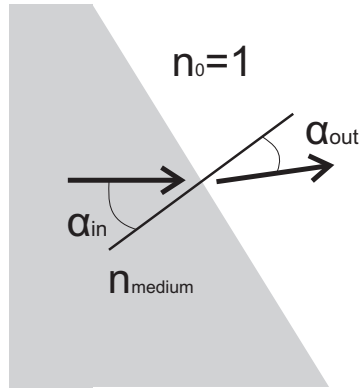


Figure 2.1.: X-ray refraction of an incident beam at a surface of a medium. The refractive index n_0 in free space is unity. The refracted angle α_{out} is for x-rays smaller than the incident angle α_{in} .

2.1.2. Phase contrast

As explained in the introductory chapter the phase-contrast imaging relies on the phase shift caused by a medium, which can be detected indirectly using interferometric methods. No direct measurement of the phase shift of a wave field is possible, because only intensities can be directly detected, and the phase information is lost.

Neglecting the absorption, the phase shift of the electro-magnetic wave traveling through a medium is given by

$$\Delta\Phi = \frac{2\pi\delta d}{\lambda}, \quad (2.8)$$

where δ is the *refractive index decrement* of the complex refractive index n of the medium and d the wave traveling distance. Note that this is the real part of the complex refractive index as explained in the beginning of the Section 2.1. The refractive index decrement δ depends on the x-ray wavelength λ and on the density of the sample as described in the book by *J. Als-Nielsen* [2]:

$$\delta = \frac{r_e \lambda^2 \rho_a f^0}{2\pi}, \quad (2.9)$$

where $r_e = 2.82 \cdot 10^{-15} \text{m}$ is the classical electron radius, ρ_a is the atomic density and f^0 is the real part of the atomic scattering factor in the forward direction. Equation 2.9 is valid far enough from absorption edges (near the absorption edges a dispersion correction f' has to be taken into account, as is described in [2]).

Knowing the incidence angle $\alpha_{in} = 45^\circ$ of the incident x-ray beam to the surface of the medium and its refractive index n_{medium} for x-rays the refraction angle α_r of a non-absorbing

phase object is given by Snell's law as

$$\begin{aligned}
 n_{medium} \sin(\alpha_{in}) &= n_0 \sin(\alpha_{out}) & (2.10) \\
 n_{medium} \sin(\alpha_{in}) &= \sin(\alpha_{out}) \\
 \arcsin(n_{medium} \sin(\alpha_{in})) &= \alpha_{out} \\
 \alpha_r &= \alpha_{out} - \alpha_{in} \\
 \alpha_r &= \arcsin(n_{medium} \sin(\alpha_{in})) - \alpha_{in}
 \end{aligned}$$

with $n_0 = 1$ in vacuum ($n_{air} \approx 1$) and $n_{medium} = 1 - \delta$ for a pure phase object (see Figure 2.1). With δ being in the range of 10^{-8} for x-ray wave lengths of about 0.05 nm the refracted angles α_r are in the range of $-1 \cdot 10^{-5}$ rad. The refraction angles of x-rays are negative, as the index of refraction is less than one. In phase-contrast imaging these refracted angles are detected using interferometric techniques. In our case an x-ray grating interferometer is used.

2.2. Tomographical principle

The principle of tomographical reconstruction from projections is treated in detail by many authors (see e.g. in the book by Kak and Slaney [53], or more mathematically in the book by Natterer [73]). Using the nomenclature from Kak and Slaney² the theoretical background of tomographical reconstruction will be briefly presented here. Please note that all functions written with small letters will represent functions in the real space and the ones with capital letters will describe the Fourier transforms of the real space functions.

2.2.1. Radon transform and Fourier slice theorem

In x-ray computed tomography three-dimensional images of the inner structure of an object are generated from a series of x-ray projections taken from different directions through the rotating object. In case of a synchrotron radiation source the beam can be assumed to be parallel, hence, only the reconstruction for parallel-beam geometry will be explained here (for the case of fan-beam geometry see [53]). The projections are recorded by a two-dimensional x-ray detector as an intensity distribution representing some physical property of the object (e.g. the object's attenuation coefficient for x-rays). This projection is mathematically a Radon transform of the two-dimensional object's function $f(x, y)$. A one-dimensional projection of the function $f(x, y)$ for a certain projection angle Θ can be defined by

$$p_{\Theta}(t) = \int_{(\Theta,t)line} f(x, y) ds, \quad (2.11)$$

where Θ is the projected angle and the line integrals are evaluated along constant

$$t = x \cos \Theta + y \sin \Theta. \quad (2.12)$$

²The constant factors resulting from the Fourier transform (i.e. $1/2\pi$) will be omitted to simplify the equations.

2. Instruments and methods

Using a delta function $p_{\Theta}(t)$ can be rewritten as

$$p_{\Theta}(t) = \int_{-\infty}^{+\infty} \int_{-\infty}^{+\infty} f(x, y) \delta(x \cos \Theta + y \sin \Theta - t) dx dy, \quad (2.13)$$

that is known as the *Radon transform* of the function $f(x, y)$.

Now using the *Fourier Slice Theorem* the Fourier transform of a projection $p_{\Theta}(t)$ can be related to the Fourier transform of the object along a radial line (compare Figure 2.2). The two-dimensional Fourier transform of the object function is given as

$$F(u, v) = \int_{-\infty}^{+\infty} \int_{-\infty}^{+\infty} f(x, y) e^{-j2\pi(ux+vy)} dx dy, \quad (2.14)$$

and the one-dimensional Fourier transform of the projection $p_{\Theta}(t)$ at an angle Θ as

$$P_{\Theta}(\omega) = \int_{-\infty}^{+\infty} p_{\Theta}(t) e^{-j2\pi\omega t} dt, \quad (2.15)$$

where (Θ, ω) are the representation of the coordinates (u, v) after the transform in polar coordinates by $(u, v) = (\omega \cos \Theta, \omega \sin \Theta)$.

The Fourier slice theorem relates now the projection $p_{\Theta}(t)$ and the function $f(x, y)$ in Fourier space:

$$P_{\Theta}(\omega) = F(\omega \cos \Theta, \omega \sin \Theta), \quad (2.16)$$

that means that the Fourier transform $P_{\Theta}(\omega)$ at the angle Θ is equivalent to $F(u, v)$ along a line through the origin, which is rotated by the angle Θ with respect to the x-axis.

The object function $f(x, y)$ can be reconstructed when projections over the angles Θ in the range of π are known. The one-dimensional Fourier transform given by Eq. 2.15 leads to the Fourier transform of the projections $P_{\Theta}(\omega)$, that according to the Fourier slice theorem is related with lines of the two-dimensional Fourier representation of the object function $F(u, v)$ in Eq. 2.14. The object function $f(x, y)$ is given by the inverse Fourier transform:

$$f(x, y) = \int_{-\infty}^{+\infty} \int_{-\infty}^{+\infty} F(u, v) e^{j2\pi(ux+vy)} du dv. \quad (2.17)$$

2.2.2. Backprojection of filtered projections

One possible implementation of the reconstruction of the object's function $f(x, y)$ from the projections is the *backprojection of filtered projections*. The term 'filtered' means that the projections (i.e. the Fourier representations of $f(x, y)$) are filtered by a filter function in the frequency domain before the inverse Fourier transform in Equation (2.17) that can be rewritten in polar coordinates using the substitution $t = x \cos \Theta + y \sin \Theta$ as:

$$f(x, y) = \int_0^{\pi} \int_{-\infty}^{+\infty} |\omega| P_{\Theta}(\omega) e^{j2\pi\omega t} d\omega d\Theta, \quad (2.18)$$

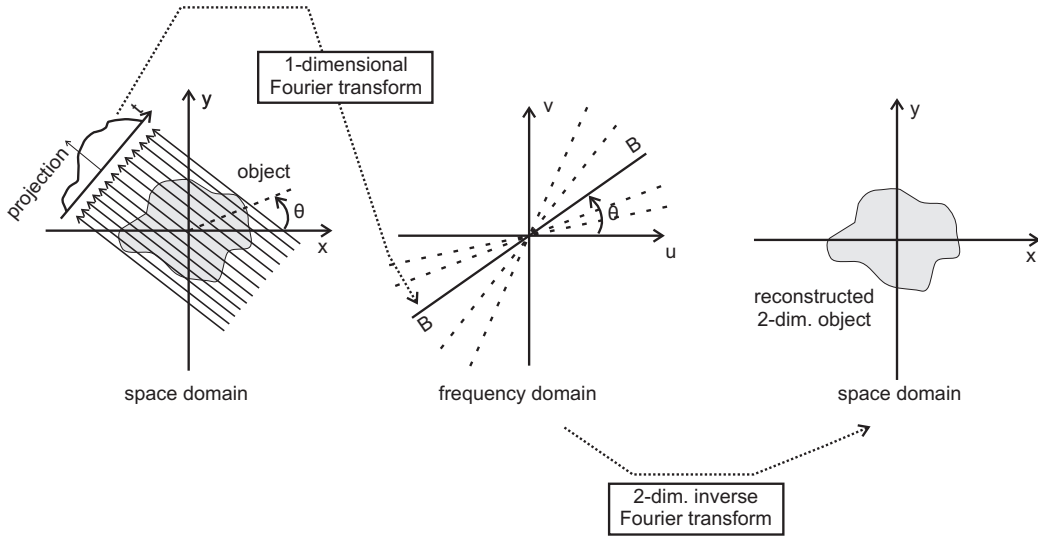


Figure 2.2.: Scheme of a tomographic measurement and reconstruction of a 2-dimensional object. The Fourier Slice Theorem relates the Fourier transform of a projection to the Fourier transform of the object along a radial line (adapted from [53, Chapter 3.2]).

where the frequency filter $|\omega|$ is the essential part of the reconstruction. The inner integral represents the *filtered projection*, and the outer integral is the so called *backprojection*. Algorithms based on this equation are called *filtered backprojection algorithm* as also used in this work.

Different filters were used for the reconstruction of the projections from different contrasts obtained with a grating interferometer, respectively. The filters used for reconstructions in this work will be explained in detail in Chapter 3. In the following the reconstruction according to the Equation (2.18) will be simplified written as:

$$f(x, y) = \int_0^\pi \mathcal{F}^{-1} [Q(\omega)P_\Theta(\omega)] d\Theta, \quad (2.19)$$

with the general filter $Q(\omega)$. In the standard reconstruction using the backprojection algorithm filter functions are used consisting of two parts: the frequency filter $|\omega|$ and an additional function that suppresses the higher frequencies during the reconstruction.

2.3. X-ray sources

In this work two different x-ray sources were used for imaging purposes, a conventional laboratory x-ray tube and a synchrotron radiation source. In the present section the characteristics of the both x-ray sources are described, and their implications for x-ray imaging explained. In the last part the GKSS materials science beamline W2 (HARWI II) is introduced, at which an x-ray grating interferometer was designed and set up during this work.

2. Instruments and methods

2.3.1. X-ray tube

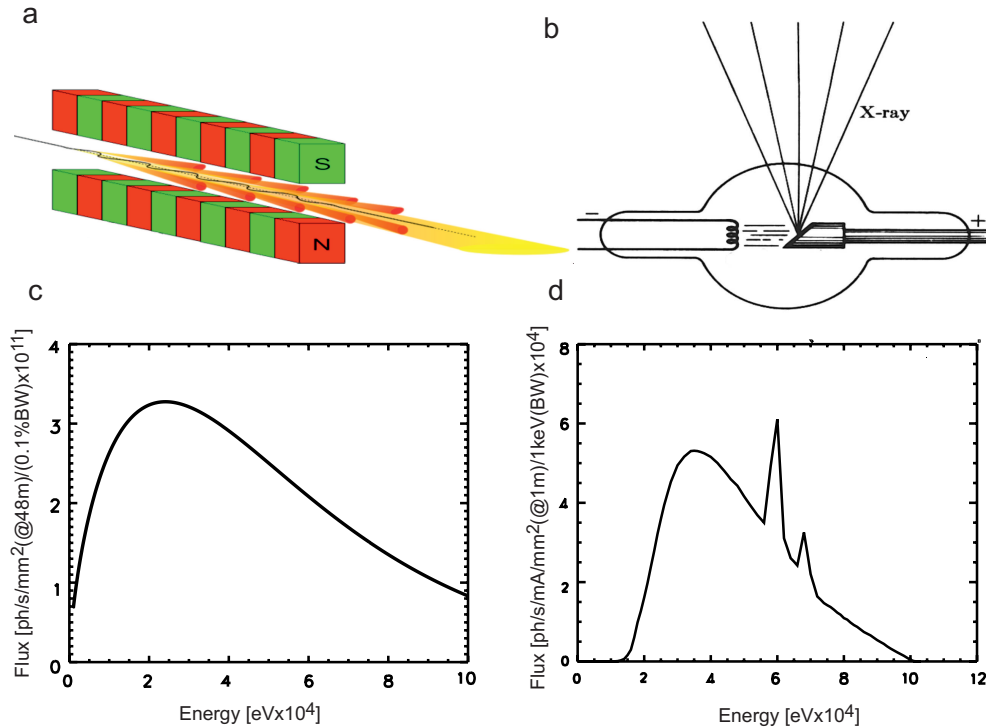


Figure 2.3.: (a) A schematic of a wiggler and (b) of a conventional x-ray tube,³(c) shows the photon flux of the wiggler W2 for 0.1% of the total bandwidth at the sample plane 48 m downstream the beam direction calculated using XOP and the values listed in the Table 2.1, and (d) shows the plot of the photon flux of 1 keV bandwidth at 1 m distance from the source for a 100 kV x-ray tube with tungsten as target. Note that even the band limited synchrotron wiggler flux is ≈ 7 order of magnitudes higher than the x-ray tube flux, the total wiggler flux is about 1000 magnitudes higher than the one of an x-ray tube.

In Figure 2.3(a) a synchrotron radiation insertion device named *wiggler*, and in Figure 2.3(b) a conventional x-ray tube source are schematically shown. It consists of a *cathode* that emits electrons and an *anode* that acts as a target. The electrons are accelerated by the electric field towards the anode and being sharply stopped at the anode produce the so-called *bremstrahlung* in the x-ray regime. Additionally, the characteristic peaks resulting from the fluorescence lines of the target material overlap the broad *bremstrahlung* spectrum. In Figure 2.3(d) the photon flux of 1 keV bandwidth at 1 m distance from the source for a 100 kV x-ray tube with a tungsten target is plotted. Note that the flux of an x-ray tube is about seven magnitudes less than the flux of a wiggler of a synchrotron radiation source for 0.1 % of the total bandwidth at the sample plane 48 m downstream the beam direction as plotted in Figure 2.3(c). The total wiggler flux is about 1000 magnitudes higher than the one of an

³Both schematics were adapted from the web pages: <http://sls.web.psi.ch/view.php/-about/whatis/description/whatis/LightTube1.jpg> and <http://sls.web.psi.ch/-view.php/about/whatis/description/whatis/LightRing1.jpg> [visited November, 30th 2009]

x-ray tube. For this reason x-ray tubes are often not practical for monochromatic imaging applications, because the monochromatic flux of the beam is too low. In case of imaging with polychromatic radiation, the projections suffer from polychromatic artifacts [53], due to the wavelength dependent attenuation coefficients.

Modern x-ray tubes are well established in many fields of application such as medical and biological morphology studies. Their advantages are the easy availability of the sources and the high spatial resolution that can be achieved by minimising the focus size on the target. The spatial resolution in tomograms produced using tube sources is similar to what can be achieved at second generation synchrotron radiation sources (compare the work by Brunke *et al.* [18]). In case of high demands on the density resolution the x-ray tube cannot compete with the high photon flux at the synchrotron sources that is mandatory to improve statistics in the projections.

During this work measurements were performed using a commercially available Seifert ID 3000 x-ray generator at the Laboratory for Micro- and Nanotechnology at Paul Scherrer Institut. The Seifert x-ray generator was operated at 40 kV and 25 mA with a tungsten (W) line focus tube (DX-W8 \times 0.4-L). The target was inclined with respect to the optical axis of 6°, thus the effective source size was 0.8 (horizontal) \times 0.4 (vertical) mm². The grating interferometer used in combination with the x-ray tube is introduced in Section 4.4.

2.3.2. Synchrotron radiation sources

Charged particles like electrons or positrons emit electromagnetic radiation when accelerated. This sort of radiation is called *synchrotron radiation*, when it is produced by a particle-storage ring⁴. In such a ring the particles (electrons or equivalently positrons) are guided by magnetic fields along a circular path. They move in several packages called *bunches* around the storage ring reaching almost the speed of light. Particle-storage rings were initially only built for particle-physics experiments and the synchrotron radiation was an unwanted effect of energy loss, limiting the maximum particle energy. Nowadays dedicated storage rings have been constructed only to produce as much as possible of this sort of radiation. The photons emitted are very focussed in forward direction, making these rings the most brilliant artificial x-ray photon sources currently available. X-ray free-electron lasers (XFEL) in hard and soft x-ray regime, which will provide several orders of magnitude more flux than the synchrotron storage rings, are already available now. As the name implies, for the first time they produce very short-pulsed laser light in the x-ray regime.

Several parameters are used to characterise synchrotron radiation storage rings, of which only the most important are mentioned here. More details can be found in the book by Wille [98].

As shown schematically in Figure 2.3(a) the synchrotron radiation is emitted as an extremely forward-focussed cone due to an effect of relativity (compare [98, Chapter 2.2]), that can be characterized by its opening angle in the horizontal plane by $2\nu_x$ and vertical plane

⁴The name *synchrotron* came from the particle accelerator rings that worked with magnetic fields synchronised with the particle acceleration.

2. Instruments and methods

by $2\nu_z$. The two parameters can be approximately given by

$$\nu_x \approx \gamma^{-1} \quad (2.20)$$

$$\nu_z \approx 0.565\gamma^{-1}\left(\frac{\lambda}{\lambda_c}\right)^{0.425} \quad (\text{for } 0.2 < \frac{\lambda}{\lambda_c} < 100), \quad (2.21)$$

where $\gamma = E_e/m_e c^2$ is the Lorentz factor with E_e the energy of the electrons in the storage ring and $m_e c^2 = 511$ keV the rest energy of the electrons. λ_c is the critical wavelength dividing the photon spectrum in two parts of equal power and is given by

$$\lambda_c[\text{\AA}] = 5.59 \frac{R[\text{m}]}{E_e[\text{GeV}]}, \quad (2.22)$$

with R being the radius of the storage ring given in meters. The half opening angle in the horizontal plane of the photon beam of a 4 GeV storage ring with a $\gamma = \frac{4 \cdot 10^6[\text{keV}]}{511[\text{keV}]} \approx 7828$ amounts to 0.12 mrad = 0.007° . The small divergence of the photon beam makes the synchrotron radiation the brightest x-ray source and thus desirable for many fields of applications.

The intensity of the synchrotron radiation can be further amplified by using so-called *insertion devices* like *wigglers* or *undulators*. These devices are periodic magnetic structures that cause oscillations of the electron (or positron) beam when placed in straight sections of the storage ring. They are described by a dimensionless quantity K as

$$K = \frac{\lambda_0 B_0 e}{2\pi m_e c}, \quad (2.23)$$

where $\lambda_0[\text{mm}]$ is the field period of the magnetic field and $B_0[\text{T}]$ the maximum magnetic flux. The maximum angle of the motion of the particle during its oscillation around the electron orbit is given by

$$\nu_\omega = K\gamma^{-1}. \quad (2.24)$$

The distinction between wigglers and undulators is made using the parameter K . Devices with $K > 1$ are called wigglers, and those with $K < 1$ undulators. That means that the divergence of the photon beam is higher when using a wiggler. The advantage of a higher divergence for imaging is the resultant larger maximum beam size that allows the imaging of centimetre sized objects.

Undulators emit partially coherent radiation with a narrow energy spectrum due to the only weak oscillation of the particles in the magnetic field. In contrast, wigglers produce a broad energy spectrum, where coherency is lost due to the higher ν_ω . Typically a small energy band is selected from the spectrum by single crystals using Bragg diffraction. The monochromator principle and the characteristics of the wiggler beamline W2 used in this work are presented in Section 2.3.3. Figure 2.3(c) shows a plot of the photon flux of the wiggler W2 at the sample position through an aperture of $1\text{mm} \times 1\text{mm}$ calculated using the software XOP⁵. For more details to the calculations see Section 2.3.3.

⁵XOP 2.3 - X-ray Oriented Programs. The software is available online at: <http://ftp.esrf.eu/pub/scisoft/xop2.3/> [visited January, 17th 2010] and the parameters are listed in Table 2.1

The measurements performed at a synchrotron radiation source and presented in this work were carried out at the second generation storage ring DORIS III at the Deutsches Elektronen-Synchrotron (DESY, Hamburg, Germany). It is operated with positrons (e^+) of energy 4.45 GeV in usually 5 bunches circulating in a ring with a circumference of approx. 300 m and a ring current decaying exponentially from 140 mA to 90 mA within one runtime of about 8 hours.

2.3.3. Beamline W2 (HARWI II)

The beamline W2 is the wiggler beamline that has been equipped with a grating interferometer during this work. It is situated at the storage ring DORIS III and operated by the GKSS Research Centre Geesthacht (GKSS) in cooperation with DESY since 2006 as a high energy materials science beamline. The technical details of the beamline have been published by Beckmann *et al.* [14, 11] and in the book by Reimers, Pyzalla, Schreyer, and Clemens [86]. Figure 2.4 shows a schematic of the beamline consisting of the wiggler, an optics hutch with the monochromator tank, the 1st experimental hutch with the setups of tomography and diffraction experiments, the 2nd experimental hutch with a high pressure cell operated by the Geoforschungszentrum Postdam (GFZ), and the control hutch.

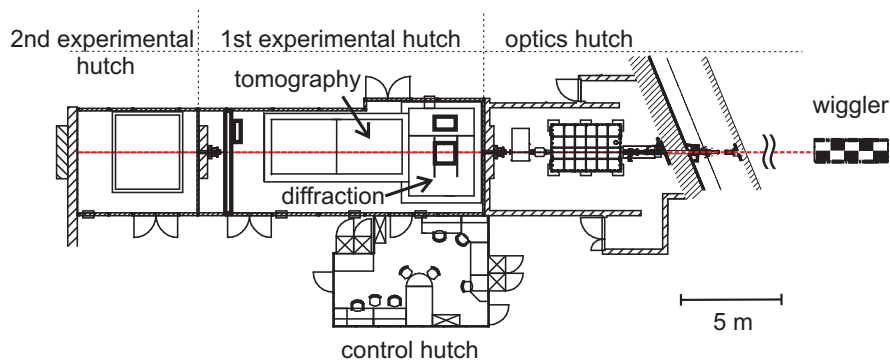


Figure 2.4.: Schematic of the beamline W2 consisting of the wiggler, optics hutch with the monochromator tank, the 1st experimental hutch with tomography and diffraction setups, and the 2nd experimental hutch with a high pressure cell operated by Geoforschungszentrum Potsdam. The red line represents the beam path.

Two monochromator setups, one with horizontal and one with vertical beam reflection, are installed at W2. The horizontal monochromator is used for diffraction applications. The vertical one provides a wide beam up to 70 (horizontal) x 8 (vertical) mm² making it particularly suitable for tomographic imaging. Different pairs of crystals are used in Laue-Laue and Laue-Bragg geometry to vary the photon energy [50, 66]. The monochromator concept of the beamline W2 is presented in detail by Beckmann *et al.* [10].

The main characteristics of the beamline W2 are listed in the Table 2.1⁶, which are used for the spectrum calculation shown in Figure 2.3(c). The only optical components considered in

⁶Values from HASYLAB homepage, visited January, 19th 2010

2. Instruments and methods

Table 2.1.: Source characteristics of the beamline W2.

Parameter	Unit	
DORIS III		
Positron Energy	GeV	4.45
Positron Current	mA	140-70
Source size (hor.) σ_x	mm	1.797
Source size (vert.) σ_z	mm	0.514
Wiggler W2		
Total length	m	4
Period length	mm	110
Number of periods		35
Minimal gap	mm	14
Peak field B_0	T	1.98
K		20.3
Critical energy	keV	26.7
Filters		
Carbon	mm	3(permanent)/7 (variable)
Copper	mm	1.0/2.0
Monochromator		double-crystal Si-111 (bent Laue) and Si-111 (Bragg), in vacuum
Beam size (max.)	mm	70 (horizontal) x 4 (vertical)
Energy range	keV	16 - 150
Integrated flux ⁷	ph/s/mm ²	2.2×10^{15}
Flux at 20 keV ^{7, 8}	ph/s/mm ² /(0.1%BW)	1.6×10^{10}
Flux at 30 keV ^{7, 8}	ph/s/mm ² /(0.1%BW)	7.5×10^{10}

the plot were the monochromator crystals. Due to the Laue geometry the two 0.7 mm thick silicon (111) crystals diminish each the flux by a factor of 0.5, when assuming no bending. By bending the crystals significantly more flux can be provided as the energy bandwidth increases with larger crystal curvature. All the additional influences that strongly depend on the photon energy were not considered in the plot. The carbon filters (10 mm in total) reduce the transmitted flux by a factor of 0.4 at 20 keV and by 0.6 at 30 keV (this is the photon energy range used during this work). As the last effect the absorption inside the monochromator silicon crystals can be considered with a factor of 0.25 at 20 keV and 0.5 at 30 keV to the transmitted flux. The flux for 20 keV and for 30 keV is separately calculated using these values and then listed in the Table 2.1.

As the wiggler beamline W2 operates at the second-generation storage ring DORIS III, its source divergence is much larger compared to that of newer third-generation synchrotron radiation sources like PETRA III with undulator sources. This fact, and the millimetre-sized source point in the wiggler, have two important consequences: 1.) It makes the beamline extremely interesting for applications on centimetre-sized objects, and 2.) it leads to a very low spatial coherence in the x-ray beam, that makes direct phase-contrast imaging (compare the phase-contrast review in the introductory chapter) practically impossible. The beamline can be treated like an extended incoherent x-ray source (like a conventional x-ray tube) and phase-contrast methods designed for this type of sources can be considered for W2. The phase-contrast method using a three-grating interferometer has been used with incoherent sources (x-ray tubes and neutrons [30, 39, 82, 95]) and was redesigned for the beamline W2, meaning that the grating geometries had to be adjusted to the beamline. Additionally, due to

⁷Calculated with XOP (see text).

⁸Flux at sample position through a $1 \times 1\text{mm}^2$ aperture at 100 mA ring current and a wiggler gap of 20 mm. Influence of additional optical components is considered (for details see text).

the large source point a compromise between a high sensitivity of the interferometer at high intergrating distances and the image blur by the beam divergence at larger sample-to-detector distances had to be found. This fact will be discussed in detail in Chapter 3.

2.4. X-ray detector

The same x-ray detector was used as for the conventional absorption-contrast imaging at the beamline W2. The x-ray camera consisted of a luminescence screen, a commercial Nikon lens, and a Finger Lake Instruments PLO9000 CCD camera.

As a luminescence screen CdWO_4 crystal $587 \mu\text{m}$ thick and covered by a black lacquer (see [28] for more details) was used. Commercial Nikon lenses operated in retro-focus position (facing the luminescence screen with the side, that is normally facing the CCD chip) with focal lengths of 50 mm or of 35 mm were used for different magnifications. The amount of light and the resolution can be controlled by the aperture inside the lens.

A Finger Lake Instruments PLO9000 CCD camera with an active area of 3056×3056 pixels with a pixel size of $12 \mu\text{m}$ was used. The CCD camera uses an internal iris shutter to protect the CCD from illumination during the read out. The CCD is cooled down to -15° by an internal Peltier element during the operation. In full frame operation the CCD digitalises with 16 bit at 10 MHz (true dynamic range ≈ 13 bit). The lowest exposure time can be chosen to 0.05 seconds, lower exposure times cannot be achieved, since the iris shutter is too slow. The typical exposure times were between 0.1 and 15.0 seconds with a full frame read-out time of 1 second. Figure 2.5(a) shows a schematic of the x-ray detector consisting of a luminescence screen (CdWO_4), a lens (Nikon, 50 mm) and a CCD detector (Fingerlake Instruments PLO9000). Figure 2.5(b) shows a plot of a quantum efficiency of the CCD chip of the FLI camera and the emitted intensity of the luminescence screen plotted against the wavelength in the visible light regime with a peak quantum efficiency of of the CCD at about 68% at ≈ 550 nm wavelength and a peak of the emitted intensity of the CdWO_4 screen of about 48% at ≈ 470 nm. This two peaks fit well in the range of 500 nm.

2. Instruments and methods

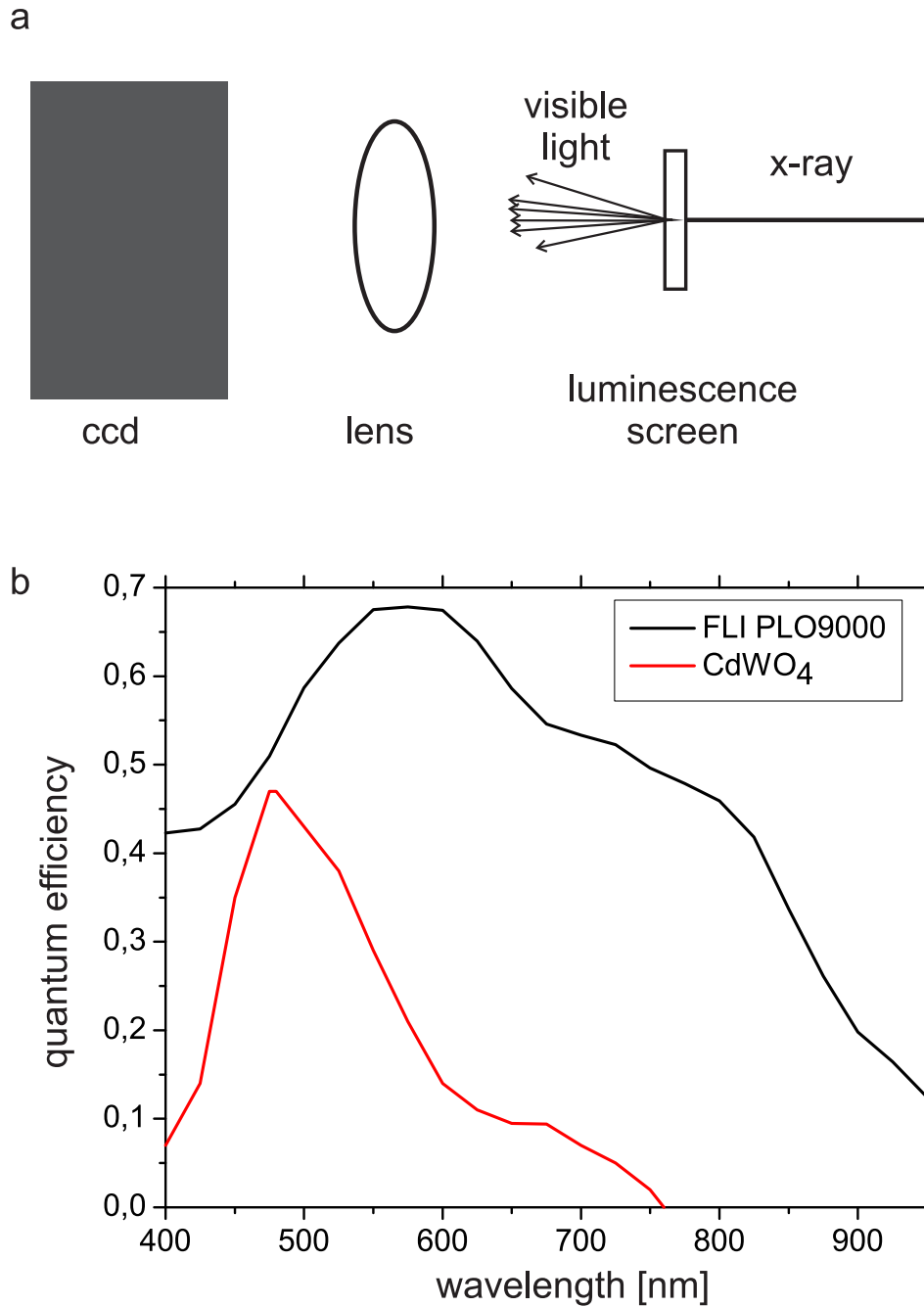


Figure 2.5.: (a) Schematic of the x-ray detector consisting of a luminescence screen (CdWO_4) that converts x-rays into visible light, a lens that projects the object on the CCD detector (FLI PLO9000). (b) The quantum efficiency for the visible spectrum of the CCD chip KAF-09000 used in the Finger Lake Instruments PLO9000 CCD camera and the emission intensity of the luminescence screen CdWO_4 . The curves were reproduced from the manufacturer homepages.

3. Grating-based interferometry

This chapter describes the grating interferometer for phase-contrast imaging that was designed and set up at the beamline W2 during this work. Section 3.1 gives a general introduction into the principle of grating-based interferometry. The Talbot self-imaging effect being the main phenomenon behind the grating-based phase-contrast imaging, the signal-formation and the image-acquisition process are explained in detail. Additionally, the image processing chain for calculating a projection and the 3D reconstruction of the three different signals (absorption, phase-contrast, and dark-field signal) from projections using *filtered backprojection algorithms* are described. In Section 3.2 the experimental implementation of the interferometer designed during this work is presented showing all mechanical components. Section 3.3 points out the difference of this setup at the 2nd generation storage ring DORIS to the setups at 3rd generation synchrotron radiation sources and at laboratory x-ray tubes. In the last Section 3.4 a new method is introduced to determine the spatial resolution in the absorption and phase-contrast projections recorded with the interferometer setup by calculating the *Modulation Transfer Function* (MTF) of the edge of a silicon cuboid.

3.1. Principle of grating-based imaging

3.1.1. The Talbot self-imaging effect

In the early 19th century Henry Talbot observed a phenomenon of visible light passing through periodic structures like gratings that he described in his work *Facts relating to optical science*. [93]. The periodically modulated light wave seemed to repeat itself at certain distances behind the grating in the propagation direction. The phenomenon is known as the *Talbot self-imaging effect* and is described in case of visible light in more detail for example by Talbot himself [93], and by Paturski [78].

Simply speaking, when a periodical object, like for example a silicon grating of a certain pitch, is illuminated by coherent light, the wave front will be changed by this object. These changes will lead to interference pattern in discrete distances downstream the beam which can be measured as a variation of intensity of the same periodicity as the object that produced them, in our case the silicon grating. So, the Talbot self-imaging effect is based on the Huygens-Fresnel principle¹ and the wave propagation through free space, and can be observed at any coherent light source with any periodic structure changing the wave front.

In general, self-imaging means image formation without any lens or other optical component between the object and its image. Strictly speaking, only the case of self-imaging of monochromatic, coherent plane-wave illumination of a periodic object is called the Talbot

¹The Huygens-Fresnel principle states that a wave front can be at any point considered as a sum of spherical waves, which can be integrated to a resulting wave front.

3. Grating-based interferometry

effect. The discrete distances between the periodic structure and the images are the *Talbot length* d_T , or an integer multiple of it

$$d_T = 2mp^2/\lambda, \quad (3.1)$$

with the period of the one-dimensional periodic object p , the wavelength λ , and an integer $m = 1, 2, 3, \dots$. It can be shown that the discrete Talbot lengths can be calculated using the Huygens-Fresnel principle by propagating a periodically modulated wave front as is shown in Appendix A. In 1967 Montgomery [72] found that the classical Talbot effect is only a special case in a larger class of self-imaging effects. The Talbot effect demands a periodic object, while Montgomery showed that quasi-periodic structures also produce self-images. In the work by Lohmann *et al.* [65] it is discussed in detail that the Talbot images represent only a subset of the Montgomery images, and two cases of self-images were presented: The images at distances $d = md_T$, (m is an integer) that we call classical Talbot images, and self-images occurring at distances $d = (m/n)d_T$, where m and n are small integers, e.g. $(m/n) = 1/2, 1/4, 2/3$. These images are called fractional Talbot images and enormously increase the number of usable self-image planes for different applications. The image does not replicate the object (here a periodic grating) at every fractional Talbot distance - it strongly depends on the shape and the kind of the grating, as well as on the fraction (m/n) . For example, self-images of the object with a doubled period can be observed at certain conditions, that also can be used as a fractional Talbot image for interferometric purposes. A series of fractional Talbot (or fractional Montgomery) distances are listed in the work by Lohmann *et al.* [65].

So far, we only looked at coherently illuminated periodic or quasi-periodic structures. The self-imaging effect under incoherent illumination is first described by Lau [63] in 1948 in case of visible light. He used an additional absorption grating that he placed in proper distance in front of a periodic structure. This additional grating produced an array of mutually incoherent thin line sources out of one extended incoherent source, that caused an overlap of the interference patterns produced by two neighbor line sources illuminating the periodic structure. This overlap increased the total intensity in the self-image plane.

The self-imaging effect using incoherent illumination got the name *Lau effect* and is used in many different applications, e.g. in imaging with a grating interferometer at low-coherence sources as in the present work. A very thorough literature review of the historical background of the Talbot effect (classical and fractional), and of the Lau effect giving an overview over the preceding publications can be found in the review of the self-imaging phenomena by K. Patorski [78]. For the sake of simplicity, the general principle of the grating-based phase-contrast imaging will be introduced using the example of the fractional Montgomery effect in Section 3.1.2, i.e. the case of coherently illuminated phase gratings. The more complicated case of the Lau interferometry at fractional Talbot distances, i.e. the case of non-coherently illuminated phase grating, as used in this work, will be explained later in the Section 3.1.5.

3.1.2. Grating interferometer formulas for a phase grating

Plane wave case Compared to the previous section, where the Talbot effect in general was explained, this part deals with a very specific case of the self images downstream a phase grating. For the following explanations an ideal phase grating is assumed with a duty cycle

3.1. Principle of grating-based imaging

of 0.5, i.e. only the half of the grating period produces a phase shift and the other half does not change the incoming wave.

In case of a monochromatic parallel-beam illumination and for a phase grating G_1 with a period p_1 , self images are produced at the fractional Talbot distances

$$D_n = n \frac{p_{1,e}^2}{2\lambda}, \quad (3.2)$$

with the Talbot orders $n = 1, 2, \dots$ and the period of intensity modulation $p_{1,e}$ behind G_1 , we refer to as the effective period of grating G_1 , and which is given by

$$p_{1,e} = p_1/\eta, \quad \text{with} \quad \begin{cases} \eta = 1, & \text{for an absorption grating or a } (\pi/2)\text{-shifting phase grating} \\ \eta = 2, & \text{for a } \pi\text{-shifting phase grating as considered here.} \end{cases} \quad (3.3)$$

The phase gratings are produced such that the stages introduce a phase shift of π to the incoming wave front at a certain wavelength (for more details see the Appendix C) splitting the incoming beam into the $\pm 1^{\text{st}}$ diffraction orders. For all other wavelengths the phase shift deviates from π . The consequences of this effect on the self images are discussed in Section 3.1.6. When the beam propagates from the grating G_1 to the detector, interference pattern can be observed at the Talbot distances.

For a phase grating, the self images occur at odd fractional Talbot orders ($n = 1, 3, 5, \dots$) and at even fractional Talbot orders ($n = 2, 4, \dots$) for an absorbing grating. Due to the similarity to the beam-splitting crystal interferometer the grating G_1 is also called *beam-splitter grating* as it splits the incoming beam into diffraction orders.

To detect the phase shift introduced by the sample to the incoming wave the transverse changes of the intensity pattern of the self image have to be detected. A non-absorbing phase object introduces a phase shift to the incoming plane wave front. This change means a deviation of the wave front propagation direction by an angle α . The interference pattern is shifted transversely by αD_n , with the intergrating distance D_n .

Working with a π -shifting phase grating the intensity pattern behind the G_1 has the period $p_{1,e}$, that is half of the period p_1 (see Eq. 3.3). A typical phase grating has the period $p_1 = 4 \mu\text{m}$ that leads to a period $p_{1,e} = 2 \mu\text{m}$ of the resulting interference pattern. To detect changes in a $2 \mu\text{m}$ pattern one can either use a very high-resolving detector or an additional grating in combination with a phase-stepping technique and a standard CCD detector. The second grating G_2 must be an absorbing grating that matches the period of the observed pattern

$$p_2 = \frac{p_1}{2} = p_{1,e}. \quad (3.4)$$

Spherical wave case The parallel-beam geometry is never achieved in a real experiment as we always deal with sources of a finite distance. For the calculation of the grating geometries the magnification factor must be taken into account when designing the grating periods (see Figure 3.1 showing a spherical two-grating setup). Thus, in case of spherical waves the fractional Talbot distances rescale with a magnification factor M , which can be calculated

3. Grating-based interferometry

from the source-to- G_1 distance l , and the G_1 -to- G_2 distance D_n by

$$M = \frac{l + D_n}{l} . \quad (3.5)$$

Here should be mentioned that we neglect the local curvature of the wave front and consider it as a plane wave scaled by the magnification factor M . The rescaled Talbot distances d_n are determined by

$$d_n = M D_n , \quad (3.6)$$

representing a geometrically magnified projection of G_1 onto G_2 illuminated by a source focal point. In the following the distance d_n will be simply denoted as d , and the subscript n will only be used in cases, where the meaning of d is not clear.

The period p_2 of the absorbing analyser grating G_2 , which is chosen to match the period of the resulting interference pattern produced by the phase grating must be equal to the period of the self images, which also has to be scaled by the magnification factor M

$$p_2 = p_{1,e} = M \frac{p_1}{\eta} . \quad (3.7)$$

By means of a phase-stepping scan a precise detection of the interference pattern can be achieved, i.e. either the grating G_2 or the grating G_1 is shifted in several steps parallel to the other grating and images are recorded at each position.

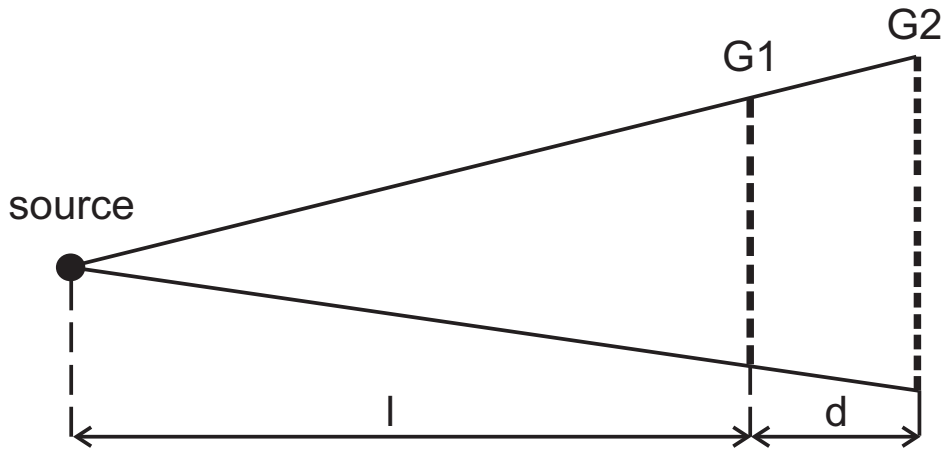


Figure 3.1.: Schematic of a spherical wave grating interferometer setup. G_1 : phase grating, G_2 : analyser grating.

3.1.3. Phase scanning and processing

The changes in the interference pattern are analysed for each detector pixel separately. The intensity oscillations during a phase-stepping scan in each detector pixel (χ_x, χ_y) can be

3.1. Principle of grating-based imaging

written as a Fourier series

$$I(\chi_x, \chi_y, x_g) = \sum_{m=0}^{\infty} a_m(\chi_x, \chi_y) \cos(mkx_g + \phi_m(\chi_x, \chi_y)), \quad (3.8)$$

with the amplitude coefficients a_m , the corresponding phase coefficients ϕ_m , with $k = 2\pi/p_2$, the period p_2 of the grating G_2 , and x_g the grating position during the phase-stepping scan. The first order cosine from Eq. 3.8 is a good approximation of the intensity oscillations in our case.

$$I(\chi_x, \chi_y, x_g) = a_0(\chi_x, \chi_y) + a_1(\chi_x, \chi_y) \cos\left(\frac{2\pi x_g}{p_2} + \phi_1(\chi_x, \chi_y)\right), \quad (3.9)$$

with a_0 representing the averaged value of the cosine function, ϕ_1 the transverse shift, and a_1 the amplitude of the first order cosine. In the case of very small source sizes possibly higher order cosines have to be taken into account (for more details see [6, Chapter 2.4]).

To determine the coefficients a_0 , a_1 and ϕ_1 one can fit a cosine function using a least square fitting function. But the more convenient way is to use a *Fast Fourier Transform* (FFT) algorithm for discrete Fourier analysis, as also done during this work.

The quality of a grating interferometer is described by the visibility of the interference pattern. The visibility is defined by

$$V = \frac{(I_{max} - I_{min})}{I_{mean}}. \quad (3.10)$$

As we calculate the Fourier coefficients for the signal processing, we use the ratio of these coefficients to determine the visibility as

$$V = \frac{2a_1}{a_0}. \quad (3.11)$$

In real measurements the beam profile is never absolutely homogenous and can change over time. To correct for that, a reference phase-stepping scan is performed without the sample in the beam. From analysis of the data from the reference scan, in the same way as described above, one obtains the coefficients a_0^r, a_1^r and ϕ_1^r denoted with the superscript ' r ' for the reference image. The coefficients obtained from sample images will be marked with the superscript ' s '.

The transmission through the sample is given by the averaged intensities a_0 by

$$T = \frac{a_0^s}{a_0^r}. \quad (3.12)$$

The transverse shift of the interference pattern is proportional to the phase shift of the first Fourier component

$$\phi_1 = \phi_1^s - \phi_1^r. \quad (3.13)$$

As the last signal, the so-called *dark-field signal* described by the change in visibility from Equation 3.10, here defined as the ratio of the first order amplitude a_1 relative to the average

3. Grating-based interferometry

value a_0 , is given by

$$V = \frac{V^s}{V^r} = \frac{a_0^r a_1^s}{a_0^s a_1^r}. \quad (3.14)$$

Figure 3.2 shows the intensity in one pixel during a phase-stepping scan with and without the sample. The Fourier coefficients obtained from a FFT of the signal provide the three signals described above. More details on the image processing chain can be found in the works by Pfeiffer *et al.* [79], Weitkamp *et al.* [95], and in the PhD thesis by M. Bech [6].

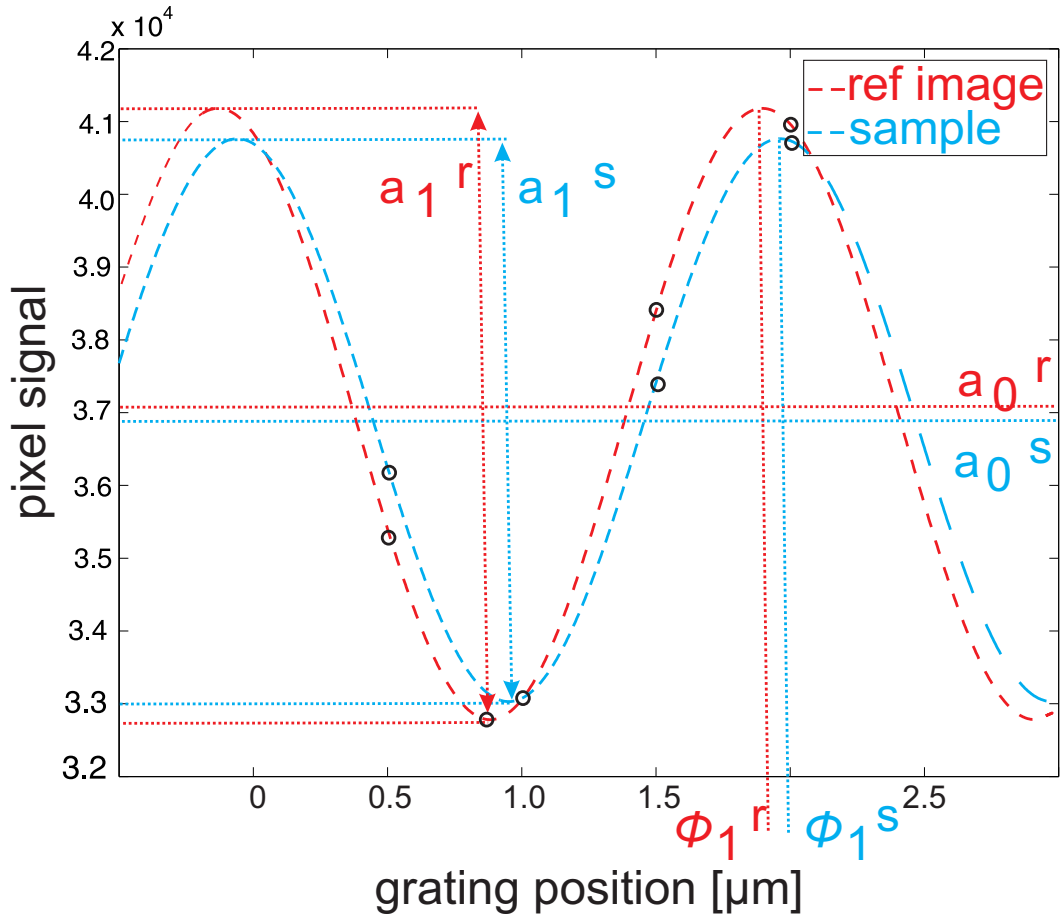


Figure 3.2.: The signal of one pixel during a phase-stepping scan. (red) Intensity without a sample and (blue) intensity with sample. From the quantities a_0^r , a_0^s , a_1^r , a_1^s , and ϕ_1^r and ϕ_1^s represent the zeroth and first order Fourier coefficients, that are used to calculate the three different signals of the grating interferometer.

Relation of the projection signals The signal in Eq. 3.12 is the conventional x-ray attenuation which is associated with the imaginary part of the complex refractive index β and is measured in form of the linear attenuation coefficient μ of the object. A combination of the Radon transform of the object with Beer's law describes the transmission projection in the

3.1. Principle of grating-based imaging

plane $z = z_0$ (see the Equation (2.15))

$$T^\Theta(x') = \exp \left[- \int_0^d \frac{4\pi}{\lambda} \beta(x', y') dy' \right] = \exp \left[- \int_0^d \mu(x', y') dy' \right], \quad (3.15)$$

where $\mu(x', y') = 4\pi/\lambda \cdot \beta(x', y')$ is the linear attenuation coefficient from Equation (2.6) expanded to two dimensions, λ is the x-ray wavelength, and (x', y', z) belong to a coordinate system, which is defined by rotating the system (x, y, z) around the z -axis by the projection angle Θ . Integration is carried out along the x-ray path over the extension of the sample of diameter d . Note that the variable z was omitted to simplify the writing. The quantity a_0 from Equation 3.12 corresponds to the transmitted projection as one would measure it with a standard x-ray radiography in absorption mode.

The signal in Eq. 3.13 is the phase shift $\Phi(x, y)$ introduced by the object to the incoming wave field and resulting in a refraction of the beam by an angle α . This angle is correlated with the first derivative of the phase shift $\partial\Phi/\partial x$ by

$$\alpha = \frac{\lambda}{2\pi} \frac{\partial\Phi}{\partial x}, \quad (3.16)$$

with the x-ray wavelength λ . The transverse shift $\phi_1 \in]-\pi, \pi]$ from Equation 3.13 is related to the lateral shift of the interference pattern in a given pixel by

$$S(\chi_x, \chi_y) = \phi_1(\chi_x, \chi_y) \frac{p_2}{2\pi}, \quad (3.17)$$

and to the angular refraction by

$$\alpha(\chi_x, \chi_y) = \frac{S(\chi_x, \chi_y)}{d} = \frac{\phi_1(\chi_x, \chi_y)}{d} \frac{p_2}{2\pi}. \quad (3.18)$$

Analog to the absorption-contrast projection in Eq. 3.15, we measure the differential phase-contrast projection of refraction angles [77]

$$\alpha^\Theta(x') = \frac{\lambda}{2\pi} \frac{\partial\Phi^\Theta(x')}{\partial x'} = \int_0^d \frac{\partial\delta(x', y')}{\partial x'} dy', \quad (3.19)$$

where $\Phi^\Theta(x') = 2\pi/\lambda \int_0^d \delta(x', y') dy'$ is the spatially dependent, total relative phase shift of the x-ray wave front during its propagation through the sample.

Using the Equation 3.16 the differential phase shift can be written as

$$\frac{\partial\Phi(\chi_x, \chi_y)}{\partial x} = \frac{2\pi}{\lambda} \alpha(\chi_x, \chi_y) = \frac{p_2}{\lambda} \frac{\phi_1(\chi_x, \chi_y)}{d}. \quad (3.20)$$

The total phase shift Φ can be determined by integration. In the following, the image formed by ϕ_1 will be called *differential phase-contrast image*.

The signal in Eq. 3.14 is described in detail by Pfeiffer *et al.* [79], and by M. Bech [6] as a reduction of the visibility of the interference fringes caused by a beam spread from small angle scattering in the sample and is related to the visibility obtained from Equation 3.10.

3. Grating-based interferometry

This spread is connected to a material specific *linear diffusion coefficient* ϵ , depending on the total scattering width σ and the sample thickness Δy

$$\epsilon = \frac{\sigma^2}{\Delta y}. \quad (3.21)$$

After integration, the scattering width along the beam path through the sample is given by

$$\sigma^2 = \int_0^d \epsilon dy', \quad (3.22)$$

and the visibility of the interference fringes at the projection angle Θ can be written as a function of the linear diffusion coefficient $\epsilon(x', y')$ as

$$V^\Theta(x') = \exp \left[-\frac{2\pi^2 d^2}{p_2^2} \int_0^d \epsilon(x', y') dy' \right], \quad (3.23)$$

with p_2 the period of the interference pattern and d the distance between the phase grating G_1 and the analysing grating G_2 . In the following the images formed by the reduction of the visibility will be denoted as *dark-field image* similar to the dark-field contrast in the visible light regime.

3.1.4. Tomographic reconstruction

For the reconstruction of the object's original complex refractive index distribution, or more explicitly of $\mu(x, y)$ and $\delta(x, y)$, and of the distribution of the linear diffusion coefficient $\epsilon(x, y)$ from the three sets of projection images $T^\Theta(x')$ and $\alpha^\Theta(x')$, and $V^\Theta(x')$, respectively, a filtered backprojection algorithm as described in Section 2.2 was applied.

Transmission projections For the reconstruction of the attenuation coefficients $\mu(x, y)$ from the transmission projections $T^\Theta(x')$ in Eq. 3.15 the corresponding filtered backprojection reconstruction from the Equation 2.19 is used

$$\mu(x, y) = - \int_0^\pi \mathcal{F}^{-1} [\tau^\Theta(\omega) \cdot K(\omega)] d\Theta, \quad (3.24)$$

where $\tau^\Theta(\omega)$ represents the Fourier transform of the logarithm of the normalized transmission projection, \mathcal{F}^{-1} denotes the inverse Fourier transform operator, and $K(\omega) \equiv |\omega|$ is the frequency filter for line projection integrals.

Differential phase-contrast projections The reconstruction of $\delta(x, y)$ from the differential phase-contrast projections $\alpha^\Theta(x')$ in Eq. 3.19 is achieved as

$$\delta(x, y) = \int_0^\pi \mathcal{F}^{-1} [A^\Theta(\omega) \cdot H(\omega)] d\Theta, \quad (3.25)$$

where $A^\Theta(\omega)$ represents the Fourier transform of the projections of the measured deflection angles and $H(\omega) = i \cdot \text{sgn}(\omega)/(2\pi)$ is the imaginary filter for gradient projections, where here

$\text{sgn}(\omega)$ is the sign function. It should be noted that this kind of filtering is a Hilbert transform in real space (for more details see [31, 82]).

Dark-field projections The reconstruction of $\epsilon(x, y)$ from the dark-field projections $V^\Theta(x')$ in Eq. 3.23 is performed as:

$$\epsilon(x, y) = -\frac{p_2^2}{2\pi^2 d^2} \int_0^\pi \mathcal{F}^{-1} [\Gamma^\Theta(\omega) \cdot K(\omega)] d\Theta, \quad (3.26)$$

where $\Gamma^\Theta(\omega) = \mathcal{F}[-\log(V)]$ represents the Fourier transform of the logarithm of the normalized visibility projection in Eq. 3.14, and $K(\omega)$ is the same frequency filter as in Equation 3.24. This reconstruction assumes the dark-field signal to be independent on the sample rotation angle. This is true for homogeneous specimens, but it is also a good approximation for many other samples without a preferred orientation of the inner structures.

3.1.5. The case of incoherent illumination - The Lau effect

As already mentioned in the Section 3.1.1, a certain amount of transverse coherence is required to observe interference patterns in the self-image plane of the grating G_1 . The maximum width of the source point, up to that interference patterns can still be observed, is given as [6, Chapter 2.3.3, Eq. 2.33]

$$s = \frac{p_2 l}{2d}, \quad (3.27)$$

where l is the distance between the source and the beam-splitter grating G_1 , and d the G_1 -to- G_2 distance, i.e. the fractional Talbot distance. The transverse coherence length, that is defined as [2]

$$\xi_c = \frac{\lambda l}{s}, \quad (3.28)$$

with wavelength λ , is too short at larger source sizes to observe interference patterns in the plane of G_2 [81]. To overcome this problem an additional highly absorbing grating in the following called G_0 can be used in front of the beam-splitter grating G_1 . This additional grating divides the extended source focal point into many thin line sources and thus, creates an array of mutually incoherent virtual sources. The experimental proof of this principle for x-ray interferometry was first reported in [83].

This three-grating setup is known as *Talbot-Lau interferometer*, that allows for using the grating interferometer in combination with large sized sources. The mutually incoherent line sources add up incoherently in the plane of the analyser grating G_2 , when the period is chosen such, that the space between the interference patterns from two neighboring line sources is exactly one or an integer multiple of one period of the pattern, i.e. the so called *in registry* condition must be fulfilled [78]. This condition is fulfilled if the period p_0 of the grating G_0 is chosen to be

$$p_0 = \frac{l}{d} p_2, \quad (3.29)$$

where d corresponds to the Talbot distance G_1 - G_2 and p_2 is the period of the analyser grating G_2 .

3. Grating-based interferometry

The total size of the source is not giving the effective coherence length anymore, i.e. the visibility of the interference fringes, but the size of the individual virtual sources. An example should demonstrate the enhancement of the transverse coherence in a Talbot-Lau setup: For a photon energy of 20 keV ($\lambda \approx 6.2 \times 10^{-2}$ nm), a typical horizontal source size of a 3rd generation synchrotron undulator source of 50 μm , and a distance $l = 40$ m between the source and G_1 gives a transverse coherence length $\xi_c \approx 50$ μm . Good images with the grating-based setup can be achieved at 3rd generation synchrotron radiation sources that means that the transverse coherence of the used radiation should be in the same range. For a similar setup at a conventional x-ray tube with a source size of 0.25 mm and a distance $l = 2$ m from the source to G_1 the transverse coherence length is $\xi_c \approx 0.5$ μm . Now, we calculate the transverse coherence length in the presence of a source grating G_0 with a typical period of $p_0 = 25$ μm and a duty cycle (DC) of 0.5 directly behind the source. A DC of 0.5 means that the bar-width is exactly the half of the period². The corresponding size of the virtual sources is $p_0/2 = 12.5$ μm and $\xi_c \approx 10$ μm , that is a factor of 20 higher than the ξ_c of the x-ray tube radiation without a G_0 .

According to Pfeiffer *et al.* [83] and Weitkamp *et al.* [95] this setup decouples the property of transverse coherence from the total size of the source. However, the spatial resolution remains unaffected and is influenced by the source size, and the distances between source, sample and detector in the same way as it would be without the grating interferometer.

3.1.6. Achromaticity

The grating interferometer is highly achromatic as it even can efficiently be used with polychromatic laboratory x-ray sources. Since the Talbot distances depend on the wavelength, for polychromatic radiation the interference patterns for the Talbot distance at corresponding wavelength will be superimposed and blurred in the beam propagation direction. In the work by Engelhardt *et al.* [30] simulations of both polychromatic point sources and larger sources were presented. According to his work no limit for the acceptable bandwidth $\Delta\lambda/\lambda$ could be found, but a strong dependence on the increasing source size destroying the fringe-visibility when no G_0 is used.

The other effect of polychromaticity on the performance of the grating-based setup is the decreasing efficiency of the gratings, especially of the beam splitter grating, when the wavelength deviates from the design value (i.e. grating G_1 shifts the phase by π only at the design energy). At shorter wavelength (as the design value for the gold thickness) the efficiency of the gold gratings will significantly go down and decrease the fringe visibility. However, an acceptable bandwidth of 10% is reported by Weitkamp *et al.* [96]. The measurements of fringe visibility for changing monochromatic wavelength obtained at the beamline W2, which will be presented in the Section 3.3 confirm these results.

²Definition duty cycle: DC = bar-width/period.

3.2. Experimental implementation of the interferometer

In this section the experimental implementation of the new grating interferometer for the beamline W2 is presented, including all grating parameters, the experimental setup, and the x-ray detector, as well as the special design of the interferometer. Due to the geometrical constraints of the setup it works with a fixed geometry by changing the Talbot orders by increasing or decreasing the x-ray energy but not the distances. In addition, the detector used for the measurements is introduced. A detailed description of the image acquisition process is given in the Appendix B, explaining the complete image acquisition chain, including the correct alignment of the gratings before the measurement. The grating-production process is explained in Appendix C.

3.2.1. Interferometer geometries

As described in the previous Section 3.1.5 the x-ray source size should not exceed a certain size s , else the visibility of the interference fringes behind the beam-splitter grating G_1 (see Eq. 3.27) diminishes. The horizontal source size in the wiggler of the beamline W2 is given as $\sigma_x = 1.7$ mm (see Table 2.1) and using Eq. 3.28 we can calculate the transverse coherence length ξ_c^{W2} for a photon energy of 20 keV to

$$\xi_c^{W2} = \frac{\lambda l}{s} = \frac{6.2 \times 10^{-11} \text{m} \times 48 \text{m}}{1.7 \times 10^{-3} \text{m}} = 1.75 \mu\text{m} . \quad (3.30)$$

The result shows that the transverse coherence length of the wiggler beamline W2 is in the range of a conventional x-ray tube (calculated in the previous section to be $\approx 0.25 \mu\text{m}$ for 20 keV). Hence, the transverse coherence length is not sufficiently long for a two grating setup as it is used at 3rd generation synchrotron sources. To overcome this problem, the Lau effect as described in Section 3.1.5 can be used by placing an absorbing source grating G_0 upstream of the beam-splitting grating G_1 .

Figure 3.3(a) shows a schematic of the x-ray grating interferometer designed for the low-coherence beamline W2 consisting of three gratings: an absorbing source grating G_0 (Au), a beam-splitter grating G_1 (Si, phase shift of π), and an absorbing analyser grating G_2 (Au). The principle of such an interferometer is explained in the previous section and schematically illustrated in Figure 3.3(b).

The periods and the depths of the gratings for the setup at the beamline W2 are listed in Table 3.1. To switch between the different fractional Talbot orders the photon energy has to be changed while the inter-grating distances are kept fixed. So, we should derive the *Talbot wave lengths* instead of the distances for our grating interferometer. From the Equations 3.2 and 3.6 we can calculate the Talbot wavelengths as

$$\lambda_n = nM \frac{p_{1,e}^2}{2d_n} , \quad (3.31)$$

where n is the odd fractional Talbot order ($n = 1, 3, 5, 7, 9, \dots$), corresponding to x-ray wavelengths of 0.8, 2.4, 4.0, 5.6, 7.2, ... $\times 10^{-11}$ m or photon energies of 152, 51.4, 30.8, 22.0, 17.1, ... keV, $p_{1,e}$ is the effective period of the phase grating G_1 , and d_n is the fractional Talbot

3. Grating-based interferometry

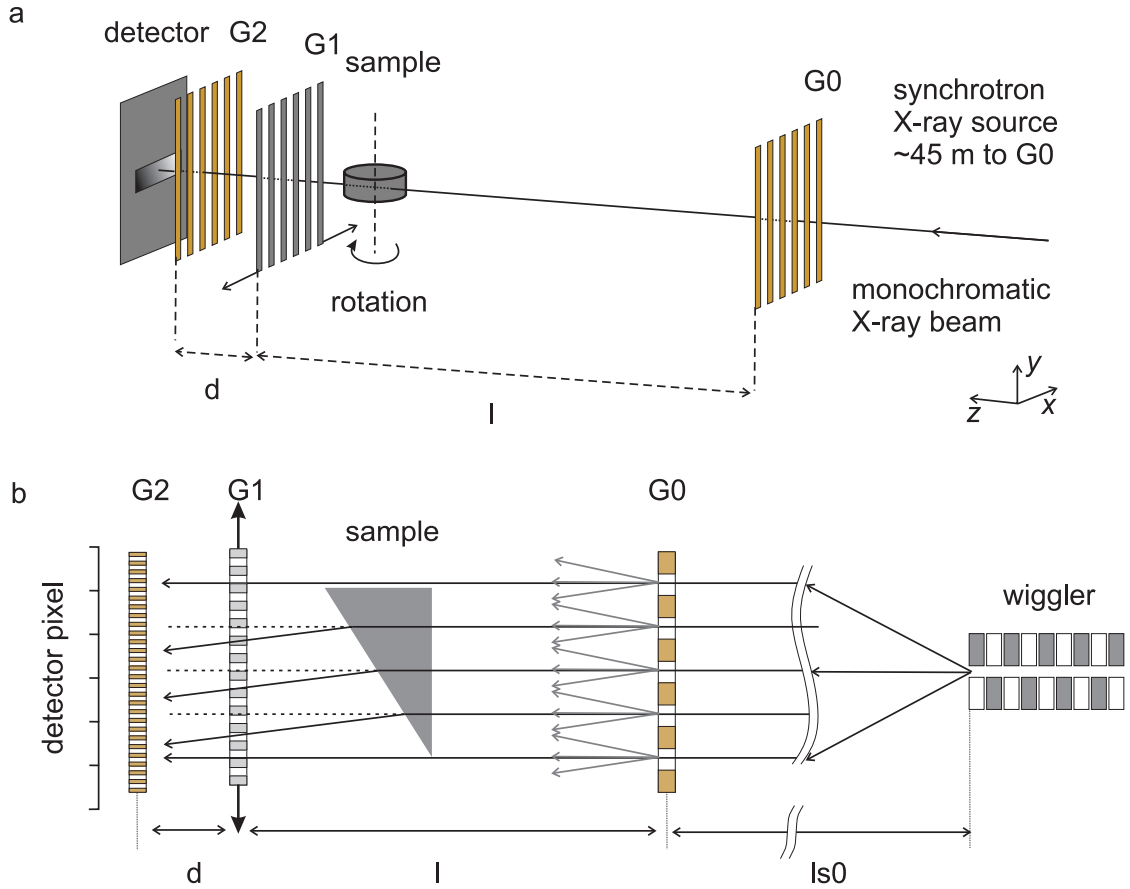


Figure 3.3.: (a) A schematic of the grating interferometer setup at the beamline W2 consisting of three gratings - the source grating G_0 , the phase grating G_1 and the analyser grating G_2 with the intergrating distances $l = 3.00$ m and $d = 0.32$ m. (b) The schematic illustrates how the interferometer works at a non-coherent x-ray source. The source gold grating G_0 produces many small partially coherent line sources, the partially coherent beams penetrate the sample, are refracted and cause a shift in the interference pattern produced by the phase grating G_1 . This interference pattern is analysed by the analyser gold grating G_2 and projected onto the detector pixels.

distance scaled by the magnification factor according to Eq. 3.6. These photon energies are theoretically calculated and represent the expected energies with high contrast that can be used for imaging with the interferometer. Experimentally usable photon energies are strongly influenced by the beam-splitter grating, which is designed for only one energy and decrease the visibility of the interference pattern for all other energies. The design energy of a grating depends on its height that deviates due to the production process from one grating to the next. The Table 3.1 lists the heights of the four different phase gratings and the energies, which arise from these heights.

Now we should calculate the transverse coherence length for the beamline W2 with the source grating G_0 and a duty cycle (DC) of 0.7. We can use the Equation 3.30 and replace

³The height was determined to be $54 \mu\text{m}$ during the production, but the experimental results show that the grating must have similar height as the $G_{1\#4}$. The height was not tried to be measured, as the $G_{1\#2}$ showed the highest visibility and such a measurement would put it at risk.

3.2. Experimental implementation of the interferometer

Table 3.1.: Grating properties

The list of the grating geometries designed for the beamline W2. The two gold gratings G_0 and G_2 are usable in the energy range below the given energy (absorption of 90 % at the given energy) and the four phase gratings G_1 are optimized for the design energies. Above the design energy of the gold gratings the interference pattern visibility decreases, as the grating absorption becomes insufficient.

The use of the phase grating G_1 at its design energy increases the visibility, since then the phase shift induced by the grating is almost π . The source grating G_0 consists of two areas: one with a duty cycle 0.7 to increase visibility and the other with 0.5 to have more photon flux.

Grating	design energy	period	height	duty cycle
	E_{ph} [keV]	p [μm]	h [μm]	DC \pm std
phase grating G_1 #1	27.3	4.33	35	0.42 ± 0.02
phase grating G_1 #2	32.7	4.33	42 ³	0.54 ± 0.04
phase grating G_1 #3	25.7	4.33	33	0.40 ± 0.02
phase grating G_1 #4	32.7	4.33	42	0.49 ± 0.06
source grating G_0	30	22.29	45-50	0.7/0.5
analyser grating G_2	25	2.4	30.8	0.5

the wiggler source size s by the period p_0 scaled with the DC of the source grating G_0 and the distance l by the distance ξ_{01} between the source and the beam-splitter grating:

$$\xi_c^{G_0} = \frac{\lambda_{01}}{(1 - 0.7)p_0} = \frac{6.2 \times 10^{-11}\text{m} \times 3\text{m}}{22.3 \times 10^{-6}\text{m} \cdot 0.3} = 27.8\mu\text{m} , \quad (3.32)$$

that is one order of magnitude larger than ξ_c^{W2} . Using the G_0 instead of a narrow slit has the advantage that the loss of intensity is smaller and due to the short distance from the slit system at the beamline W2 of about 10 m, the field of view would be very limited when working with a single slit. A larger distance l_{01} would increase the transverse coherence but the chosen distances are the maximum possible at the beamline W2.

3.2.2. Mechanical components

The grating-based imaging system consists of an x-ray detector, an air beared high precision rotation axis and the motorized grating holder. The Figure 3.5(a) and (b) show the motorized grating holder (6 motors for alignment and 1 piezo for stepping the beam-splitter grating G_1), (b) the source grating placed on the diffractometer providing many degrees of freedom for adjusting the G_0 in respect to the other two gratings. The Figure 3.4 shows a schematic of the motorised parts of the interferometer showing the degrees of freedom, which are needed to align the gratings. Not shown are the adjustment possibilities of the source grating G_0 , which is mounted inside a goniometer with motorised adjustments in all possible directions.

The absorbing gold grating G_0 and the phase grating G_1 were fabricated by C. Grünzweig and C. David at the Paul Scherrer Institut (Villigen/PSI) in Switzerland. Both these gratings were produced on 4 inch silicon wafers in a fabrication process involving photolithography, deep etching into silicon and for the absorption grating G_0 electroplating of gold. The fabrication process of these two gratings is described in detail by David *et al.* [25] and is presented in the Appendix C. The analyser gold grating G_2 is produced by E. Reznikova and J. Mohr

3. Grating-based interferometry

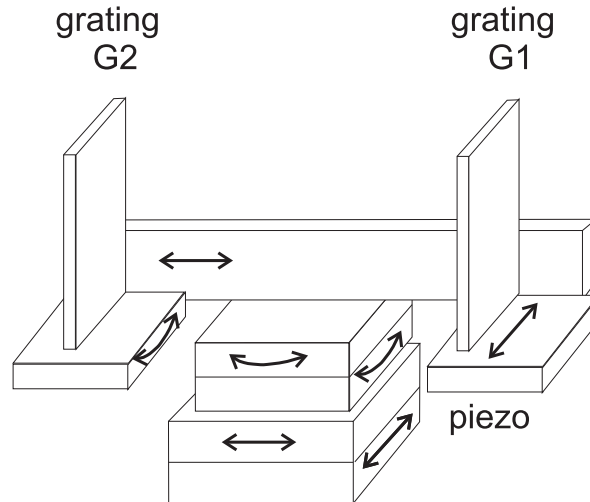


Figure 3.4.: A scheme of the adjustment motors showing 6 motors for the grating alignment of G_1 and G_2 and a piezo to step the phase grating G_1 (the grating on the right).

from Karlsruhe Institute of Technology (KIT), Karlsruhe, Germany. It is more critical, as the same height is required as for the source grating G_0 but the period is one order of magnitude smaller. The fabrication process of this grating is also explained in the Appendix C.

3.3. Influence of an extended, distant wiggler source

The three-grating interferometer method was transferred for the first time from a tube source to a low-coherence wiggler beamline source at the 2nd generation synchrotron storage ring. The influence of an extended and distant source point in combination with a beam-splitter grating G_0 to the Talbot effect has not been studied before.

The calculation from the previous section showed that the coherence conditions at the beamline W2 are comparable with those of a conventional x-ray tube. Hence, a source grating is used, which produces a virtual source with a higher transverse coherence length in the plane of G_0 . In this Section it will be shown that a source grating decouples the property of transverse coherence from the total size of the wiggler source as already stated by F. Pfeiffer *et al.* [83] and T. Weitkamp *et al.* [95]. Thus, all grating geometries and the Talbot wavelengths can be calculated with the assumption of a source in the G_0 plane. Simulated as well as experimental results will be shown proving this assumption and demonstrating that after the installation of the source grating G_0 its plane can be considered as a new source for the self-imaging effect.

3.3.1. Wavefield propagation formulas

Wave field propagation calculations are used to reconstruct the amplitude and the phase changes of a wave front propagating through free space and through several objects from the source to the detector plane. The free-space propagation can be calculated using the *Huygens-Fresnel* principle, i.e. by the superposition of the spherical waves starting from each point in the source plane. According to this principle, the wave field of a monochromatic

3.3. Influence of an extended, distant wiggler source



Figure 3.5.: The grating interferometer setup at the beamline W2. (a) The part downstream of the sample, which is mounted hanging down from the rotation stage into a water bath, consists of the phase grating G_1 , the analysing absorbing grating G_2 , and the detector including the lens system and the blackened luminescence screen. (b) The source gold grating G_0 is mounted 3.0 m upstream of the grating G_1 .

radiation source propagating from the plane z_1 to z_2 starting with the amplitude $E_1(x, y)$ results in a wave field amplitude $E_2(x, y)$ as [35]

$$E_2(x, y) = \frac{1}{i\lambda} \iint E_1(x', y') \frac{e^{ikr}}{r} \cos \alpha \, dx' dy' , \quad (3.33)$$

3. Grating-based interferometry

This equation is known as the *Fresnel-Kirchhoff* equation, with r representing the distance between the points in z_1 and z_2 and is given by

$$r = \sqrt{(x - x')^2 + (y - y')^2 + (z_1 - z_2)^2}. \quad (3.34)$$

The Fresnel-Kirchhoff Equation 3.33 can be simplified by replacing r in the denominator of Equation 3.33 by the beam direction z and taking it out of the integral. In addition, using the paraxial approximation⁴ the r in the exponent ikr can be approximated by the first terms of a binomial expansion as [35]

$$r \approx z + \frac{(x - x')^2 + (y - y')^2}{2z}. \quad (3.35)$$

With this approximation the Fresnel-Kirchhoff equation can be written as (the factor $\cos \alpha \approx 1$ for small angles and can be neglected)

$$E_2(x, y) = \frac{e^{ikz}}{i\lambda z} \int \int E_1(x', y') \exp\left(ik \frac{(x - x')^2 + (y - y')^2}{2z}\right) dx' dy'. \quad (3.36)$$

Now, with the definition of a *propagator kernel*

$$h_z(x, y) = \frac{e^{ikz}}{i\lambda z} e^{\frac{ik}{2z}(x^2 + y^2)}, \quad (3.37)$$

the Equation 3.36 can be written as a convolution of the incident wave front $E_1(x, y)$ with the kernel:

$$E_2(x, y) = \int \int E_1(x', y') h_z(x - x', y - y') dx' dy'. \quad (3.38)$$

The convolution in real space is a simple multiplication in Fourier space

$$E_2(x, y) = \mathcal{F}^{-1}(\mathcal{F}(E_1) \times \mathcal{F}(h_z)). \quad (3.39)$$

The use of the Fresnel-Kirchhoff equation in Fourier space and of the paraxial approximation allows fast simulations of an x-ray imaging setup. This sort of simulations does not consider any partial coherence in case of a finite source size or energy bandwidth. In this case, the resulting intensities in the observation plane have to be calculated using the Equation (3.38) for monochromatic point sources and integrated over the transverse cross section of the source and the frequency range (see [35, 94] for more details).

3.3.2. Simulations of visibility

In this work the simple approach was chosen, without taking the partial coherence of the wiggler source into account. All calculations were made assuming a monochromatic incoming plane wave at the sample position. This assumption is valid, as the distance between the source focal point in the wiggler and the sample plane is large (48 m). The extension to a spherical setup can also be easily made by considering the magnification factor from Equation 3.5. The simulation then consists of the following steps:

⁴The paraxial approximation assumes only small refraction angles.

3.3. Influence of an extended, distant wiggler source

1. The complex plane wave front is multiplied with the phase shift introduced by the beam-splitter grating G_1 .
2. This plane wave front is propagated to the observation plane with the analyser gold grating G_2 . The propagation is performed using Equation 3.39 in Fourier space and the result is transformed back to the space domain.
3. The resulting complex wave front is multiplied in Fourier space by the Fourier representation of the G_0 and the G_2 described by the corresponding transmission of gold at the desired energy. This multiplication corresponds to a convolution with the shape of G_0 and G_2 in space domain. To simulate grating imperfections the shape of the gratings have been smoothed with a smoothing factor of 20 %.
4. The visibility of the interference fringes is calculated using Equation 3.11 and the Fourier coefficients a_0 and a_1 .

In other words, we describe our setup with a radiation source situated in the G_0 plane and producing a monochromatic, plane wave front that is shifted in phase by G_1 exactly by a factor of π^5 and producing a Talbot self image in the plane of G_2 . The calculations of the visibility were performed for different x-ray energies for the setup at the beamline W2 using Matlab. The simulated results were compared to the measured visibility values for the corresponding energies (see next section).

3.3.3. Measurement of visibility

The visibility of the interference pattern in the plane of G_2 was measured for different x-ray energies. It was calculated as described in the Section 3.1 according to the classic definition in Equations 3.14 and using the first order amplitude a_1 relative to the average value a_0 according to Equation 3.11 for each single detector pixel.

The setup at the beamline W2 consists of the source grating G_0 with a duty cycle of 0.7, an analyser grating G_2 , an x-ray detector and a phase grating G_1 , that was changed to test all available phase gratings (G_1 #1, #2, #3, and #4 all listed in the Table 3.1). For the phase gratings #1 and #2 the x-ray energy was varied from 16 to 60 keV in 0.5 keV steps and for the other two phase gratings the steps were chosen to 1 keV for a faster measurement. At each energy a phase scan with 16 phase steps over 2 periods of the interference pattern was performed, taking images at each step. The exposure times varied during the energy scan to avoid overexposure of the detector at higher x-ray energies with higher photon flux. During further data analysis the mean value of visibility averaged over 200×100 pixels in the middle part of the projections was calculated and plotted together with the simulated values against the corresponding x-ray energy as shown in Figures 3.6 (a)-(d).

The plots in Figure 3.6 show the same shape for the measured and the simulated visibility. The phase gratings G_1 #1 and #3 show three significant visibility peaks: 7th fractional Talbot order at 22 keV, 6th fractional Talbot order at 25 keV, and 5th fractional Talbot order at 30 keV. The other two phase gratings #2 and #4 do not show the 6th fractional Talbot order

⁵The phase shift is only exactly π at the design energy of the grating G_1

3. Grating-based interferometry

peak at 25 keV, which is produced by a duty cycle deviating from the optimum value of 0.5 as could be seen in simulations. The height of the phase grating $G_1\#1$ was determined during the production to be $54\ \mu\text{m}$. If this was correct, the measured visibility peak at 22 keV (see Figure 3.6 (a)) would disappear, since it would shift the phase of the incoming x-ray beam by 2π at 22 keV. The measurement showed that the height was not correctly determined. But, the measured curve showed the same shape as the one of the grating $G_1\#4$, thus, the same height as the grating $G_1\#4$ was used for the visibility simulations. The height was not measured again, as any measurement procedure would put the grating at risk that is the best of the phase gratings showing the best performance. The absolute values at the peak energies in the simulations deviate slightly from the measured values, since the calculations were made for ideal gratings and a plane wave field setup, which were smoothed by a smoothing factor of 20 %. In the plots in Figure 3.6 (b) and (d) the calculated visibility between the two maxima is lower than the measured one. This deviation can be explained by the high dependence of the calculations on the duty cycle of the phase grating G_1 as can be seen from the plots in (a) and (c) of the same figure. The DC deviation of all phase gratings is in the range of several percent but it leads to an additional visibility peak for the gratings $G_1\#1$ and $\#3$.

The Talbot energies were correctly calculated with the assumption of a source in the G_0 plane. If the source focal point in the wiggler affected the Talbot orders, they would be at significantly different x-ray energies: the 7th fractional Talbot order at 24.2 keV, the 6th fractional Talbot order at 28.4 keV, and the 5th fractional Talbot order at 33.9 keV. As the measurement matched the simulated visibility peak positions very well, it clearly demonstrates that the approximations made for the calculations before were correct.

The question, if the amount of partial coherence resulting from the long travel distance of the beam from the wiggler to the sample plane (about 48 m) does affect the visibility, was experimentally analysed. For this measurement a phase scan was performed at 7th fractional Talbot order and 22 keV with rotating sheets of paper directly in front of the source grating G_0 . The rotating paper consisting of 6 sheets of standard printer paper ($80\ \text{g}/\text{cm}^2$) acted as a coherence diffuser. The phase grating $G_1\#2$ was used for this measurement. The measured visibility was averaged over 500×500 pixels in the middle region of the projection and compared to the averaged visibility measured without paper in the beam. No significant influence of the partial coherence of the x-ray wave field in front of G_0 could be found. The averaged visibility with coherence diffuser was found to be $28.8\ \% \pm 1.5\ \%$ and the one without diffuser $28.2\ \% \pm 1.5\ \%$.

The experimental results as well as the simulations showed that the influence of the distant wiggler source to the Talbot self-imaging effect can be neglected. Only in the case of spatial resolution the wiggler source does influence the performance of the grating setup. This influence will be analysed in detail in the following section.

3.4. Spatial resolution

For the imaging applications in absorption mode at the beamline W2 the spatial resolution of the imaging system is determined by means of a horizontal edge of a highly absorbing

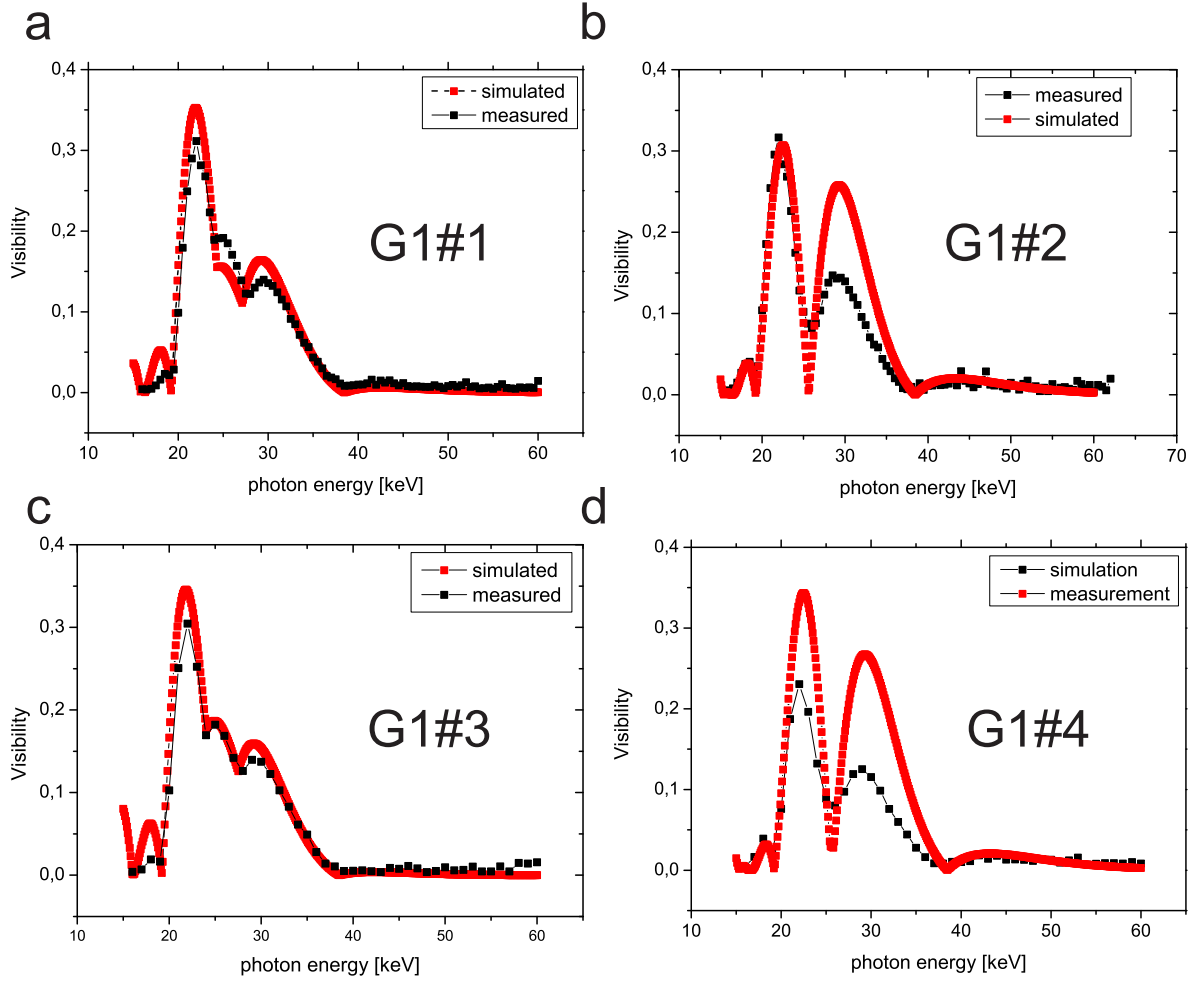


Figure 3.6.: Measured and calculated visibility for different beam-splitter gratings G_1 from the Table 3.1 plotted against photon energy. Plots (a) and (c) show additional visibility maxima due to the DC that is deviating stronger from 0.5. The grating $G_1\#2$ and 4 from the plots in (b) and (d) do not show the additional peak as their DC matches better the value of 0.5. Please mind the different scaling of (a),(c) and (b),(d).

material (Densimet) prior to the measurement. This approach is based on the works by N. J. Schneiders [91], F. Beckmann [7] and F. Busch [19], and T. Donath [28]. It obtains objective values for the spatial resolution achievable with an imaging system compared to other methods that determine the spatial resolution by imaging very fine structures like *Siemens stars*. The further development of the method using an edge was made by T. Donath, who described it in detail in his PhD thesis [28]. The procedure also used in this work determines the spatial resolution using a highly absorbing edge and is briefly presented below. As the spatial resolution strongly depends on the source size, the vertical and the horizontal spatial resolution at the beamline W2 is not the same, since the source size in horizontal is larger than in the vertical direction (see Chapter 2). In case of conventional absorption-mode applications, where the detector is as close as possible to the sample, the difference is found to be negligible (see [28, Appendix D.7]). In our case of grating-based phase-contrast imaging this difference cannot be neglected, as the sample-to-detector distance is 0.32 m. In addition,

3. Grating-based interferometry

the grating interferometer provides a signal only perpendicular to the grating structures that is in our case the horizontal direction. Hence, the difference between the vertical and the horizontal spatial resolution is of great interest for our method.

Here, an approach is shown to determine the spatial resolution from an edge produced by a silicon 90 degrees edge in both interferometer signals: the absorption and the differential-phase contrast. When rotating the edge by 45 degrees it produces a wedge, which increases linearly the phase shift with the material thickness. The measured signal shows an edge function starting at zero, as the first derivative of the phase-shift is measured. From this edge function a modulation transfer function can be calculated, that describes the spatial resolution of our system in horizontal direction. By rotating the silicon edge back it produces an edge function in the absorption contrast of the interferometer that can be used to calculate the MTF for the absorption-contrast signal.

3.4.1. MTF and spatial resolution

The response of an imaging system, that is assumed to be linear and shift invariant, can be calculated by a convolution of the input signal with the system's *point spread function* (PSF), which fully characterizes the spatial response of the system. Determining the *modulation transfer function* (MTF) related to the PSF from measured data allows for quantifying the spatial resolution in the obtained images.

The approach to determine the spatial resolution in projections used for the microtomography applications in absorption-contrast mode at the beamline W2 prior to each application will be briefly presented here. A modification of this approach was used in this work. The approach is based on the measurement of the edge spread function (ESF), produced by a strongly absorbing material causing a sharp edge in the detected signal. One cannot measure the PSF directly, as the PSF describes the system's response to a delta-peak shaped signal that could only be produced by a point-like source.

The measured image $i(x, y)$ in microtomography is given by a two dimensional convolution of the object function $o(x, y)$ and the point spread function $s(x, y)$ (PSF) as

$$i(x, y) = s(x, y) ** o(x, y) = \int_{-\infty}^{\infty} \int_{-\infty}^{\infty} s(x - x', y - y') o(x', y') dx' dy' , \quad (3.40)$$

where ** represents a two-dimensional convolution. As we measure intensities, all functions in real space are real functions. The point spread function is usually defined to be normalized to unity as

$$\int_{-\infty}^{\infty} \int_{-\infty}^{\infty} s(x, y) dx dy = 1 . \quad (3.41)$$

This normalization has the consequence that the integral intensity in the images is not changed by the convolution.

A convolution in real space is a simple multiplication in the Fourier space. Applying the

Fourier transform to Equation 3.40 leads to

$$\mathcal{F}(i) = I(u, v) = S(u, v)O(u, v) , \quad (3.42)$$

with a complex function $S(u, v)$ representing the Fourier transform of the point spread function, also called optical transfer function (OTF). The modulation transfer function (MTF) can be derived from the OTF by

$$M(u, v) = \frac{|S(u, v)|}{S(0, 0)} = |S(u, v)| , \quad (3.43)$$

which holds only for the normalized PSF giving $S(0, 0) = 1$.

A line spread function (LSF) is the response to a line-shaped input signal, and an edge spread function (ESF) is the corresponding response for an edge-shaped signal. It can be shown that the LSF is the derivative of the ESF, and that the LSF is the projection of the PSF of the system⁶.

In terms of simplicity we omit the second dimension y without losing generality. In the case of a real PSF, that we assume here, the one-dimensional ESF(x) determines the line spread function LSF(x) by

$$\frac{d}{dx}\text{ESF}(x) = \text{LSF}(x) . \quad (3.44)$$

From the LSF(x) the OTF $S(u)$ from Equation 3.42 can be calculated by an one-dimensional Fourier transform of the LSF(x)

$$S(u) = \mathcal{F} [\text{LSF}(x)] . \quad (3.45)$$

This Equation 3.43 will be used to determine the MTF from a single edge profile. The steps to measure the MTF are described by T. Donath in [28, Chapter 2.4, Appendix D.1] as follows

1. Measurement of an edge spread function ESF(x),
2. calculating the line spread function LSF(x) by derivation of ESF(x),
3. calculation of the MTF(u) by a one-dimensional Fourier transform of LSF(x).

As a resolution parameter the spatial frequency f_{10} is used, at which the MTF of the system falls below 10 %. The characteristic length to calculate the resolution the value a_{10} is given as

$$a_{10} = \frac{1}{2f_{10}} . \quad (3.46)$$

The quantity a_{10} will be given as the spatial resolution of the imaging system.

3.4.2. MTF calculation using a silicon cuboid

The standard procedure at the beamline W2 is to determine the spatial resolution parameter a_{10} as defined in Equation 3.46 for every different setup by calculating the MTF of

⁶The derivation can be found e.g. in the work by T. Donath [28]

3. Grating-based interferometry

a horizontal, highly absorbing edge (material: Densimet) placed in the sample plane. For absorption-contrast, where the detector is placed as close as possible downstream the sample, the spatial resolution in vertical and horizontal direction is almost the same, although the source focal point dimensions in vertical and horizontal direction differ very strongly.

In our case, the distance between the sample plane and the detector is at least 40 cm, as the grating holder for the phase grating G_1 and the analyser grating G_2 has to fit between the sample and the detector. In addition, the gratings itself introduce more blur to the images. Therefore, we expect that the spatial resolution in horizontal direction will significantly deviate from that in vertical direction. First, the spatial resolution was determined using the standard procedure with a Densimet edge in horizontal and vertical direction. This was done with the grating holder inside but without the gratings in the beam. Then the spatial resolution was measured with the grating-based setup using a silicon wedge in two different configurations (see Figure 3.8) for the absorption and the phase contrast respectively. Both measurements with the Densimet edge and the silicon cuboid were carried out at 30 keV that corresponds to the 5th fractional Talbot order of the interferometer and with an effective pixel size of 3.2 μm . The calculation of the MTF from the projections taken with the grating interferometer setup was performed following the same procedure as described above. The silicon edge produced a strong signal in both, absorption and phase-contrast projections that is important to hold the normalisation in Equation 3.41.

In Figure 3.7 the MTFs are plotted measured in horizontal and vertical direction as they were determined using the standard focussing procedure at the beamline W2. For this measurement the same distance between the object and the detector is chosen like in the grating-based setup. The spatial resolution is given by the value a_{10} , where the MTF signal decreases to 10 %. According to the expectations the spatial resolutions in horizontal $a_{10}^{horizontal} = 33.8 \mu\text{m}$ and vertical $a_{10}^{vertical} = 5.8 \mu\text{m}$ direction deviate strongly from each other due to the large difference in the source size dimensions in these two directions. This deviation in the spatial resolution in vertical and horizontal direction is strongly dependent on the source size and shape. Radiation sources with much higher brilliance like the third generation synchrotron radiation sources provide radiation with a much lower divergence. Thus, with the same geometry sources with high brilliance will provide a much better spatial resolution. For the conventional x-ray tube sources the spatial resolution depends in the same way on the source point parameters, but in the most cases it is limited by the detector resolution. The spatial resolution using the conventional tube source at PSI is estimated in the Section 4.4 to be limited by the detector pixel size of 172 μm . For more details see the work by M. Bech [6] who compared different x-ray radiation sources and their pros and cons in terms of grating-based phase contrast.

The monochromator with a vertical beam shift also influences the divergence of the beam. It reduces the divergence in the vertical direction, but does not influence the divergence in the horizontal direction, which is given by the wiggler source. These facts become important when measuring with the grating interferometer setup. To compare the results of the standard procedure to calculate the MTF of an edge we also would like to determine the MTF out of the signals measured with the grating-based setup.

To determine the MTF of the differential-phase signal the highly absorbing Densimet edge could not be used, as it did not produce a proper edge function but an unwanted phase-

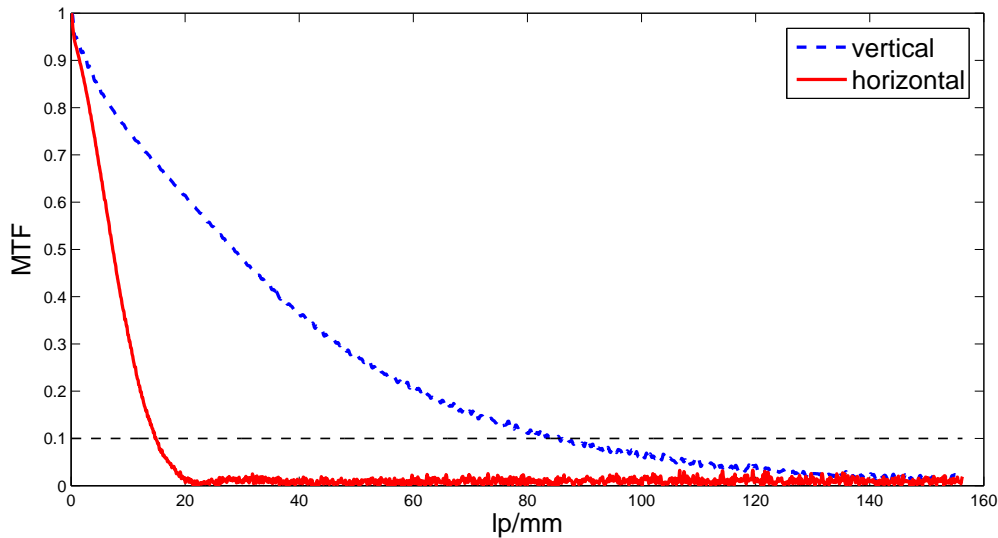


Figure 3.7.: The MTFs determined using the standard focussing procedure at the beamline W2 with a Densimet edge in horizontal (red solid line) and vertical (blue dashed line) direction measured at 30 keV with an effective pixel size of $3.2 \mu\text{m}$. The horizontal black dashed line marks the 10 % value of the MTF that is significantly higher for the vertical direction 85.2 lp/mm than that in horizontal direction 14.5 lp/mm that corresponds to the spatial resolutions of $a_{10}^{\text{vertical}} = 5.8 \mu\text{m}$ and $a_{10}^{\text{horizontal}} = 33.8 \mu\text{m}$.

wrapping at the edge due to a very high phase shift compared to that of the background (in this case air). The idea is to use a wedge with a very sharp edge. A wedge is a structure with linearly increasing thickness, which will produce an edge function in the differential-phase signal that corresponds the first derivative of the phase shift. Silicon was chosen as the material that provides very sharp edges when cut along defined directions. In our case a 90 degree angle was cut into a piece of silicon with an edge length of 1 cm. Figure 3.8 shows the measuring procedure for both signals, the absorption and the differential-phase signal. For the absorption contrast measurement [Fig. 3.8(a)] the silicon cuboid was placed with a frontal area to the detector to produce an edge function in the transmission signal. The same silicon cuboid as used for the absorption projection was rotated by 45 degrees to produce an edge function in the differential-phase signal [Fig. 3.8(b)]. Figures 3.8 (c) and (d) show the respective transmission and differential-phase projection of the silicon edge measured with the grating interferometer. In the red marked regions the signal was averaged over 200 rows resulting in the profiles shown in Figure 3.8 (e) and (f), which were used for the MTF calculations. During the averaging process the inclination of the edge was taken into account.

Figure 3.9 shows a plot of the MTF determined from the signals in absorption (black solid line) and in differential-phase contrast (red dashed line) using the silicon edge. The black dashed line marks the 10 % MTF signal used to quantify the spatial resolution. The MTF of both signals, the transmission signal and the differential-phase signal falls to 10 % of its maximum value at 13.5 lp/mm, which corresponds to a spatial resolution of $a_{10} = 37 \mu\text{m}$.

The values determined using the silicon edge are slightly higher than those measured with

3. Grating-based interferometry

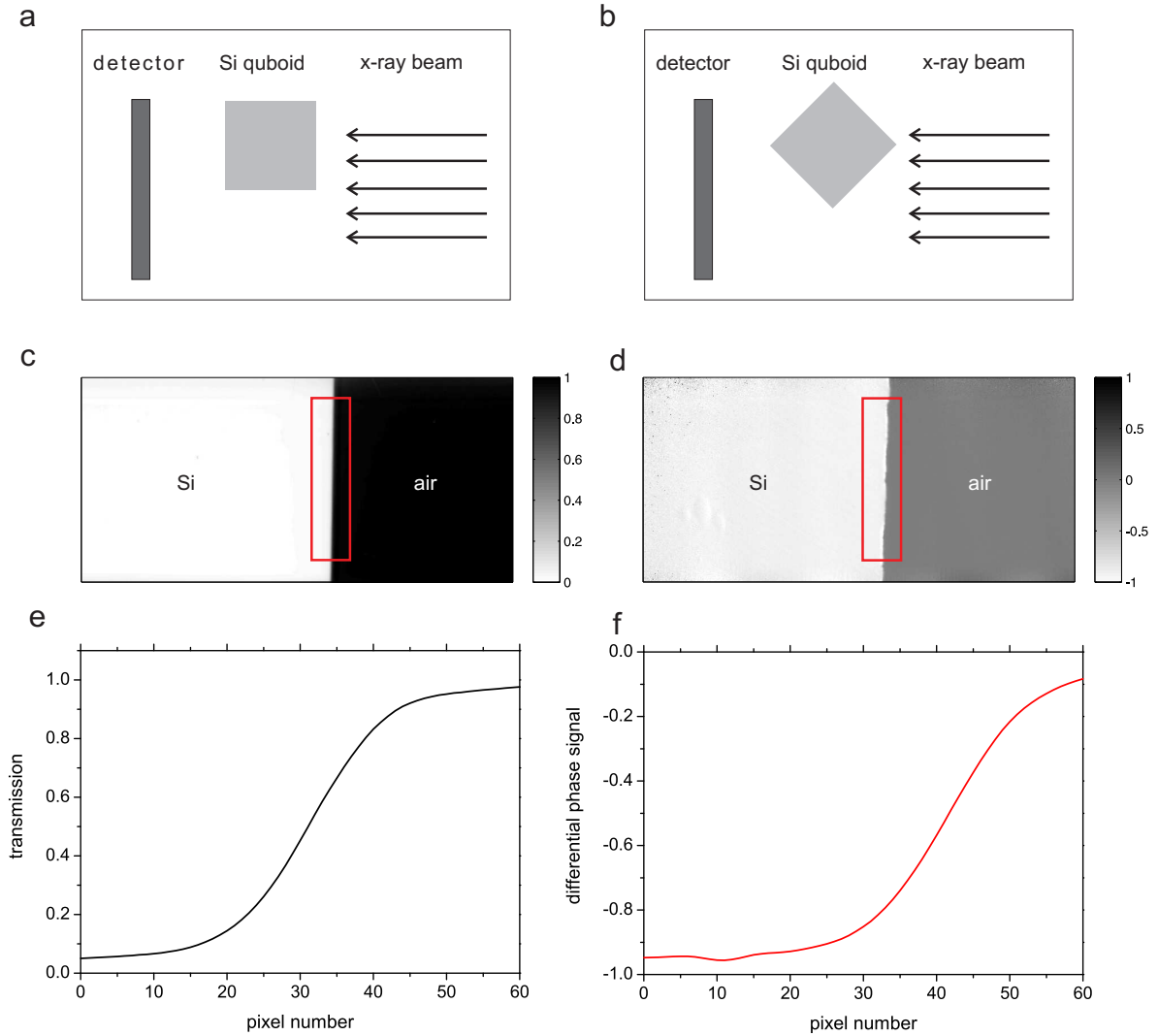


Figure 3.8.: Procedure for measuring the MTF for absorption and differential-phase contrast. (a) The silicon cuboid is placed with a frontal area to the detector to produce an edge function in the transmission signal. (b) The same silicon cuboid used in (a) is rotated by 45 degrees to produce an edge function in the differential-phase signal. (c) A transmission, and (d) a differential-phase projection of the silicon edge measured with the grating interferometer. The red marked regions were used for MTF calculations. (e) and (f) show the profiles used for MTF calculations obtained by averaging the red marked regions in (c) and (d) over 200 rows.

the standard MTF procedure with a Densimet edge giving a slightly worse spatial resolution in horizontal direction. This result corresponds to the expectations as the gratings cannot enhance the spatial resolution but introduce more blur. The spatial resolution in this dimension is limited by the horizontal source focal point that is much larger than the one in vertical direction. The spatial resolution in both signals, absorption and differential-phase contrast was found to be the same. As the spatial resolution strongly depends on the setup, the MTF calculation with the silicon edge should be repeated after any change of the settings like sample-to-detector distance, photon energy, fractional Talbot, or magnification.

This result means that the spatial resolution is limited by the source size of the wiggler source producing a divergent beam. Using the third generation synchrotron sources the limit for the spatial resolution will be the grating period of the beam-splitter grating, as the beam divergence at these sources is very small.

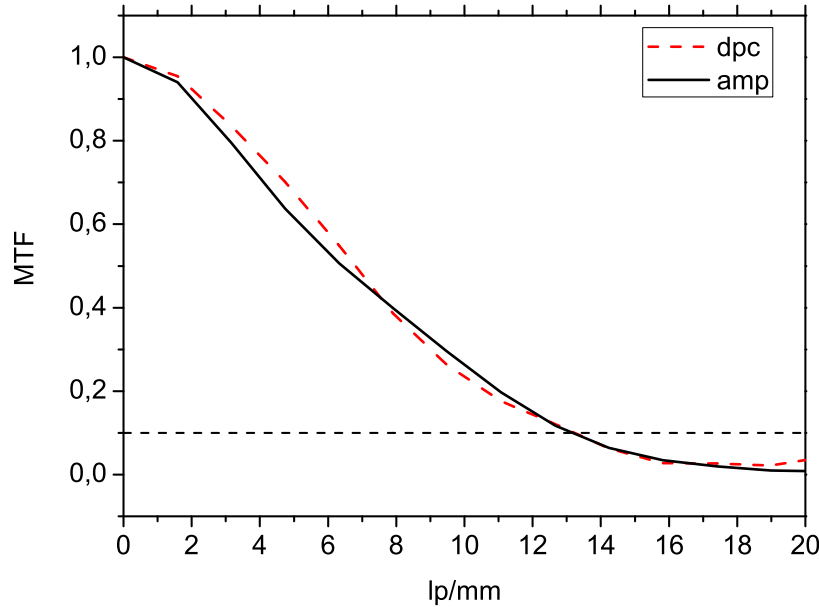


Figure 3.9.: The MTFs of an edge from the transmission and the differential-phase signal both carried out at 30 keV, at the 5th fractional Talbot order of the interferometer, and with an effective pixel size of 3.2 μm . The MTF is plotted against spatial frequency in lp/mm. The black dashed line marks the 10 % of the maximum. The MTF from the differential-phase signal (red dashed line) falls to 10 % at 13.5 lp/mm that corresponds to a spatial resolution of $a_{10} = 37 \mu\text{m}$. The MTF of the transmission signal (black solid line) falls to 10 % at the same value.

The silicon wedge allows to determine the MTF in both signals, absorption and phase-contrast, and gives reliable values for the spatial resolution achievable in the projections. Thus, in terms of spatial resolution the tomographic projections obtained with the grating-based setup become comparable to those obtained with the conventional absorption contrast setup at the beamline W2, although it is worse than the resolution with the standard microtomography setup in absorption mode that achieve spatial resolutions down to 2 or 3 μm (due to the small distances between the specimens and the detector). This simple MTF measurement procedure can be performed at any other grating-based setup to get consistent numbers for the spatial resolution achieved in the tomographic scans.

4. Quantitative phase-contrast computed tomography of a liquid phantom

4.1. Motivation

In this chapter the results of a phase-contrast computed tomography study (PC-CT) on self-made liquid phantoms are presented. The liquid phantoms consisted of several small plastic tubes filled with chemically well-defined liquids, which were measured in PC-CT. The measured attenuation coefficients and the refractive index decrements of the liquids were compared to the theoretical values. Measurements were made using the x-ray grating interferometer with a synchrotron radiation source at the beamline W2, and with a polychromatic x-ray tube at the Paul Scherrer Institut.

The primary aim of the measurements was to verify the simultaneous, quantitative determination of the attenuation coefficient (μ) and the refractive index decrement (δ) distribution inside an object in three dimensions for both source types. In addition, as the measured values were compared to the theoretically calculated values, the measurement was used to demonstrate the accuracy of the newly designed and constructed grating interferometer setup at the synchrotron wiggler source. The sensitivity of the synchrotron setup is compared for two different photon energies and Talbot orders by using the contrast-to-noise ratios (CNR) of the different investigated fluids. The results from the polychromatic x-ray tube were produced during a three-month research stay at the Laboratory for Micro- and Nanotechnology at Paul Scherrer Institut. With this study we would like to show the quantitateness of the grating-based PC-CT, even when using a polychromatic x-ray source.

Here, only two signals provided by the x-ray grating interferometer will be analysed: the conventional attenuation-contrast and the phase-contrast signals. The third signal - the dark-field signal - is not taken into account, as this study deals with imaging of fluid phantoms with no inner structures that could contribute to small-angle scattering.

The results obtained at a conventional x-ray tube were published in Herzen *et al.* 'Quantitative phase-contrast tomography of a liquid phantom using a conventional x-ray tube source', Optics Express Vol. 17, No. 12, 2009 [49], those from the synchrotron radiation source are published here for the first time.

4.2. Calculation of the liquid signals from tabulated data

As already explained in Chapter 2 the refractive index of a three-dimensional object can be described by its complex refractive index distribution $n(x, y, z) = 1 - \delta(x, y, z) + i\beta(x, y, z)$,

4. Quantitative phase-contrast computed tomography of a liquid phantom

where x , y , and z describe the coordinate system of the sample. In conventional absorption-contrast CT the imaginary part β is measured in the form of the linear attenuation coefficient μ of the x-rays. The Equation (3.15) in Section 3.1 describes the transmission projection $T^\theta(x')$ that is related to the attenuation coefficient $\mu(x', y')$. The mass attenuation coefficient (μ/ρ) is defined by the ratio of the linear attenuation coefficient μ and density ρ . For substances (subst.) that consist of a mixture of I components, each with mass attenuation coefficient $(\mu/\rho)_i$, with $i = 1, \dots, I$, the resulting mass attenuation coefficient is given by

$$\left(\frac{\mu}{\rho}\right)_{subst} = \sum_{i=1}^I \left(\frac{\mu}{\rho}\right)_i W_i, \quad (4.1)$$

where W_i is the weight fraction of the i -th component and the resulting linear attenuation coefficient simply is $\mu_{subst} = (\mu/\rho)_{subst} \cdot \rho_{subst}$, with the density of the substance ρ_{subst} .

In differential phase-contrast imaging, the variations in the real part of the refractive index $1 - \delta$ of the object are detected by analyzing the slight refraction of x-rays caused by the object. In addition to the absorption-contrast projection in Eq. (3.15), we measure the differential phase-contrast projection of refraction angles $\alpha^\Theta(x')$ like described in Equation (3.19) in Section 3.1. The refractive index decrement δ_{subst} of a mixture can be derived as a function of the x-ray wavelength λ and the density of the sample from the description in the book by J. Als-Nielsen [2] as

$$\delta_{subst} = \frac{r_e \lambda^2}{2\pi} \sum_{i=1}^I N_i f_i^0, \quad (4.2)$$

where $r_e = 2.82 \cdot 10^{-15} \text{m}$ is the classical electron radius, N_i is the atomic density of type i atoms given as atoms per unit volume, and f_i^0 is the real part of their atomic scattering factor in the forward direction. If the photon energy of the incident x-ray radiation lies considerably above the absorption edges, we may use the approximation $f_i^0 = Z_i$, with Z_i being the total number of electrons in the atom. The sum in Eq. (4.2) describes the overall electron density inside the sample. For mixtures with elemental weight fractions W_i , we substitute $N_i = (W_i \cdot N_A / A_i) \rho_{subst}$, with the atomic mass A_i of atom i and the Avogadro's number N_A , into Eq. (4.2).

The reconstruction of $\mu(x, y)$ and $\delta(x, y)$ was performed using the filtered backprojection algorithm as described in detail in Section 3.1.4 implemented in Matlab.

In a fan-beam setup the sensitivity of the grating interferometer is reduced by the factor r_1/l [29, Eq. 8], where r_1 is the source-to-sample distance and l is the source-to-G1 distance. To correct for this effect, the recorded phase projections were rescaled by multiplication by $(r_1/l)^{-1}$ prior to reconstruction.

We will use the contrast between two fluids in the absorption and the phase-contrast signal as a criterion for the sensitivity of the setup. Contrast can be described by the contrast-to-noise ratio

$$\text{CNR} = \frac{|S_a - S_b|}{\sigma_S}, \quad (4.3)$$

where S_a and S_b represent the measured signals $\Delta\mu$ (or $\Delta\delta$) of fluids a and b , respectively,

and $\sigma_S = (\sigma_a^2 + \sigma_b^2)^{1/2}$ is the standard deviation of the signal difference $|S_a - S_b|$, with the standard deviation σ_a and σ_b of the respective signals.

4.3. Measurement at a synchrotron radiation source

4.3.1. Introduction

Quantitative PC-CT measurements using different imaging methods have been reported by many authors [27, 59, 76, 68]. In the PhD work by T. Donath [28] the requirements needed for accurate quantitative computed tomography results are described in detail for a CT in absorption-contrast mode. Such measurements make a great demand on the accuracy of the whole imaging system. Demonstrating the quantitiveness of a PC-CT measurement is an important indication of the accuracy of the instrument.

Here, the results of a tomographic measurement of a self-made fluid phantom using a grating interferometer at the low-coherence synchrotron radiation wiggler beamline W2 are presented. The aim of the measurement was to use the tomographic reconstructions of the complex refractive index of well defined fluids to characterize the newly designed three-grating setup. The results of the tomographic measurements at two different photon energies (22 keV and 30 keV) will be presented. The contrast-to-noise ratios between different fluids at these photon energies will be used as a criterion for the sensitivity of the setup. The sensitivity at both energies will be compared and the results will be discussed.

4.3.2. Methods and materials

These measurements were carried out at the synchrotron radiation wiggler source of the beamline W2 (Section 2.3) using the x-ray grating interferometer setup introduced in Section 3. Two tomographic scans in a water tank (made of PMMA, 45 mm thickness of water in the beam direction) filled with demineralised water were performed at room temperature using the photon energies and Talbot orders giving the maximum visibility of the interference fringes as shown in Section 3.3.3:

1. 22 keV and the 7th Talbot order
2. 30 keV and the 5th Talbot order.

The fluid phantom constructed for this experiment consisted of five small cone-shaped low-density polyethylene (PE-LD) Eppendorf tubes with an outer diameter of about 5 mm in the scanned region. The fluids ethanol, water, glycerol, and two solutions of NaCl in water with different concentrations were used for the measurements described in this section (compare Table 4.1). For the measurement at 30 keV the Eppendorf tube filled with glycerol had to be removed, since air bubbles were produced by radiation damage during the tomographic scan. This phenomenon was not observed at 22 keV.¹

¹A possible explanation for the absence of the degassing effect at 22 keV is the significantly lower flux at this photon energy. Several strategies to reduce the gas-generation problem are discussed in Chapter 5.

4. Quantitative phase-contrast computed tomography of a liquid phantom

Figure 4.1 shows the fluid phantom that was suspended in the water bath from above, in front of the G1 grating with the Eppendorf tubes of the phantom roughly parallel to the rotation axis z . For the tomographic scan 361 projections at 22 keV and 451 projections at 30 keV were taken for projection angles from $\theta = 0^\circ$ to 360° . For each projection 8 phase steps over two periods of the grating G2 were recorded with a variable exposure time starting with 5 seconds at 22 keV and 0.3 seconds at 30 keV per image and increasing during the scan to compensate the decreasing synchrotron storage ring current. Please note that the exposure time is reduced by one magnitude from 22 keV to 30 keV due to the increasing photon flux at higher energies at this beamline, and the lower x-ray attenuation of the water tank at higher photon energies. After each image a reference image without the sample was taken to correct for any beam instabilities. Usually, the reference images are not taken after each image to make the measurement faster. But in this case we are interested in quantitative results and take as many reference images as possible. The number of projections at 30 keV was increased to enhance the statistics in the reconstruction as the visibility of the interference fringes falls to 15 % of those in the 22 keV configuration (see Chapter 3). At both photon energies the measurement was carried out with an on-chip binning of a factor two to reduce the read-out time of the CCD detector and the projections were binned by a factor of two prior to reconstruction to enhance the statistics in the reconstructions. The unbinned effective pixel size for both measurements was determined to be $6.3 \mu\text{m}$ using an automatic focussing procedure by means of an MTF calculation of a sharp strongly absorbing edge. Thus the resulting pixel size in the reconstructions was $25.2 \mu\text{m}$.

Figure 3.3 in Chapter 3 shows a schematic of the x-ray grating interferometer setup used for differential phase-contrast x-ray imaging at the low-coherence wiggler beamline W2 at DESY. The interferometer consists of an absorption source grating G0, a phase grating G1, and an analyzer absorption grating G2. The interferometer parameters are listed in Section 3.2. The phase grating G1 #1 was used for these measurements. The x-ray detector used in the experiments at the synchrotron source is described in Section 2.4.

In this approach we worked with a monochromatic beam ($\Delta E/E \approx 10^{-3}$ using a bent Laue monochromator crystal) and with a large distance from the source in the wiggler to the grating G1. In the absence of the source grating G0 (i.e. in the case of brilliant x-ray sources with sufficient inherent coherency) the geometric correction factor r_1/l of the grating interferometer is almost unity and can be neglected (again, r_1 represents the source-to-sample distance and l the source-to-G1 distance). Moreover, the use of a grating G0 only 3 m distant from the phase grating G1 leads to a reduction in the angular sensitivity of the setup by the correction factor described in Section 4.2. Thus, the recorded phase projections were rescaled by multiplication with $(r_1/l)^{-1} = [(3.0 \text{ m} - 0.055 \text{ m})/(3.0 \text{ m})]^{-1} = 1.01868$ prior to reconstruction.

The density of each fluid at room temperature [64] and their elemental weight fractions are listed in Table 4.1. These values were used for the calculation of the theoretical values for μ and δ . The calculated values will be denoted by the subscript 'c' e.g. as μ_c and δ_c . For the dilution series of NaCl in water the density as a function of salt concentration was used in the calculation. The values of δ_c were calculated using the tabulated data of Kissel [84]. Please note that these measurements were carried out in a water tank, i.e. relative to water, thus the theoretical values are given relative to those of water as $\Delta\mu_c = \mu_c - \mu_c(\text{H}_2\text{O})$ and

4.3. Measurement at a synchrotron radiation source

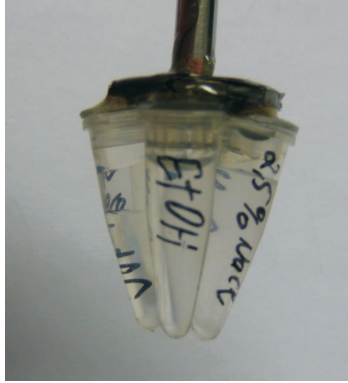


Figure 4.1.: Picture of the fluid phantom constructed for the measurements at the synchrotron radiation source. The bottom region of the phantom was scanned, where the outer diameters of the tubes are ≈ 5 mm.

$\Delta\delta_c = \delta_c - \delta_c(\text{H}_2\text{O})$ for comparison with the experimental results. The measurement in water tank had two important advantages: 1. The surrounded water avoided phase jumps at the edges of the tubes, which would distort the quantitative analysis, and 2. It will provide results comparable to the well known Hounsfield Units in the conventional medical CT in absorption mode, which are also defined relatively to water.

Table 4.1.: Density and elemental composition of the fluids used at the synchrotron radiation source at room temperature ($T = 20^\circ\text{C}$). These values were used in the calculation of $\Delta\mu_c$ and $\Delta\delta_c$ listed in the Tables 4.2 and 4.3.

Solution [wt.%]	Identifier	Density [g/cm ³]	Elemental weight fraction W_i				
			H [wt.%]	O [wt.%]	C [wt.%]	Na [wt.%]	Cl [wt.%]
H ₂ O (demineralised)	H ₂ O	0.9982	11.19	88.81	–	–	–
glycerol (85% pure)	Gly	1.2192	9.06	57.65	33.29	–	–
ethanol (99.9% pure)	EtOH	0.7894	13.13	34.73	52.14	–	–
H ₂ O+NaCl 2.5%	H ₂ O-NaCl2.5	1.0160	10.91	86.59	–	0.98	1.52
H ₂ O+NaCl 5%	H ₂ O-NaCl5	1.0340	10.63	84.37	–	1.97	3.03

4.3.3. Results and Discussion

Figures 4.2(a) and 4.2(b), show the reconstructions of $\Delta\mu$ and $\Delta\delta$ respectively, from the same slice of the fluid phantom measured at 22 keV at the synchrotron radiation source. In Figures 4.3(a) and 4.3(b) the reconstructions for 30 keV are presented. For both figures (Fig. 4.2 and Fig. 4.3) and for the determination of measured values 20 tomographic slices were averaged along the z -axis to enhance the signal-to-noise ratio in the reconstructed slices. From these reconstructions experimental values for $\Delta\mu$ and $\Delta\delta$ were determined from the mean value over a circular averaging region of 100 pixels diameter containing 7857 voxels within each tube (in total 7857×20 voxels). Also the standard deviations σ_μ and σ_δ over all pixels were determined. Note that the given deviations represent the error of the mean value, which is a factor of $(\text{number of pixels})^{-1/2}$ smaller than the standard deviation of one pixel (refer to [36]). The measured values together with the mean-value deviations for the measurements

4. Quantitative phase-contrast computed tomography of a liquid phantom

at 22 keV and 30 keV are given in Tables 4.2 and 4.3, respectively. The scatter plots in Figure 4.4 and 4.5 compare the measured $\Delta\mu$ and $\Delta\delta$ values to the calculated $\Delta\mu_c$ and $\Delta\delta_c$ values for each photon energies, respectively.

The Eppendorf tube filled with demineralised water serves as a control of the zero value and should be measured as zero in both refractive index and attenuation coefficient measurements. For both photon energies the values for water coincide within one standard deviation with zero, as expected. The values for ethanol and the NaCl2.5 dilution in water match the calculated values also within one standard deviation for both energies. But the values for the NaCl5 solution and especially glycerol measured at 22 keV show strong deviations in μ and δ . Furthermore, the deviation of the δ values increases for the lower photon energy. One possible reason is the fact that these fluids produce a strong contrast in both signals, especially compared to the enclosing polyethylene tube. At such sharp interfaces between materials scattering occurs and leads to a decrease in the visibility of the Talbot fringes and an error in the absolute values of μ and δ . This error increases with lower photon energy since the setup becomes more sensitive when increasing the Talbot order and decreasing the energy. The reason for the strong deviations of the measured μ values for glycerol from the calculated values can be the slightly wrong purity of the glycerol. The theoretical values are calculated for an 85 % pure glycerol, as for the purity of the commercial available glycerol the worse value was declared on the container. This means, that the purity of the glycerol might be higher that would lead to higher measured μ values.

Table 4.2.: Measured and calculated attenuation coefficients $\Delta\mu$ and refractive index decrements $\Delta\delta$ for the fluids in the phantom (relative to water) for a photon energy of 22 keV at room temperature ($T = 20^\circ\text{C}$). The given deviations σ_μ and σ_δ were determined for each averaging region describing the variation about the mean value. The calculated $\Delta\mu_c$ and $\Delta\delta_c$ values were determined for the photon energies of 22 keV. The data is plotted in Fig. 4.4.

Identifier	$\Delta\mu \pm \sigma_\mu$ [$10^{-2}/mm$]	$\Delta\mu_c$ [$10^{-2}/mm$]	$\Delta\delta \pm \sigma_\delta$ [10^{-8}]	$\Delta\delta_c$ [10^{-8}]
H ₂ O	0.03 ± 0.06	0	0.005 ± 0.05	0
Gly	0.41 ± 0.06	0.24	10.15 ± 0.08	9.44
EtOH	-2.57 ± 0.06	-2.58	-8.59 ± 0.07	-9.33
H ₂ O-NaCl2.5	1.05 ± 0.07	1.01	0.68 ± 0.08	0.69
H ₂ O-NaCl5	1.93 ± 0.06	2.06	1.22 ± 0.05	1.37

4.3.4. Contrast-to-noise ratios

We can compare the performance of the setup at two different photon energies using these measurements. The contrast between the measured refractive indices of two fluids in the absorption and the phase-contrast signal, described by the contrast-to-noise ratio (CNR) in Eq. 4.3, is used as parameter for the comparison. The CNR for different fluids at both energies are listed in Table 4.4.

The comparison of the contrast-to-noise ratios at different energies shows the expected behavior: The CNR_μ and CNR_δ for 22 keV are significantly higher than those for 30 keV. The

4.3. Measurement at a synchrotron radiation source

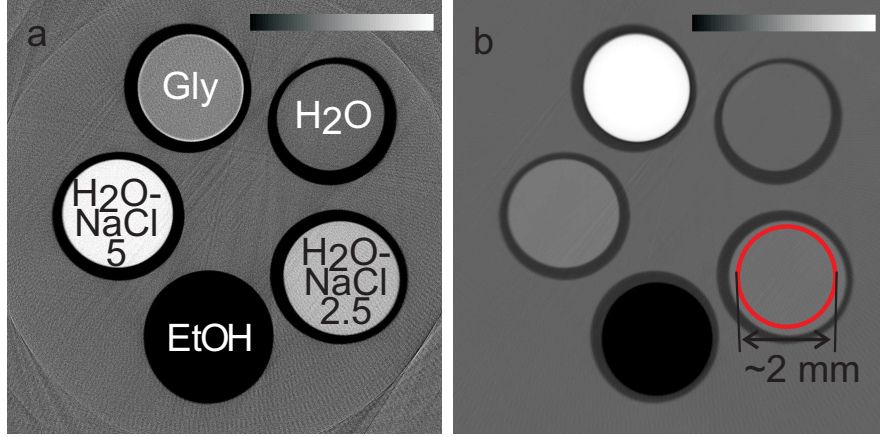


Figure 4.2.: Tomographic reconstructions from the same slice of the phantom at 22 keV showing (a) the attenuation coefficient $\Delta\mu(x, y)$ and (b) the refractive index decrement $\Delta\delta(x, y)$ measured at the synchrotron radiation source. The images are windowed (from black to white) between the range of $-2.1 \cdot 10^{-2}$ to $0.6 \cdot 10^{-2} \text{ mm}^{-1}$ in (a) and from $-8.2 \cdot 10^{-8}$ to $0.2 \cdot 10^{-8}$ in (b). The fluids in the five polyethylene tubes of the phantom have been labelled with their identifiers according to the fluid descriptions in Table 4.1. A centred, circular averaging region, as shown for one tube in (b), was defined for each tube to obtain the experimental values given in Table 4.2.

Table 4.3.: Measured and calculated attenuation coefficients $\Delta\mu$ and refractive index decrements $\Delta\delta$ for the fluids in the phantom (relative to water) for a photon energy of 30 keV at room temperature ($T = 20 \text{ }^\circ\text{C}$). The calculated $\Delta\mu_c$ and $\Delta\delta_c$ values were determined for the photon energies of 30 keV. The data is plotted in Fig. 4.5.

Identifier	$\Delta\mu \pm \sigma_\mu$ [$10^{-2}/\text{mm}$]	$\Delta\mu_c$ [$10^{-2}/\text{mm}$]	$\Delta\delta \pm \sigma_\delta$ [10^{-8}]	$\Delta\delta_c$ [10^{-8}]
H ₂ O	-0.003 ± 0.06	0	0.006 ± 0.04	0
EtOH	-1.18 ± 0.05	-1.23	-4.66 ± 0.04	-5.01
H ₂ O-NaCl2.5	0.43 ± 0.06	0.41	0.39 ± 0.04	0.37
H ₂ O-NaCl5	0.78 ± 0.05	0.84	0.68 ± 0.04	0.74

Table 4.4.: Signal-to-noise ratios CNR_μ and CNR_δ for the photon energies 22 keV and 30 keV of the synchrotron setup. The data is calculated from the values in Tables 4.2 and 4.3.

Fluids	$CNR_\mu(22\text{keV})$	$CNR_\delta(22\text{keV})$	$CNR_\mu(30\text{keV})$	$CNR_\delta(30\text{keV})$
H ₂ O/EtOH	30.64	99.91	15.1	82.5
H ₂ O/H ₂ O-NaCl2.5	11.1	7.2	4.7	6.8
H ₂ O/H ₂ O-NaCl5	22.4	17.2	10.0	11.9
EtOH/H ₂ O-NaCl2.5	40.7	87.2	20.6	88.2
EtOH/H ₂ O-NaCl5	53.0	114.0	27.7	94.4
H ₂ O/Gly	4.5	107.5	-	-
EtOH/Gly	35.1	176.3	-	-

4. Quantitative phase-contrast computed tomography of a liquid phantom

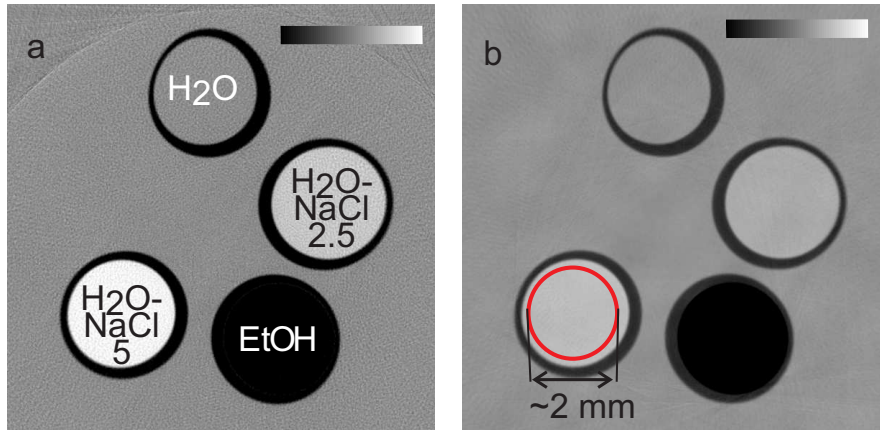


Figure 4.3.: Tomographic reconstructions from the same slice of the phantom at 30 keV showing (a) the attenuation coefficient $\Delta\mu(x, y)$ and (b) the refractive index decrement $\Delta\delta(x, y)$ measured at the synchrotron radiation source. The images are windowed (from black to white) between the range of $-1.56 \cdot 10^{-2}$ to $0.26 \cdot 10^{-2} \text{ mm}^{-1}$ in (a) and from $-3.5 \cdot 10^{-8}$ to $0.6 \cdot 10^{-8}$ in (b). The fluid phantom contains only 4 polyethylene tubes as the tube with glycerol had to be removed. The tubes have been labelled with their identifiers according to the fluid description in Table 4.1. A centred, circular averaging region, as shown for one tube in (b), was defined for each tube to obtain the experimental values given in Table 4.3.

CNR_{μ} increases by a factor of 2, while the CNR_{δ} is enhanced by an average factor of 1.2. Several effects should be considered in this comparison. As shown in Chapter 3, the visibility of the interference fringes changes from 32 % at 22 keV to 15 % at 30 keV. This seems to be the main contribution to the decrease in the contrast-to-noise ratio and is due to the higher effectiveness of the gold gratings at lower photon energies.

There are three other effects influencing the CNR of the measurements that have to be mentioned here: 1.) At lower photon energies both the attenuation and the phase shift increase, but this is offset by the decreasing flux at 22 keV due to the increased self-absorption in the monochromator crystals and in the water tank. 2.) Furthermore, at 30 keV the photon flux is higher, but the gold grating $G2$ starts to become transparent to the x-rays. Thus, the fringe-visibility decreases towards higher photon energies. 3.) For the tomography scan at 30 keV more projections were recorded, taking advantage of the shorter exposure times, to compensate for the decreasing visibility.

All these effects make a direct comparison difficult, but nevertheless, the results are representative for a measurement with corresponding settings. Thus, they can be used to find the optimum settings for the object under investigation, as they characterise the imaging system at the corresponding photon energy.

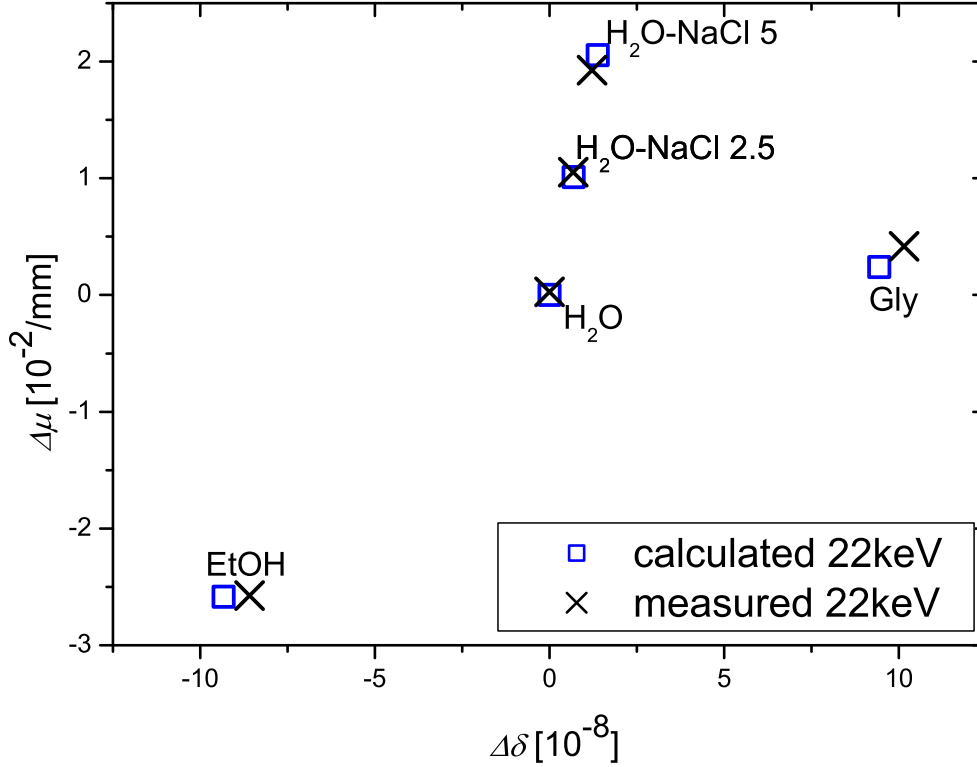


Figure 4.4.: Plot of measured and calculated attenuation coefficients $\Delta\mu$, $\Delta\mu_c$ and refractive index decrements $\Delta\delta$, $\Delta\delta_c$ for 22 keV. Black crosses represent the measured and blue squares the calculated values for 22 keV. The data to the plot is given in the table 4.2.

4.3.5. Conclusions

The results obtained at the synchrotron radiation source show that at both photon energies (22 keV and 30 keV) the measured mean complex refractive index values for almost all fluids were in good agreement with the theoretical values. The deviations in measured values for ethanol and NaCl5 solution in water at both photon energies could be explained by the presence of scattering at the container interfaces decreasing the fringe visibility and leading to errors in the measurement of absolute values. The reason for the high deviation of the μ value for glycerol measured at 22 keV can be the slightly wrong purity of the glycerol. Such errors are not easy to correct for. Beside these deviations, both measurements demonstrated the accuracy of the grating-based phase-contrast tomography as a quantitative imaging method.

The contrast-to-noise ratios between the measured refractive indices for different fluids were calculated for both measurements. This allowed the accuracy and sensitivity of the

4. Quantitative phase-contrast computed tomography of a liquid phantom

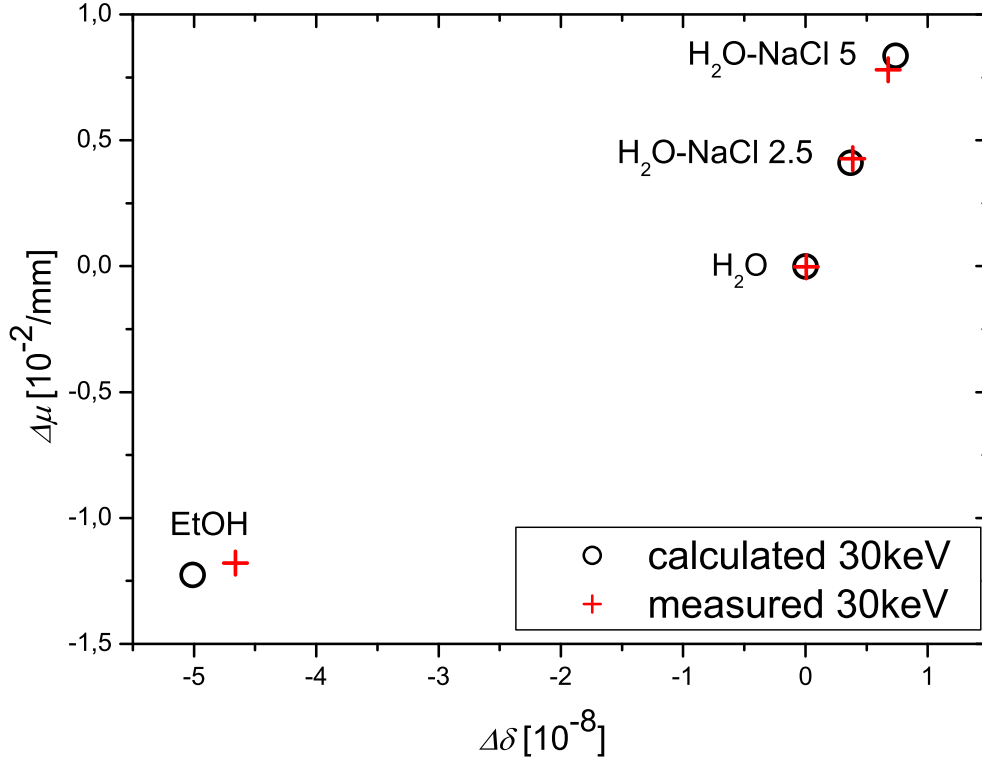


Figure 4.5.: Plot of measured and calculated attenuation coefficients $\Delta\mu$, $\Delta\mu_c$ and refractive index decrements $\Delta\delta$, $\Delta\delta_c$ for 30 keV. Red crosses represent the measured and black circles the calculated values for 30 keV. The data to the plot is given in the table 4.3.

setup at the corresponding photon energies to be characterised. Although the measurements of the fluid phantom were performed with the same imaging system, various effects discussed above make the direct comparison using the CNRs difficult. We came to the conclusion that nevertheless the results represent the performance of the grating-based synchrotron setup at different photon energies and can be used for choosing the optimum settings for further investigations. According to that, one should choose the lower photon energies for very weakly absorbing samples to achieve enough contrast in the phase-signal. When studying metal alloys, like aluminium or magnesium alloys, the higher photon energy should be chosen. In this way samples producing very strong phase shifts, can also be investigated with PC imaging, that would lead to phase-wrapping artifacts at a lower photon energy with higher sensitivity. The ability to choose the photon energy from a number of available energies to achieve the best conditions for every object investigated with PC-CT and to image it without polychromatic artifacts with high spatial resolution makes the grating interferometer at the synchrotron radiation source a powerful method.

4.4. Measurement at a conventional x-ray tube

4.4.1. Introduction

A research stay of three months at the Laboratory for Micro- and Nanotechnology at the Paul Scherrer Institut (PSI, Villigen, Switzerland) was a part of this work. During this stay the grating-based phase-contrast method at low-brilliance x-ray sources was studied. Subsequently, the grating interferometer described in this work was designed and installed at the low-brilliance synchrotron wiggler source W2 in cooperation with PSI, TU München and KIT Karlsruhe.

The aim of the work at PSI was to demonstrate the simultaneous determination of the attenuation coefficient and the refractive index decrement distribution inside an object in three dimensions using a grating interferometer with a polychromatic low-brilliance x-ray tube. Here the experimental results of the investigation on the quantitateness and accuracy of this method are presented. These results were published in Herzen *et al.* 'Quantitative phase-contrast tomography of a liquid phantom using a conventional x-ray tube source', OPTICS EXPRESS Vol. 17, No. 12, 2009 [49]. For this study, a similar phantom as described in previous section consisting of several tubes filled with chemically well-defined liquids was built and measured in PC-CT. The study was largely motivated by the fact that modern medical CT applications increasingly rely on quantitative interpretation of the tomographic gray-scale images, e.g. in the assessment of bone density in the context of osteoporosis.

4.4.2. Methods and materials

For the reconstruction of the object's $\mu(x, y)$ and $\delta(x, y)$, from the two sets of projections $T^\Theta(x')$ and $\alpha^\Theta(x')$ respectively, a filtered back-projection reconstruction algorithm was applied as described in detail in Chapter 2, Section 2.1. In this approach we worked with a fan-beam setup, where the sensitivity of the grating interferometer is reduced as mentioned in the previous section. To correct for this effect, the recorded phase projections were multiplied with the factor $(r_1/l)^{-1} = [(1.4 \text{ m} - 0.078 \text{ m})/(1.4 \text{ m})]^{-1} = 1.059$ prior to reconstruction.

Figure 4.6 shows the self-built phantom consisting of thirteen small cylindrical low-density polyethylene (PE-LD) tubes with outer diameters of 8 mm and volumes of 0.5 ml that were filled with fluids of well defined chemical composition (see Table 4.5). To cover a wide range of attenuation coefficients and refractive index decrements, we mixed different pure liquids (ethanol, water, glycerol) and salts (NaI, NaCl).

Differential phase-contrast x-ray imaging and CT were carried out using an x-ray grating interferometer as shown schematically in Fig. 4.7 and described in Section 2.3.1. The interferometer consists of a source grating G0, a phase grating G1, and an analyzer absorption grating G2. The source grating G0, which is placed close to the x-ray tube anode, allows the use of x-ray sources with square-millimetre-sized focal points [83]. The signal is formed by the two gratings G1 and G2 due to the Talbot self-imaging effect [77]. The interferometer that was used here was designed for an x-ray energy of 28 keV and consisted of three gratings with respective periods of $p_0 = 14.2 \mu\text{m}$, $p_1 = 3.5 \mu\text{m}$, and $p_2 = 2.0 \mu\text{m}$ and respective structure

4. Quantitative phase-contrast computed tomography of a liquid phantom



Figure 4.6.: Picture of the self-made fluid phantom used for the measurements with the x-ray tube. The phantom consists of 13 cylindrical polyethylene tubes with outer diameters of 8 mm filled with the fluids listed in Table 4.5.

Table 4.5.: Density and elemental composition of the fluids. These values were used in the calculation of $\Delta\mu_c$ and $\Delta\delta_c$ listed in Table 4.6.

Solution [wt.%]	Identifier	Density [g/cm ³]	Elemental weight fraction W_i					
			H [wt.%]	O [wt.%]	C [wt.%]	Na [wt.%]	Cl [wt.%]	I [wt.%]
H ₂ O (demineralized)	H ₂ O	0.9982	11.19	88.81	–	–	–	–
glycerol (99.5%)	Gly	1.26	8.76	52.12	39.13	–	–	–
ethanol (p.a. 99.9%)	EtOH	0.7894	13.13	34.73	52.14	–	–	–
H ₂ O+NaCl 1.25%	H ₂ O-NaCl1.25	1.0072	11.05	87.70	–	0.49	0.76	–
H ₂ O+NaCl 2.5%	H ₂ O-NaCl2.5	1.0160	10.91	86.59	–	0.98	1.52	–
H ₂ O+NaCl 5%	H ₂ O-NaCl5	1.0340	10.63	84.37	–	1.97	3.03	–
H ₂ O+NaCl 10%	H ₂ O-NaCl10	1.0707	10.07	79.93	–	3.93	6.07	–
ethanol+NaI 1.25%	EtOH-NaI1.25	–	12.96	34.29	51.49	0.19	–	1.06
ethanol+NaI 2.5%	EtOH-NaI2.5	–	12.80	33.86	50.84	0.38	–	2.12
ethanol+NaI 5%	EtOH-NaI5	–	12.47	32.99	49.54	0.77	–	4.23
ethanol (75%) + glycerol (25%)	EtOH75-Gly25	–	–	–	–	–	–	–
ethanol (50%) + glycerol (50%)	EtOH50-Gly50	–	–	–	–	–	–	–
ethanol (25%) + glycerol (75%)	EtOH25-Gly75	–	–	–	–	–	–	–

heights of $h_0 = 42 \mu\text{m}$, $h_1 = 36 \mu\text{m}$, and $h_2 = 26 \mu\text{m}$. The distance between G_0 and G_1 was 1.40 m and the distance between G_1 and G_2 was 0.198 m, corresponding to the fifth fractional Talbot distance. The gratings were produced on 4 inch silicon wafers in a fabrication process involving photolithography, deep etching into silicon, and (for the absorption gratings G_0 and G_2) electroplating of gold [25].

As x-ray source we used a Seifert ID 3000 x-ray generator operated at 40 kV and 25 mA with a tungsten (W) line focus tube (DX-W8 \times 0.4-L) producing a typical bremsstrahlung spectrum overlaid with the fluorescence K_α line of tungsten at 59 keV. The influence of the polychromatic illumination on the performance of the grating interferometer is discussed in Chapter 3. Due to the inclination of the target with respect to the optical axis of 6° , the effective source size was $0.8 \text{ (h)} \times 0.4 \text{ (v)} \text{ mm}^2$. A PILATUS 100K pixel detector consisting of an array of 487×195 pixels with a pixel size of $0.172 \times 0.172 \text{ mm}^2$ was used to record images. Its detection efficiency, determined by the probability of absorbing an x-ray in the $320 \mu\text{m}$ -thick Si sensor, is $\approx 10\%$ at 28 keV.

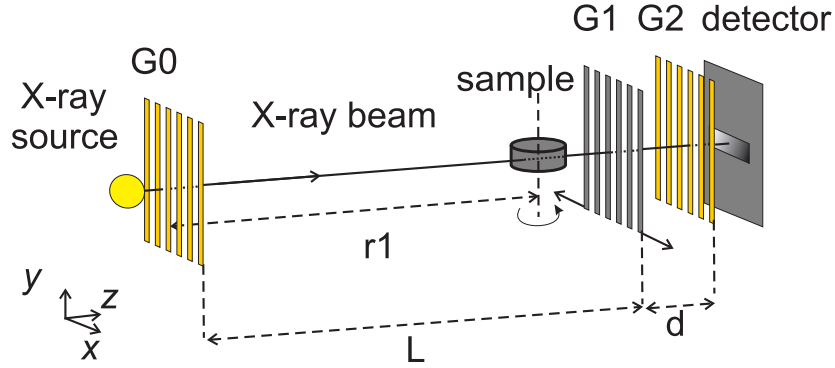


Figure 4.7.: X-ray grating interferometer for differential phase-contrast imaging with an x-ray tube. A phase object in the beam path causes a slight deflection of x-rays changing the locally transmitted intensity through the arrangement formed by the gratings G1 and G2. The sample is placed on a tomographic rotation stage.

The measurements were carried out at room temperature in a water tank (made of PMMA, 50 mm thickness of water in the beam direction) filled with demineralised water. The stationary water tank was placed in front of the G1 grating. The fluid phantom was mounted on the rotation stage with the cylindrical tubes of the phantom parallel to the rotation axis z (see Fig. 4.7) and immersed in the tank. For the tomographic scan, 361 projections were taken for projection angles from $\Theta = 0^\circ$ to 360° . For each projection 16 phase steps covering two periods of the analyser grating G_2 were recorded with an exposure time of 10 seconds per image. The visibility of the interference pattern behind a 50 mm PMMA water tank with a wall thickness of 3 mm was determined to 8%.

To obtain the phase-contrast and the conventional projection, a set of raw images was recorded for different positions of the grating G1. From this so-called phase-stepping scan (described in more detail in Chapter 3) both projections were computed. These projections can be used directly as input for the filtered back-projection reconstruction algorithms, i.e., numerical implementations of Eqs. 3.24 and 3.25 as explained in Section 2.1.

The calculation of theoretical values for μ and δ for each fluid was performed using their density at room temperature [64] and their elemental weight fractions, both listed in Table 4.5. In the following we denote calculated values by a subscript 'c' e.g. as μ_c and δ_c . For the dilution series of NaCl in water, the density as a function of salt concentration was used in the calculation. Since we could not find tabulated data for the density of the dilution series of NaI in ethanol and for the ethanol-glycerol mixtures, we did not calculate theoretical values for these mixtures. To calculate δ_c we used the tabulated data of Kissel² and for the calculation of μ_c , we used the data of Plechaty *et al.* [84]. Since our measurements were carried out in a water tank, i.e. relative to water, we give all measured and theoretical values relative to those of water as $\Delta\mu_c = \mu_c - \mu_c(\text{H}_2\text{O})$ and $\Delta\delta_c = \delta_c - \delta_c(\text{H}_2\text{O})$.

Both μ and δ strongly depend on the x-ray energy. For the comparison of measured and

²For the calculation of δ_c the values of f^1 for elastic photon-atom scattering, anomalous scattering factors, tabulated by L. Kissel were taken from the file flf2.asf.Kissel.dat of the DABAX library [1].

4. Quantitative phase-contrast computed tomography of a liquid phantom

calculated values we thus have to select an effective photon energy, for which we calculate the theoretical data. The measurement of μ and δ is generally carried out with two different effective x-ray energies due to two main reasons: 1.) The image formation processes of the conventional and the phase-contrast data are intrinsically different, and 2.) the specific energy-dependent efficiency of the x-ray gratings leads to a different weighting of the initial energy spectrum (for more details, see [3, 30]). Thus, we use two different effective x-ray energies E_μ and E_δ , which we determine from the measured data of ethanol as described below. It should be noted that this approach is necessary since a non-energy dispersive detector was used.

4.4.3. Results and Discussion

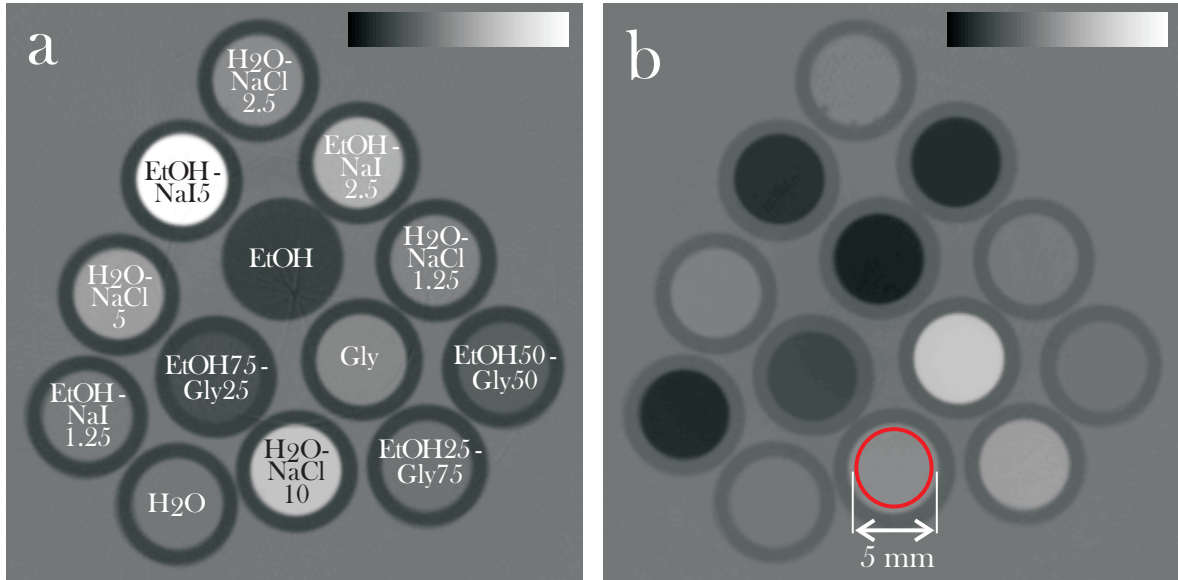


Figure 4.8.: Tomographic reconstructions from the same slice of the phantom showing (a) the attenuation coefficient $\Delta\mu(x, y)$ and (b) the refractive index decrement $\Delta\delta(x, y)$ measured at the x-ray tube. The colour bar (from black to white) ranges from $-2.0 \cdot 10^{-2}$ to $3.0 \cdot 10^{-2} \text{ mm}^{-1}$ in (a) and from $-7.5 \cdot 10^{-8}$ to $11.3 \cdot 10^{-8}$ in (b). The fluids in the 13 polyethylene tubes of the phantom have been labelled with their identifiers according to the fluid description in Table 4.5. A centred, circular averaging region, as shown for one tube in (b), was defined for each tube to obtain the experimental values given in Table 4.6.

Reconstructions of $\Delta\mu$ and $\Delta\delta$ from the same slice of the phantom are shown in Figs. 4.8(a) and 4.8(b), respectively. For the specific reconstructions shown in Fig. 4.8, 55 tomographic slices were averaged (along the z -direction) to increase the signal-to-noise ratio. From these reconstructions experimental values for $\Delta\mu$ and $\Delta\delta$ were determined from the mean value over a circular averaging region of 30 pixels diameter containing 709 voxels within each tube (in total 709×55 voxels). Also the standard deviations σ_μ and σ_δ over all pixels were determined. Note that the given deviations represent the error of the mean value, which is a factor of $(\text{number of pixels})^{-1/2}$ smaller than the deviation of one pixel (refer to [36]). The

4.4. Measurement at a conventional x-ray tube

Table 4.6.: Measured and calculated attenuation coefficients $\Delta\mu$ and refractive index decrements $\Delta\delta$ for all fluids in the phantom (relative to water). The deviations σ_μ and σ_δ describe the error of the mean value within each averaging region. The calculated $\Delta\mu_c$ and $\Delta\delta_c$ values were determined for effective photon energies of $E_\mu = 30.1$ keV and $E_\delta = 28.3$ keV, respectively, as discussed in the text. The data is plotted in Fig. 4.9.

Identifier	$\Delta\mu \pm \sigma_\mu$ [$10^{-2}/mm$]	$\Delta\mu_c(E_\mu)$ [$10^{-2}/mm$]	$\Delta\delta \pm \sigma_\delta$ [10^{-8}]	$\Delta\delta_c(E_\delta)$ [10^{-8}]
H ₂ O	0.023 ± 0.019	0	-0.015 ± 0.049	0
Gly	0.358 ± 0.022	0.382	5.831 ± 0.077	6.736
EtOH	-1.220 ± 0.054	-1.219	-5.632 ± 0.076	-5.634
H ₂ O-NaCl1.25	0.247 ± 0.028	0.201	0.122 ± 0.053	0.208
H ₂ O-NaCl2.5	0.467 ± 0.022	0.406	0.486 ± 0.022	0.413
H ₂ O-NaCl5	0.878 ± 0.028	0.827	0.662 ± 0.028	0.829
H ₂ O-NaCl10	1.796 ± 0.018	1.707	1.388 ± 0.028	1.670
EtOH-NaI1.25	0.065 ± 0.022	–	-5.183 ± 0.055	–
EtOH-NaI2.5	1.272 ± 0.028	–	-5.013 ± 0.045	–
EtOH-NaI5	3.539 ± 0.038	–	-4.782 ± 0.038	–
EtOH75-Gly25	-0.906 ± 0.027	–	-3.361 ± 0.066	–
EtOH50-Gly50	-0.540 ± 0.025	–	-0.340 ± 0.042	–
EtOH25-Gly75	-0.115 ± 0.017	–	2.767 ± 0.044	–

measured values together with the standard deviations are given in Table 4.6. Figure 4.9 shows a scatter plot of the measured values $\Delta\mu$ and $\Delta\delta$.

The tube with demineralised water in the phantom serves as a control of the zero value. Water should be measured as zero, as the measurement was carried out in a water tank, i.e. relative to water. We found that the measured values for water $\Delta\mu = 0.023 \pm 0.019 \cdot 10^{-2} \text{mm}^{-1}$ and $\Delta\delta = -0.015 \pm 0.049 \cdot 10^{-8}$ coincide within one standard deviation with zero. A second very important result is the fact that the measured values for $\Delta\mu$ and $\Delta\delta$ change in the correct proportion depending on the concentration for all three fluid series H₂O-NaCl, EtOH-NaI, and EtOH-Gly which is not self-evident for a measurement with a polychromatic x-ray source. In the case of a wide photon-energy spectrum, the influence on the measured values may vary with the salt concentration in the fluids.

Effective energies for the μ and the δ measurements were determined by matching the measured and the calculated data for ethanol, which has comparatively large signals in both μ and δ . The effective energies were determined to be $E_\mu = 30.1$ keV and $E_\delta = 28.3$ keV, both determined with 0.1 keV resolution. Note that both effective energies and especially E_δ are close to the interferometer design energy of 28 keV. Using these effective energies we observe that the measured values closely match the theoretically calculated values for most fluids. Only the fluids with high μ and δ values (H₂O-NaCl5, H₂O-NaCl10 and Gly) show a trend of having overly low δ values in the measurement. This might be attributed to beam-hardening effects or to a slightly wrong effective energy E_δ due to errors in the ethanol measurement that was used for the determination of the effective energies. One possible source of error (sub-pixel) in the values for the μ and the δ for ethanol might be the vicinity of the ethanol tube to the centre of rotation and a small error in the determination of the centre of rotation.

4. Quantitative phase-contrast computed tomography of a liquid phantom

As discussed in the PhD thesis of T. Donath [28, Chapter (5)], even very small errors in determination of the centre of rotation lead to systematic errors in the tomographic reconstruction. In our case the centre of rotation was determined with one pixel resolution.

The contrast between two fluids in the absorption and the phase-contrast signal can be described by the contrast-to-noise ratio in Eq. 4.3. From the reconstructions in Fig. 4.8 and the plot in Fig. 4.9 it is obvious that fluids can be much better distinguished by using both complementary signals instead of only one.

For example for the fluids H₂O-NaCl1.25 and glycerol (Gly) we find $\text{CNR}_\mu = (0.358 - 0.247) / (0.022^2 + 0.028^2)^{1/2} = 3.12$ looking at the attenuation coefficients, but looking at the refractive index decrements instead, we find a much higher contrast-to-noise ratio of $\text{CNR}_\delta = (5.831 - 0.122) / (0.077^2 + 0.053^2)^{1/2} = 61.07$. Similarly, we find for the fluids H₂O and EtOH-NaI1.25 contrast-to-noise ratios of $\text{CNR}_\mu = 1.44$ and $\text{CNR}_\delta = 70.16$. These substances can thus hardly be distinguished by their attenuation coefficients alone, but easily by looking at their refractive index decrements. Conversely, the fluids EtOH and EtOH-NaI1.25 show less contrast for the refractive index decrement ($\text{CNR}_\delta = 4.79$), but can be easily distinguished by looking at the complementary attenuation coefficient ($\text{CNR}_\mu = 22.04$).

4.4.4. Conclusions

The results clearly illustrate that PC-CT, by simultaneously yielding phase-contrast and attenuation-contrast images, provides significantly more information than standard laboratory CT. It has particularly been shown that the approach can yield quantitative volume information of the distribution of the refractive index decrement δ and the attenuation coefficient μ . By exploiting both the absorption and the phase-contrast signal it is possible to distinguish substances with weak contrast in either one of the signal channels, and to generally improve the specificity of the measurement by using PC-CT. The presented experimental results obtained from a fluid phantom agree well with the theoretical expectations. The quantitateness of the results, obtained with a conventional polychromatic x-ray tube source, makes this method of great interest for a wide range of quantitative x-ray CT applications, including future medical diagnostics, industrial non-destructive testing, and other research areas.

The limited spatial resolution (here limited by the pixel size of 172 μm) and the effects of polychromatic radiation are compensated by the most important advantage of this method - the availability of x-ray tube sources even for small laboratories. Thus, the method is useful for applications with high throughput like medical imaging or industrial non-destructive testing. Here, radiation dose or cost considerations demand precise detection of diseases or defects with the most efficient x-ray measurement.

4.5. Summary

Tomography measurements of a self-made fluid phantom using the grating interferometer at a low-coherence synchrotron wiggler source have been made using two different photon energies (22 keV, 7th Talbot order; 30 keV, 5th Talbot order). The results show a high accuracy

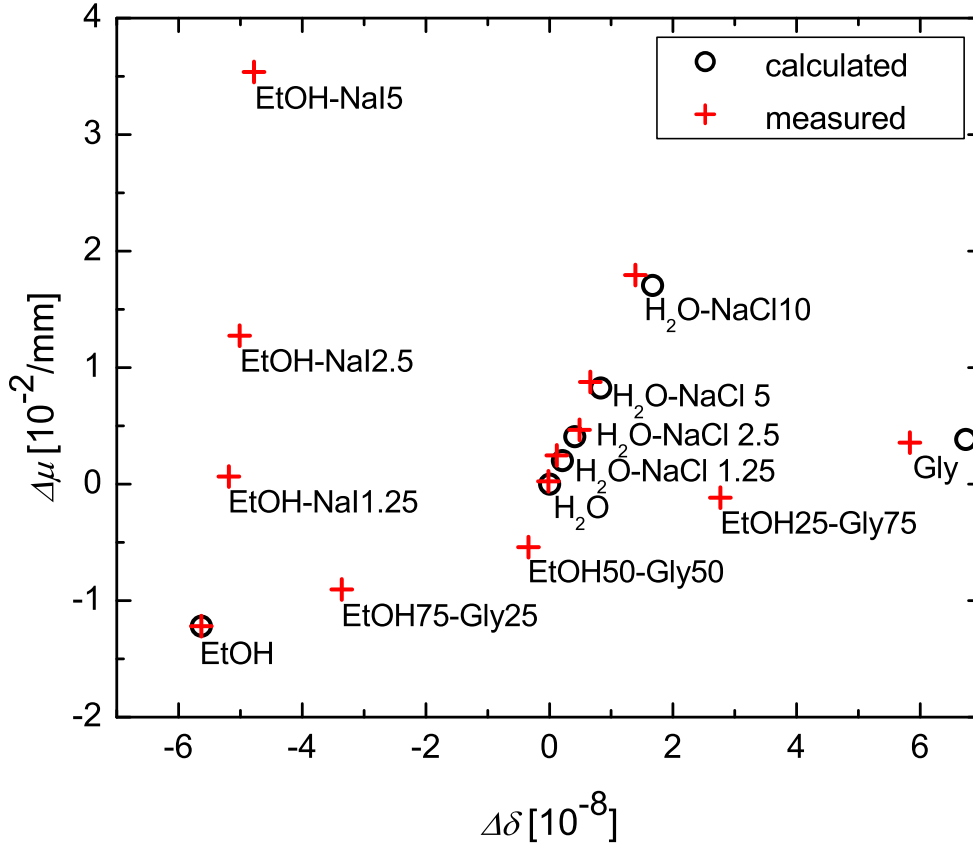


Figure 4.9.: Scatter plot of measured and calculated attenuation coefficients $\Delta\mu$, $\Delta\mu_c$ and refractive index decrements $\Delta\delta$, $\Delta\delta_c$. The plot shows the data given in Table 4.6.

in providing reliable quantitative information about the distribution of the refractive index decrement δ and the attenuation coefficient μ . The small deviations from the theoretic values could be explained by the presence of increased scattering at the plastic container interfaces decreasing the fringe visibility and leading to an error in the determination of absolute values.

Furthermore, the contrast-to-noise ratios (CNRs) of different fluids measured with the synchrotron setup at different photon energies could be used to quantify the performance of the setup at both energies. Although, a range of effects discussed have an influence on the CNRs of the measurements, the CNRs are representative of the measurement at the corresponding settings. Thus, the CNRs can be used to characterise the sensitivity of the synchrotron setup helping to choose the optimum parameters for further investigations.

The results obtained during a research stay at the Laboratory for Micro- and Nanotechnology at the Paul Scherrer Institut in Switzerland, using the grating interferometer setup with

4. Quantitative phase-contrast computed tomography of a liquid phantom

a polychromatic x-ray tube have also been presented. The measured attenuation coefficients μ and the refractive index decrements δ of the liquids agree well with the calculated theoretical values. The small deviations could be explained by polychromatic artifacts and an error in determination of the centre of rotation. By combining both the absorption and the phase-contrast signals, substances with weak contrast in either one of the signal channels can be easily distinguished. The accuracy of the results despite using polychromatic illumination with low flux, and the high availability of x-ray tube sources for small laboratories makes this method very interesting for a large field of applications.

5. Applications

5.1. Introduction

In this chapter selected applications are presented using the imaging setup at the beamline W2 in both modes, the absorption and the newly designed phase-contrast mode. The Section 5.2 of this Chapter deals with imaging of laser-welded materials presenting the results of a tomographic characterisation of a laser-welded aluminium alloy T-joint in absorption-contrast mode [47]. The assets and drawbacks of this method for imaging of such materials are pointed out. In addition, projections of aluminium and magnesium alloy laser-welds are presented using the grating-based phase-contrast setup. The projections include three different information simultaneously and demonstrate the high potential of the grating-based imaging method in the field of materials characterisation.

In the Section 5.3 tomographic reconstructions of biological soft tissue are presented using the new grating-based setup. Furthermore, the power of the method for analysing centimetre-sized unstained weakly absorbing samples in fluid environment is discussed.

5.2. Imaging of welded materials

5.2.1. Imaging laser-welded T-joints in absorption mode

Motivation

New advanced joining techniques like laser beam welding (LBW) and friction stir welding (FSW) have a high potential for light weight structures of automotive and aircraft industries [12]. Using LBW in fabrication of metallic airframe components could reduce fabrication cost and fuel consumption during the operation significantly due to the weight reduction compared to riveting (see Figure 5.1). Currently, only a limited number of fuselage parts of civil aircrafts are welded due to stringent damage tolerance requirements. In order to enhance the use of laser-welded parts in the fuselage of new generation aircrafts, such as the A380, there is the need for better understanding of the crack propagation in the vicinity of the weld joints. Additionally, there is the need to improve the understanding on the interaction between damage development and existing weld imperfections, such as porosity within the weld zone. It is known that like all fusion welding processes, LBW is prone to porosity development and hence the effect of porosity on the growing crack should be studied using modern analytical methods and tools.

¹F.S. Bayraktar and P.Staron and M. Kocak and A. Schreyer, *Residual Stress and Fatigue Crack Growth Analysis of Laser Welded T-Joints of Aerospace Al-Alloys*, Oral presentation at the PNAM Intermediate Meeting, 2007.

5. Applications

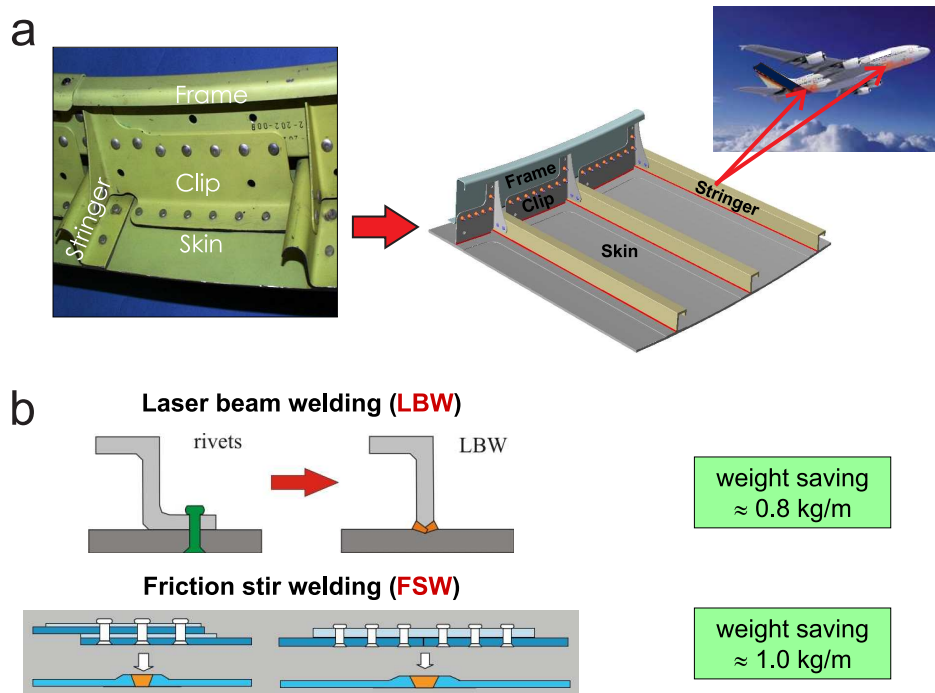


Figure 5.1.: Schematic comparing conventional riveting and welding in civil aircraft production. (a) Conventional riveted frame and welded frame with laser-welding as used in civil aircraft production. (b) Comparison between riveting and laser-beam welding (LBW) or friction-stir welding (FSW) concerning the weight reduction (Source of figures¹).

Two imaging methods are presented here as analytical methods to study the structure of welded materials: the synchrotron radiation based micro computed tomography in absorption mode ($SR\mu CT$) and the grating-based phase-contrast radiography (PCR). The $SR\mu CT$ combines the advantages of a non-destructive 3D visualisation with high spatial resolution and a very high density resolution due to the high-intensity monochromatic synchrotron radiation that is used for testing². With this technique also in-situ fatigue and fracture toughness tests on small scale specimens are possible studying for example the crack propagation within laser-welded aluminium and magnesium alloy joints. The second method - PCR - is a 2D imaging method, but it provides three different signals simultaneously, which otherwise only could be obtained from three different analysing methods (radiography, phase-contrast, and small-angle scattering). Using the synchrotron radiation a high spatial resolution at very short exposure times can be achieved. By using a 2D imaging method it was intended to match the real conditions of the quality assurance procedure during the welding process in industrial applications, where only x-ray radiography is used that is fast and non-destructive. But the conventional x-ray radiography suffers from low contrast in the single projections, such that the position and the size of the pores and precipitates inside the welded regions can hardly be defined. The problem can be solved by performing a whole tomography scan of the

²Imaging with monochromatic radiation avoids polychromatic artifacts, that are caused when lower photon energies were stronger absorbed than the higher. This effect leads to an energy shift to higher energies and reduces the dynamic range of the imaging system

specimens, where the reconstructions would show a high density and spatial resolution. As this is very time consuming (several hundreds of images are necessary for a whole tomography), the 2D PCR can close the gap between a fast measurement and a high detection rate of the inner structures by combining the different contrasts. An important advantage of this technique is that it can be easily applied during the welding process visualising in-situ the changes inside the welded material. For a 2D PCR only a small amount of additional images is needed compared to the conventional radiation (while one image in the conventional radiography in absorption mode is needed, at least four images in grating-based phase contrast is required).

Absorption-contrast tomography

Sample preparation All measurements were performed at the beamline W2 described in detail in Chapter 2. Figure 5.1(a) shows the structure of a partly welded airframe used in some parts of new civil aircrafts. In this study we concentrate on the laser-welded aluminum T-joints representing "clips", which connect the skin to the frame as shown in Figure 5.1(a).

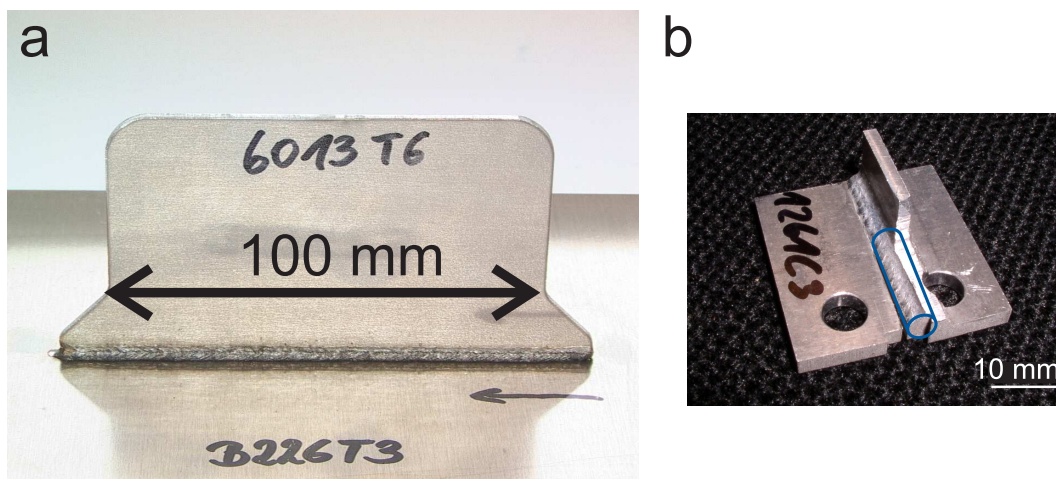


Figure 5.2.: (a) A 2 mm thick aluminum alloy 6013 T6 clip welded by laser to a 3 mm thick skin of aluminum alloy B226 T3. The length of the clip is about 100 mm and the skin area is 600 x 400 mm. Residual stress analysis was performed on such samples using synchrotron radiation and by putting cyclic load the stability of the welded region is tested under high load. (b) A miniaturized laser-welded clip (clip: AA6013 T6; skin: AA2139 T3 (same as B226 T3)) for a microtomography study using synchrotron radiation. A small cut was introduced as a notch near the weld and the two holes were used for the testing machine to put cyclic load on the sample to propagate the crack. The marker shows the welded region that was cut cylindrically (30 mm long and 6 mm diameter) for the absorption-contrast SR μ CT measurement.

The GKSS Research Center runs an Nd:YAG laser with a 400 μ m fiber, a focal length of 200 mm and a laser power of 3 kW. Helium is used as shielding gas during the welding process and the angle between the skin and the laser beam can be altered. However, some amount of

5. Applications

small pores (due to for example entrapment of oxygen) may occur within the molten metal. No artificial attempt was made to produce porous weld metal. By varying the welding speed and the welding angle the properties of the produced laser weld can be influenced. Also the porosity within the weld strongly depends on the process parameters as well as alloy composition.

Residual stresses inside the laser-welded aluminium alloy T-joints (sample shown in Figure 5.2(a)) were studied at GKSS before [5, 67]. The samples consisted of a 2 mm thick aluminum alloy AA6013 T6 clip welded by laser to a 3 mm thick skin of aluminum alloy B226 T3. The length of the clip was about 100 mm and the skin area was 600 x 400 mm. Such samples were produced using the Nd:YAG laser and a silicon wire (Si 4047) and residual stress analysis was performed by means of x-ray and neutron scattering techniques. Such specimens were used at GKSS to study crack propagation along the weld seam.

For the microtomography analysis the laser-welded T-joints had to be downsized (materials: clip AA6013 T6; skin AA2139 T3 (same as B226 T3)), since the spatial resolution of the tomogram depends on the sample size. The aluminium alloys used in the T-joints contain a small amount of copper, tin, titanium and iron and thus, a microtomographic measurement with high density resolution is a challenge. The absorption of the whole sample is quite high, so that a high x-ray energy would be required for the measurement (70 keV) to penetrate the sample. Because of the decreasing efficiency of the imaging setup³ and the contrast at higher energies, high density resolution imaging is very difficult to achieve. Therefore, a small sample (30 mm long and 6 mm diameter) was prepared by cutting the welded region cylindrically out of the T-joint as marked in Figure 5.2(b) and scanned using a photon energy of 40 keV.

Measurement The microtomography station at the high energy beamline W2 is designed for materials science applications using hard x-rays. The fixed-exit monochromator provides a highly intense monochromatic x-ray beam in the range of 20-200 keV. The possibility to use monochromatic radiation for imaging allows to choose the optimum energy for each object and to avoid unwanted effects such as beam hardening caused by polychromatic radiation. The tomography setup consists of a high precision rotation stage, which allows us to mount the sample hanging from above, and an x-ray detector. In the detector a fluorescent screen (CdWO₄ single crystal, 500 μ m thick) converts the x-rays into visible light that is magnified by a lens (Nikkor, focal length 50 mm or 35 mm) and detected by a CCD camera (KX2, Apogee Instruments, Inc., 14 bit @ 1.25 MHz).

For a complete tomographic scan 720 radiographic projections of the sample were taken in equidistant rotation steps of 0.25 degree in the angular range from 0° to 180°. Each 2 degrees the sample was moved out of the beam and an image is taken, which is used for flat field correction. The maximum field of view of the detector was 25 mm \times 8 mm and an energy of 40 keV was used. An effective pixel size of 6.83 μ m and a spatial resolution of 10.45 μ m were determined by means of a modulation transfer function for this measurement.

³The photon flux decreases with higher photon energies as the energy range of the wiggler W2 with the maximum flux is around the critical energy of 27 keV. A high flux is mandatory to achieve a high density resolution. In addition, the efficiency of the 500 μ m luminescent screen decreases with higher energies.

To reconstruct the 3D structure from the projections the filtered back projection algorithm for absorption contrast was used. The projections with the sample were normalized by the reference projections without the sample, so that the obtained projections represent the absorption of the sample at different angles. The reconstruction then provided volumetric information about the absorption of the sample in 3D. The reconstructed data was stored as a floating point volume and processed by VGStudio Max (Volume Graphics GmbH, Heidelberg, Germany) to a volume rendering dataset.

Results Figure 5.3 presents the result of the high resolution tomography measurement of the laser weld cut cylindrically out of the T-joint. The tomogram shows an excellent density resolution and all different aluminium alloys used in the weld could be clearly separated, even though the density difference between the aluminium alloy used in the clip ((3) top of the weld) and the alloy used in the skin ((1) bottom region of the weld) was below 5 % (alloy densities: (3) AA6013 2.7 g/cm³; (1): AA2139 2.8 g/cm³)⁴ and produced only a weak relative absorption contrast at 40 keV. Even the weld region itself could be separated from the base material. It is displayed as transparent to make the different types of pores visible (blue structures). This result demonstrates the advantage of using synchrotron radiation for imaging: As the optimum photon energy can be chosen for each material, it is possible to visualise highly absorbing samples almost free of artifacts with high density and spatial resolution in absorption mode. It is a very unique result, as it is very hard to achieve such a high density resolution using high x-ray energies.

5.2.2. Imaging laser-welded butt-joints in phase-contrast mode

Phase-contrast radiography

Sample preparation Butt-joints welded by the same laser-welding method described above were imaged using the phase-contrast radiography (PCR). Figure 5.4 shows the two specimens used for this study: (a) the magnesium alloy joint (2.5 mm thick; material AZ31, 3% aluminium, 1% zinc, density: 1.8 g/cm³) and (b) the aluminium alloy joint (2.8 mm thick; material: AA6156, 95-98% aluminium, 1% magnesium, 1% copper, density: 2.7 g/cm³). From both samples, small specimens were cut out in the marked region and glued to a sample holder, which was placed on the CT-rotation axis of the grating-based imaging setup introduced in Chapter 3. To simplify the measurement a small part of the sample was cut out from the welded region. However, also the whole joint could be put into the beam without destroying it.

As laser-beam welding melts the basic material in the region of the weld, not only the characteristics of the alloys are changed (strength and flexibility) but also precipitations of different compound materials present in the alloy can occur and porosity can be introduced by e.g. entrapment of oxygen. The welding process can be optimised by changing the alloy composition or welding parameters like laser-beam speed and incident angle. In industrial laser-beam welding the welds are checked directly after welding using x-ray radiography with

⁴data source: <http://www.matweb.com>

5. Applications

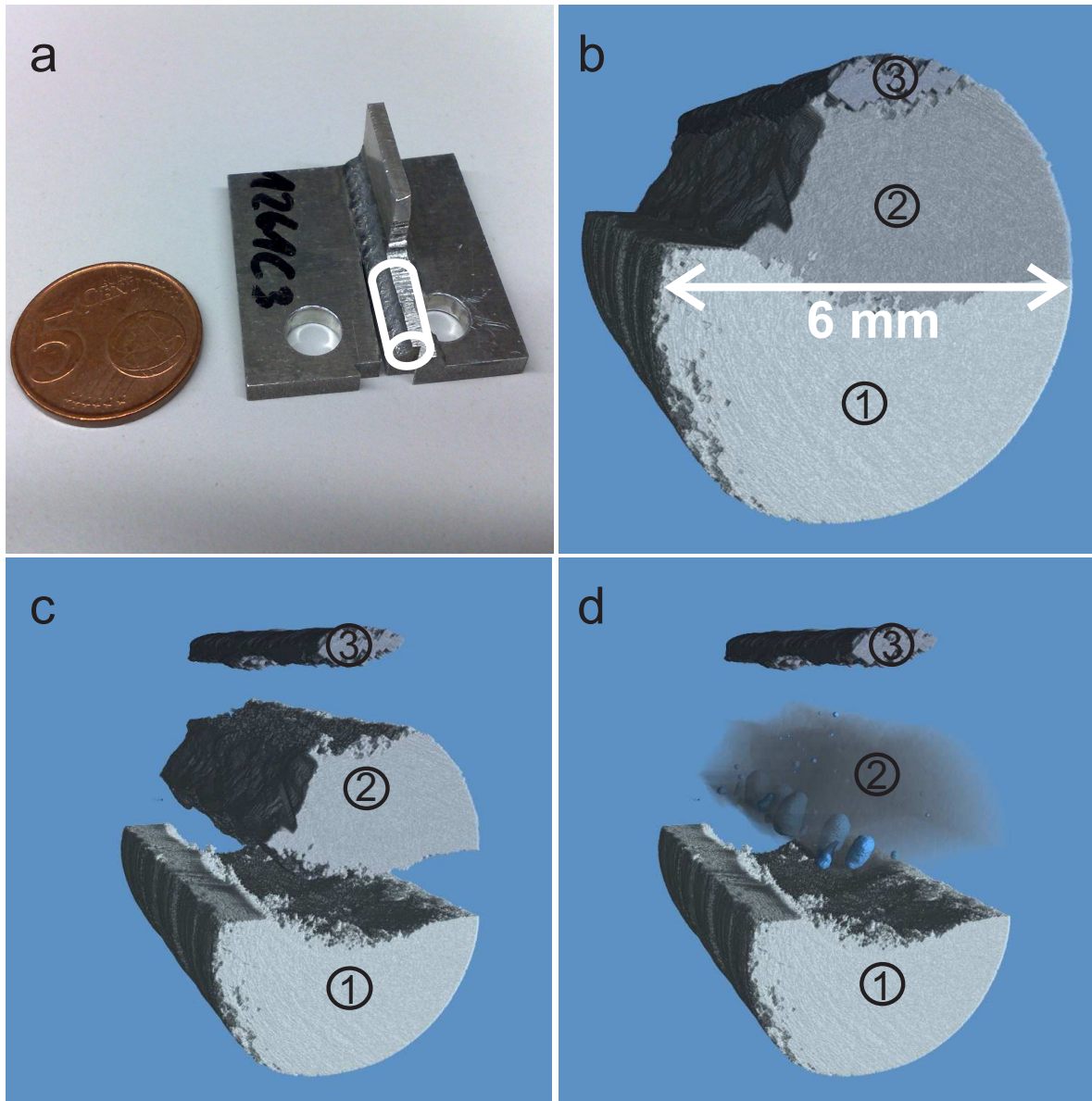


Figure 5.3.: Picture of the T-joint and the volumetric rendering of the tomogram of the cylindrically cut aluminum alloy laser weld. The tomography scan of the 6 mm weld was performed using 40 keV and the absorption mode setup. The different gray values represent the absorption of different alloys used in the weld ((1): AA2139 T3, (2) welded region containing pores, (3): AA6013 T6). The weld itself is shown as transparent to make the pores visible that are coloured blue (spatial resolution: $10.45 \mu\text{m}$, effective pixel size: $6.83 \mu\text{m}$).

an x-ray tube and a detector.

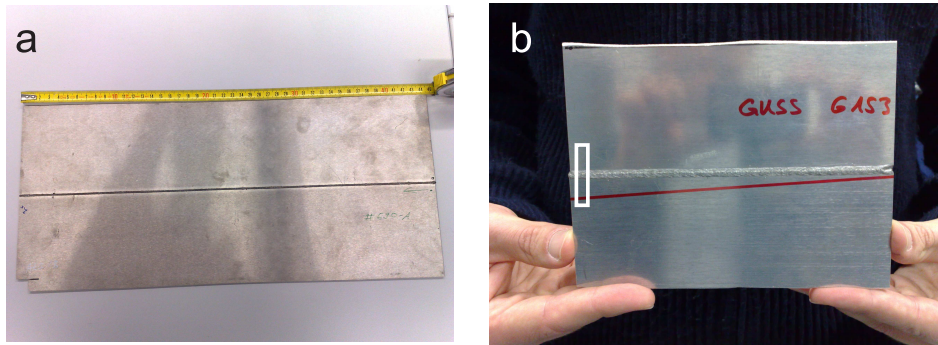


Figure 5.4.: Picture of laser-welded butt-joints imaged using grating-based phase-contrast radiography (PCR). (a) magnesium alloy joint (2.5 mm thick; material AZ31, 3% aluminium, 1% zinc, density: 1.8 g/cm^3) and (b) aluminium alloy joint (2.8 mm thick; material: AA6156, 95-98% aluminium, 1% magnesium, 1% copper, density: 2.7 g/cm^3). From both samples small specimens were cut out in the marked regions and glued to a sample holder.

Measurement For both specimens the projections were recorded using the grating interferometer in the 5th Talbot order at 30 keV. The beam-splitter grating G_1 #1 was used for the measurements (see Chapter 3 for more details). To obtain one projection a phase-stepping scan with 8 phase steps over two periods of the grating G_2 was performed with the specimen in the beam and without the specimen, to obtain flat field correction images (exposure time: 0.5 s per image). From the intensity changes during the phase-stepping scan three different contrast projections were calculated by means of a Fast Fourier Transform (FFT) as explained in Chapter 3 using Matlab.

Results and discussion Figure 5.5 shows the results of the PCR measurement of the magnesium-alloy (a)-(c) and aluminium-alloy (d)-(f) butt-joints. Figures 5.5(a) and (d) show the transmission pictures of both specimens similar to that, one would obtain using a conventional absorption-contrast mode. In the welded region marked in the Figure, only weak contrast of inner structure of the weld can be seen (here: porosity and precipitations), while the base material (bottom part of the specimens) absorbs homogeneously. Although the specimens were measured in air, this setup should produce enough contrast due to the large density difference of air and magnesium or aluminium ($\rho_{air} = 0.0012 \text{ g/cm}^3$ and $\rho_{Mg} = 1.74 \text{ g/cm}^3$, $\rho_{Al} = 2.7 \text{ g/cm}^3$). But in the projections one can hardly define the position and the size of the pores and precipitates inside the welded regions. The problem can be solved by performing a whole tomography scan of the specimens, rotating it over 180 degrees and recording projections from many different angles. The reconstructions would show a high density and spatial resolution, thus, the localisation of porosity and precipitates would be easily possible. But as already mentioned a whole tomography often is too time-consuming and destructive as the sample has to be downsized, since the spatial resolution depends on the total sample size. Thus it would not match the real conditions of the quality assurance procedure during the welding process in industrial applications.

Looking at the other two signals provided by the grating interferometer, one can clearly

5. Applications

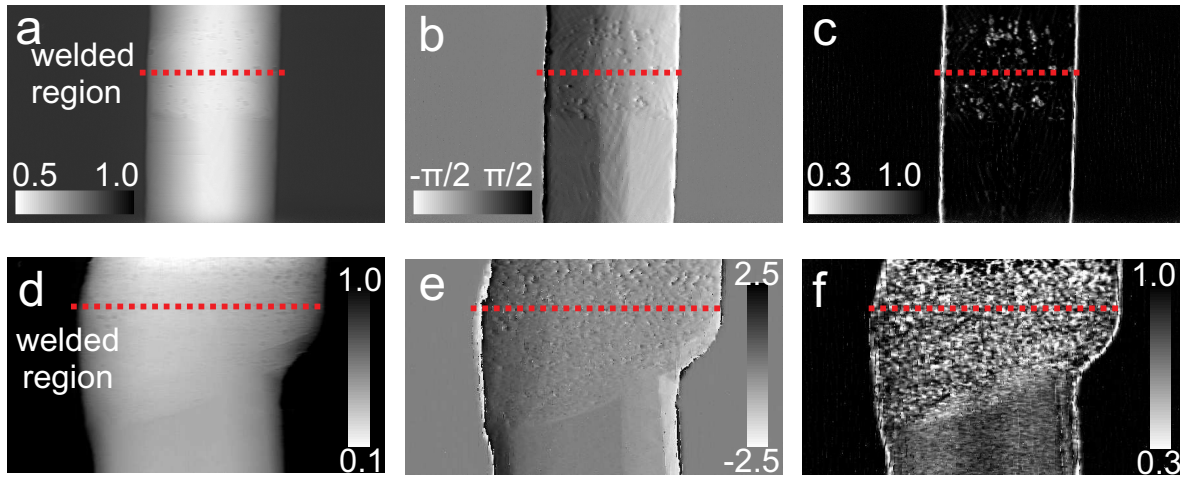


Figure 5.5.: (a)-(c) Projections of a magnesium-alloy laser weld (material: AZ31; 30 keV, 5th Talbot order, field of view: 4x6 mm²). (a) The transmission (b) the differential phase contrast and (c) the dark-field contrast of the same region of the sample. The dark-field and the differential phase-contrast signals show better contrast in the welded region, while the transmission shows only poor contrast for inner structures. (d)-(f) Projections of an aluminum-alloy laser weld (material: AA6156; 30 keV, 5th Talbot order, field of view: 4x6 mm²). (d) X-ray transmission, (e) the differential phase contrast, and (f) the dark-field contrast. The differential phase contrast and the dark-field signals increase in the welded region, while the transmission is almost the same.

distinguish between the welded region and the basic material (see Figure 5.5(b) and (e) for differential phase contrast and (c) and (f) for dark-field contrast. Both signals rise at each edge inside and outside the specimens, so the borders of the samples produce a very high signal in both contrasts. In the differential phase contrast 'phase-wrapping' can be seen at the edges of the sample. This effect occurs when the amount of phase-shift exceeds several times π due to the large difference between the complex refractive index decrements δ of the air and the material. Phase-wrapping would produce strong artifacts in tomographic reconstructions and should be removed by an adequate algorithm prior to reconstructions, but it is not important for our purpose, as we were only interested in radiographic projections. Nevertheless, using the differential phase contrast the welded region of both specimens can be clearly localised.

The dark-field signal clearly shows the changes in the welded regions of the specimens compared to the basic material. Since this signal is similar to the small-angle scattering signal, the structure of the material was changed by laser-beam welding in such a way, that small-angle scattering signal rises. As the interferometer is sensitive only to structures in the range of few μm , such structures must appear in the weld. The basic material of the magnesium sample seems not to produce a dark-field signal, thus, only the porosity inside the weld can be seen. In the aluminium specimen the basic material also produces dark-field signals, but it increases in the welded region, as precipitations appear after welding increasing the dark-field signal.

Conclusions

The results from the two approaches, the tomography in absorption mode (SR μ CT) and the radiography in phase-contrast mode (PCR), demonstrate the power of the methods to give unique insights into the inner structure of the materials and changes caused by welding processes. Especially the SR μ CT can be used to study the porosity inside the welds and can help to improve the welding processes by characterising the welds in 3D.

The special assets of the PCR are its ability to provide three different contrast simultaneously allowing to judge the quality of the weld from simple projections by combination of the information from the signals. Using the synchrotron radiation beamline W2 very short exposure times (due to high flux) and high spatial resolution at large field of view sizes compared to other synchrotron beamlines (now: 6 mm \times 30 mm; in future: 6 mm \times 60 mm) can be achieved in PCR projections. As a possible future task, the PCR at the beamline W2 can be expanded to imaging other welding processes like Friction Stir Welding (FSW). It can even be used for in-situ imaging to visualise the changes in the welded region on the fly in combination with the in-situ welding machine FlexiStir [32, 89], as a 2D PCR can be performed in several seconds.

This approach can also be adopted to the standard quality assurance procedure for welding as known from industrial applications by equipping the x-ray tube and the detector with a propiate grating interferometer. It would loose the high flux, the spatial resolution, and the ability to adjust the x-ray energy to the analysed material, but it profit from the high availability of the x-ray tubes for a high throughput.

An analysis of those welds in three dimensions using phase-contrast tomography is not shown here, as a reconstruction of the images shows in all signals many strong artifacts due to strong phase wrapping at the edges of the specimen. Such phase jumps could be avoided by scanning the sample in an environment with similar refractive index like the one of the metal joints, for example some kind of oil. But such analysis would take too long to be used as a standard quality assurance method and it would be far away from realistic conditions, since the metal joints are hardly put into oils or other fluid environment.

5.3. Phase-contrast tomography of biological samples

5.3.1. Introduction

Imaging weakly absorbing materials with x-rays in absorption mode is possible using lower photon energies (in the range of 7-10 keV) and sample preparation techniques like staining, freeze-drying, and embedding into resin. Excellent results were reported using the micro tomography setup in absorption mode operated by GKSS at the DESY beamline BW2 using low energies on ceacilians [56], sponges [43, 75], and on insects in the report [33].

5. Applications

The complicated sample preparation is mandatory to stabilize the sample for a micro tomography scan, which can take up to two hours. By staining the samples or parts of it the contrast in the tomogram is increased. All these preparation methods are very time consuming and strongly change the soft tissue e.g. by freeze-drying. Thus, many unique and valuable specimens cannot be analysed, as the preparation would destroy them (for example very old ceacilian species from museums). The same problem occurs when analysing human or animal soft tissue. Such specimens need to be measured in fluid environment, but in this case the absorption of the fluid (and also of the specimen itself, when it is not cut down to a few millimetres) would absorb too strongly at lower energies. The grating-based phase-contrast imaging method installed at the beamline W2 can close this gap, as it works at higher photon energies (in the range between 22-30 keV) and allows for measuring samples of several centimetres in fluid environment.

As an example phase-contrast tomographical reconstructions of mouse heart and brain are presented in this Section. Whole organs (≈ 10 mm diameter, specimens from TU München) embedded in formalin were scanned in a water bath using the new grating-based setup at the beamline W2 demonstrating the achievable contrast in the soft tissue.

5.3.2. Tomography of mouse heart and brain

Sample preparation and measurement

Both specimens were embedded in a formalin solution (4 % formalin as used in medicine) in a polyethylene Eppendorf tube of 12 mm outer diameter. The formalin solution was degassed for two days under a low-pressure cap to avoid gas bubble formation produced by radiation damage during the scan. The Eppendorf tube with the specimen was glued to a sample holder and mounted on the CT-rotation axis hanging from above into a 25 mm thick water container filled with demineralised water. The water serves as background for the measurement to match the complex refractive index of the specimen to that of the background to avoid 'phase-wrapping' at the edges of the sample container in the phase-contrast signal.

The measurements were carried out using the grating interferometer at the beamline W2 (see Section 3 for more details about the setup). For the tomography scan 451 projections over 360 degrees were recorded with 8 phase-steps over two periods of the grating G_2 for each projection. The exposure time was in the range of 5 seconds per image, changing during the scan to correct for the decreasing ring current of DORIS. The images were taken with a binning factor of 2. After every projection a reference projection was recorded by moving the sample vertically out of the water tank. The reference projections were used to correct for beam instabilities. The effective pixel size was determined by an automated focussing procedure to be $6.3 \mu\text{m}$, the spatial resolution is estimated to $\approx 15\text{-}20 \mu\text{m}$ (limited by the source size and the sample-to-detector distance).

The reconstruction was performed using the filtered back projection algorithm as described in Chapter 3 implemented in Matlab. The reconstructed slices were stored as floating point data and windowed to the given gray values before image export. To obtain absolute values of measured data, the reconstructed values had to be corrected for the reduced sensitivity of the grating interferometer as described in Chapter 4, the recorded phase projections were

5.3. Phase-contrast tomography of biological samples

renormalized by multiplication with $(r_1/l)^{-1} = [(3.0 \text{ m} - 0.055 \text{ m})/(3.0 \text{ m})]^{-1} = 1.01868$ prior to reconstruction.

Results and conclusions

In the Figures 5.6 and 5.7 the tomographic reconstructions of the mouse heart and brain are shown. The parts (a) of both figures show the attenuation coefficient μ , (b) the real part of the complex refractive index decrement δ measured relatively to water. Whereas the attenuation (a) shows almost no structures, the phase-contrast provides a detailed information about the inner structure of the samples. In the heart tissue as well as in the brain tissue, different structures can be distinguished. The reconstructions of the dark-field signal are not shown here, as similarly to the absorption contrast it do not show any information about the sample.

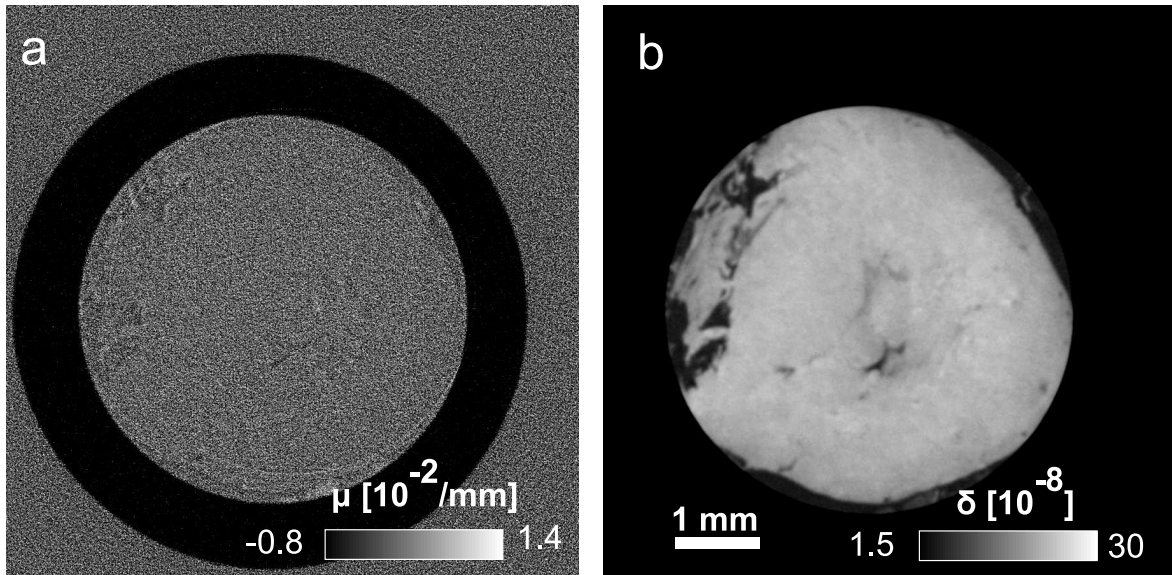


Figure 5.6.: Tomographic reconstructions of a mouse heart. (a) Attenuation coefficient μ , (b) real part of the complex refractive index decrement δ , measured in water bath at 7th Talbot order and 22 keV, binning factor 2, spatial resolution $\approx 15\text{-}20 \mu\text{m}$.

The results of the phase-contrast tomography scan of a mouse heart and brain demonstrated high sensitivity to phase shifts providing good contrast of weakly absorbing materials in fluid environment. No information of these specimens could be gained from the absorption and the dark-field contrasts.

Using the grating-based imaging method soft tissue can be measured without complicated and time-consuming sample preparation procedures. Even imaging of unique and very valuable samples can be done by this method without destroying or changing its structure. In future tasks, soft tissue can be analysed in sodium-chloride solution (NaCl) to avoid changes through the formalin or alcohol in the tissue.

5. Applications

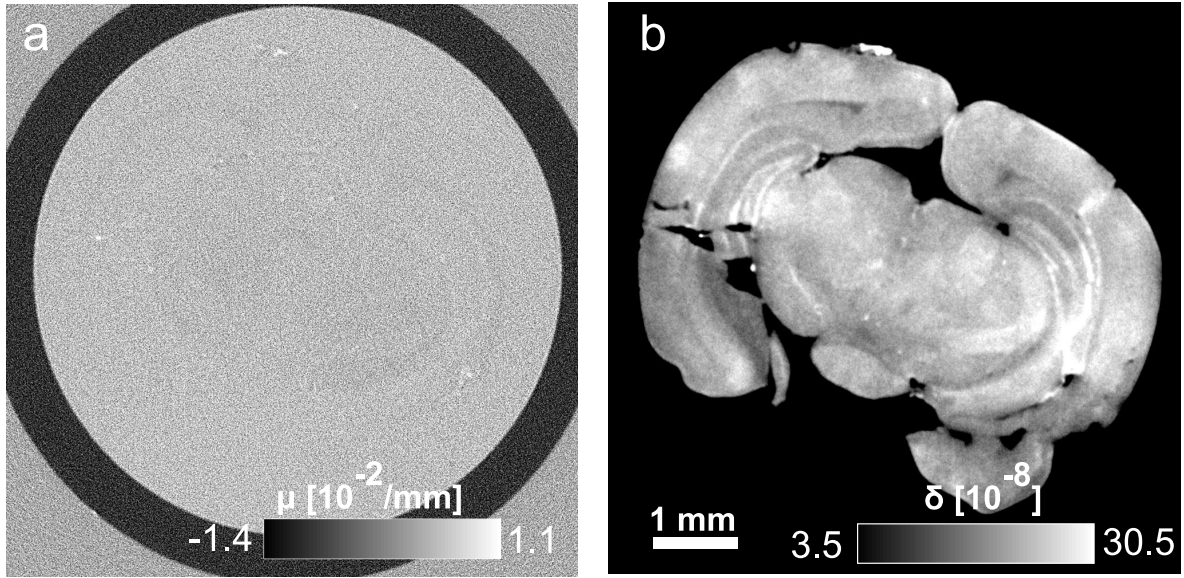


Figure 5.7.: Tomographic reconstructions of a mouse brain. (a) Attenuation coefficient μ , (b) real part of the complex refractive index decrement δ , measured in water bath at 7th Talbot order and 22 keV, binning factor 2, spatial resolution $\approx 15\text{-}20 \mu\text{m}$.

These measurements clearly demonstrate the power of the new grating-based setup to image centimetre-sized soft-tissue samples in fluid environment. It benefits from the ability to choose the optimum photon energy for each specimen (from the range of 22-30 keV) and from the high photon flux, keeping the exposure times short. In addition, it makes quantitative measurements easier, as the reconstructions do not suffer from polychromatic artifacts.

Imaging structures inside the biological soft tissue like human or animal brain or heart tissue is hardly possible using the conventional absorption contrast. Fixation like the freeze drying or the contrast enhancement with different staining methods change the morphological and chemical structure of this tissue. The future aim should be to image such tissues in its natural fluid environment. When doing so, no conventional imaging in absorption mode can be used, as the lower energies, which would provide acceptable contrast for the tissue, are completely absorbed by the sample and the fluid around it.

For the first time, biological soft tissue of several centimetres diameter can be analysed at the beamline W2 without complicated staining or drying procedures with very high contrast using the grating-based setup. The achievable resolution of about $40 \mu\text{m}$ for objects of about 30 mm in diameter is much higher than what can be achieved with methods like Magnetic Resonance Tomography (MRT) showing comparable contrast for soft tissue but a much worse spatial resolution (in the range of several hundreds of μm).

5.4. Summary

In this Chapter the results of selected applications of imaging laser-beam welded materials and biological soft tissue were presented, using the grating-based setup installed at the beam-

line W2. As example for the potential of the micro tomography setup in absorption mode a tomographic reconstruction of an aluminium-alloy laser weld was shown, demonstrating high density and spatial resolution in imaging of highly absorbing materials. The shown density resolution could only be achieved using monochromatic synchrotron radiation with high flux and would not be possible at a conventional x-ray tube setup. This mode of tomography can be used to improve the understanding of damage processes inside the welds, helping establishing the laser-beam welding as a joining technique for example in civil aircraft production.

The phase-contrast radiography (PCR) now available at the beamline W2 using the newly installed grating interferometer is shown to be sufficient for fast structure analysis of both, welded magnesium and aluminium alloys with high spatial resolution. It provided unique information with only one projection and hence, allowed localising porosity and precipitates inside the welded region from radiographic projections of laser-welded butt-joints by combination of the three signals gained simultaneously. The method benefits from the ability to adjust the x-ray energy to the analysed material that is only possible using monochromatic synchrotron radiation. This method can easily be extended to in-situ analysis of welding processes (for example FlexiStir).

The phase-contrast tomography of animal soft tissue (mouse heart and brain) using the grating interferometer showed a high sensitivity to phase-shifts. It provided detailed information in phase-contrast signal, where as no contrast could be achieved with other signals. The results demonstrate the power of the method to facilitate the imaging of soft tissue, making sample drying and embedding in resin unnecessary.

6. Summary and outlook

A three-grating interferometer technique was installed at a low-coherence wiggler beamline source at the 2nd generation synchrotron storage ring DORIS at DESY. The x-ray grating interferometer was designed and installed at the materials science wiggler beamline W2 during this work. It allows for phase-contrast imaging using monochromatic radiation with high flux and a sufficient large field of view for analysing centimetre sized objects. The possibility to choose the optimum photon energy from a range between 22 and 30 keV and the ability to image specimens with three different signals obtained simultaneously makes the newly available imaging method a unique tool in the field of materials science.

The influence of the large, distant wiggler source on the performance of the grating interferometer was analysed and found to be negligible. The presence of a virtual source in the plane of the source gold grating used to increase the transverse coherence of the x-ray beam has been shown. Thus, in terms of the Talbot self-imaging effect the setup at the beamline W2 was found to be comparable to a setup at a conventional non-coherent x-ray tube. A simple approach to reliably calculate the spatial resolution in the differential-phase and in the absorption contrast is presented and successfully demonstrated by calculating the Modulation Transfer Function (MTF) of a sharp edge produced in both signals by taking projections of a silicon cuboid in different orientations. The spatial resolution of about 40 μ could be demonstrated for objects of 30 mm in diameter that is not as good as at highly brilliant third generation sources (about 5 μ m for objects of few millimetres), but much higher than what can be achieved with MRT with comparable contrast for soft tissue (about 200 μ m for an object size of 100 μ m).

The results of a tomographic measurement of a fluid phantom are presented, which were obtained at two different photon energies (22 keV, 7th Talbot order; 30 keV, 5th Talbot order) with the synchrotron setup. The results show that the technique provides reliable quantitative information about the distribution of the refractive index decrement δ and the attenuation coefficient μ . Furthermore, the contrast of different fluids measured at different photon energies has been used to quantify the performance of the setup at both energies. The contrast-to-noise ratios (CNRs) were used to characterise the effectiveness of the synchrotron setup helping to choose the optimum parameters for further investigations.

A similar tomography measurement of a fluid phantom was obtained during a research stay at the Laboratory for Micro- and Nanotechnology at the Paul Scherrer Institut in Switzerland, using the grating interferometer setup with a polychromatic x-ray tube. The measured attenuation coefficients μ and the refractive index decrements δ of the liquids agree well with the calculated theoretical values. The visibility of the interference pattern at the tube setup was significantly inferior to that of the synchrotron setup, and the exposure times were much higher due to the low flux of the tube source. Nevertheless, the accuracy of the results despite using polychromatic illumination with low flux combined with the high availability of x-ray

6. Summary and outlook

tube sources for small laboratories makes this method very interesting for a large field of applications.

Selected applications of imaging laser-beam welded materials and biological soft tissue, using the grating-based setup installed at the beamline W2 were presented. The strength of microtomography in conventional absorption mode was shown for a tomographic reconstruction of an aluminium-alloy laser weld demonstrating high density and spatial resolution in imaging of highly absorbing materials. The density resolution demonstrated could only be achieved using monochromatic synchrotron radiation with high flux and would not be possible at a conventional x-ray tube setup. This mode of tomography can be used to improve the understanding of damage processes inside the welds, helping to establish the laser-beam welding as a joining technique for example in civil aircraft production.

The newly installed grating interferometer provides the possibility of phase-contrast radiography at the beamline W2. This imaging method was shown to be sufficient for fast structure analysis of both welded magnesium and aluminium alloys with high spatial resolution. It provided unique information in a single projection, and allowed porosity and precipitates inside the welded region of laser-welded butt-joints to be localised by using a combination of the three signals gained simultaneously. This method can easily be extended to the in-situ analysis of welding processes (e.g. FlexiStir).

The phase-contrast tomography of animal soft tissue (mouse heart and brain) using the grating interferometer showed a high contrast to phase-shifts. It provided detailed information in the phase-contrast signal, whereas no contrast could be achieved with other signals. The results demonstrate the power of the method to facilitate the imaging of soft tissue, making additional sample preparation such as freeze-drying or embedding in resin as are needed for other imaging methods unnecessary.

In conclusion, this work provides significant further advances in x-ray imaging methods for a wide field of applications ranging from materials science to biomaterials.

A. Huygens-Fresnel principle and Talbot images

This Chapter deals with the derivation of the discrete Talbot image distances d_T from the *Fresnel-Kirchhoff* equation from Equation 3.36 using a wavefield propagation as described in Section 3.3.1 with the propagator kernel $h_z(x, y)$ from Equation 3.37. It will be shown that the only information needed about the wave front is its periodicity. The derivation is adopted from the book by Goodman [35].

A periodically modulated wavefront can be described by a transmission function of e.g. a sinusoidal amplitude grating as

$$t_A(\xi, \eta) = \frac{1}{2} [1 + m \cos(2\pi\xi/p)] , \quad (\text{A.1})$$

with period p and the grating lines being parallel to the η axis. As we know from Section 3.3.1 the propagation of the wave front can be calculated in Fourier space as a multiplication of the Fourier transform of the incident wave front $t_A(\xi, \eta)$ with the Fourier transform of the propagation kernel $h_z(x, y)$

$$H_z(f_x, f_y) = \mathcal{F}(h_z(x, y)) = e^{ikz} e^{\frac{i\pi\lambda z}{(f_x^2 + f_y^2)}} , \quad (\text{A.2})$$

where the constant term e^{ikz} will be omitted. The Fourier transform of a periodic function is discrete with the following spatial frequency spectrum

$$\mathcal{F}(t_A(\xi, \eta)) = \frac{1}{2}\delta(f_x, f_y) + \frac{m}{4}\delta\left(f_x - \frac{1}{p}, f_y\right) + \frac{m}{4}\delta\left(f_x + \frac{1}{p}, f_y\right) . \quad (\text{A.3})$$

The discrete nature of the transmission function has also an influence on the propagator kernel $H_z(f_x, f_y)$. It has value unity at the origin and when evaluated at the frequencies $(f_x, f_y) = (\pm 1/p, 0)$ it yields

$$H\left(\pm \frac{1}{p}, 0\right) = \exp\left(-i \frac{\pi\lambda z}{p^2}\right) . \quad (\text{A.4})$$

The propagation of a distance z is now performed as a multiplication of Equation A.3 and Equation A.4 in Fourier space

$$\mathcal{F}(U(x, y)) = \frac{1}{2}\delta(f_x, f_y) + \frac{m}{4}\exp\left(-i \frac{\pi\lambda z}{p^2}\right)\delta\left(f_x - \frac{1}{p}, f_y\right) + \frac{m}{4}\exp\left(-i \frac{\pi\lambda z}{p^2}\right)\delta\left(f_x + \frac{1}{p}, f_y\right) . \quad (\text{A.5})$$

The field at distance y from the grating is given by an inverse Fourier transform as

$$U(x, y) = \frac{1}{2} + \frac{m}{4}\exp\left(-i \frac{\pi\lambda z}{p^2}\right)\exp\left(i \frac{2\pi x}{p}\right) + \frac{m}{4}\exp\left(-i \frac{\pi\lambda z}{p^2}\right)\exp\left(-i \frac{2\pi x}{p}\right) , \quad (\text{A.6})$$

A. Huygens-Fresnel principle and Talbot images

which can be simplified to

$$U(x, y) = \frac{1}{2} \left[1 + m \exp(-i \frac{\pi \lambda z}{p^2}) \cos(\frac{2\pi x}{p}) \right] . \quad (\text{A.7})$$

The intensity distribution is then given by

$$|U(x, y)|^2 = I(x, y) = \frac{1}{4} \left[1 + 2m \cos(\frac{\pi \lambda z}{p^2}) \cos(\frac{2\pi x}{p}) + m^2 \cos^2(\frac{2\pi x}{p}) \right] . \quad (\text{A.8})$$

Now we should consider at least one interesting interpretation of the result. Suppose that the distance z downstream the grating satisfies

$$\frac{\pi \lambda z}{p^2} = 2n\pi \quad \text{or} \quad z = \frac{2np^2}{\lambda} , \quad (\text{A.9})$$

with n being an integer. Then the intensity downstream the grating will be described by

$$I(x, y) = \frac{1}{4} \left[1 + m \cos(\frac{2\pi x}{p}) \right]^2 \quad (\text{A.10})$$

that exactly reproduces the intensity distribution produced by the absorption grating. It is a perfect image of the intensity modulated by the grating and is called Talbot self image. These discrete Talbot distances z from Equation A.9 correspond to that introduced in Chapter 3 (see Equation 3.1). Please note that the only information used for the calculation of the self image positions is the periodicity and the free-space propagation of a wave front.

B. Alignment procedure

In this chapter the alignment procedure using the newly installed grating-based interferometer at the beamline W2 is explained. The additional steps necessary for grating-based imaging are based on the setting up procedure for the apparatus for conventional absorption-contrast imaging that is explained in detail for our setup in the work by T. Donath [28, Appendix D].

When the camera optics is focussed using the automated focussing procedure calculating an MTF function of a sharp edge using the standard procedure at the beamline W2, the alignment of the grating interferometer needs to be performed. For the alignment of the three gratings a laser pointer can be used that should be adjustable in all directions x, y , and z . First the laser pointer mounted on a holder that allows a stable and reproducible adjustment, it has to be aligned parallel to the x-ray beam. By putting two absorbing structures (e.g. lead needles) in a proper distance to each other (several meters) into the x-ray beam and by overlapping them in the transmission picture taken with the camera one can determine the approximate x-ray beam direction. Now aligning the beam from the laser pointer along these two structures it is assured that the laser beam is parallel to the x-ray beam.

The intergrating distances are checked to be correct before the gratings were installed. The movement along the beam direction for all three gratings is motorized and can be adjusted for each grating independently and additionally for the gratings G_1 and G_2 as a set. Wrong distances between the gratings lead to vertical moiré fringes due to the mismatched effective grating periods.

The gratings are mounted to their holders beginning with the grating G_2 . A diffraction pattern from the laser-pointer beam produced by the grating can be observed. By rotating and tilting the grating the diffraction pattern can be oriented horizontally and the zeroth diffraction order is placed to match the incident laser beam. Then the other two gratings are mounted and adjusted using the same procedure as for the G_2 , allowing for aligning the interferometer using visible light. Only small changes of the grating rotation are required after such alignment. Usually, the grating G_2 is rotated in steps of 0.01 degrees for fine-tuning. When the gratings were rotated against each other, horizontal moiré fringes can be observed B.1 (a). The G_2 is rotated until only the vertical fringe component can be seen, then the alignment is finished and the measurement can start. The vertical fringes in Figure B.1 (b) are due to a slight mismatch of the three grating periods and could be removed by tilting the gratings along the axis parallel to the grating stages. This would reduce the period of the rotated grating.

B. Alignment procedure

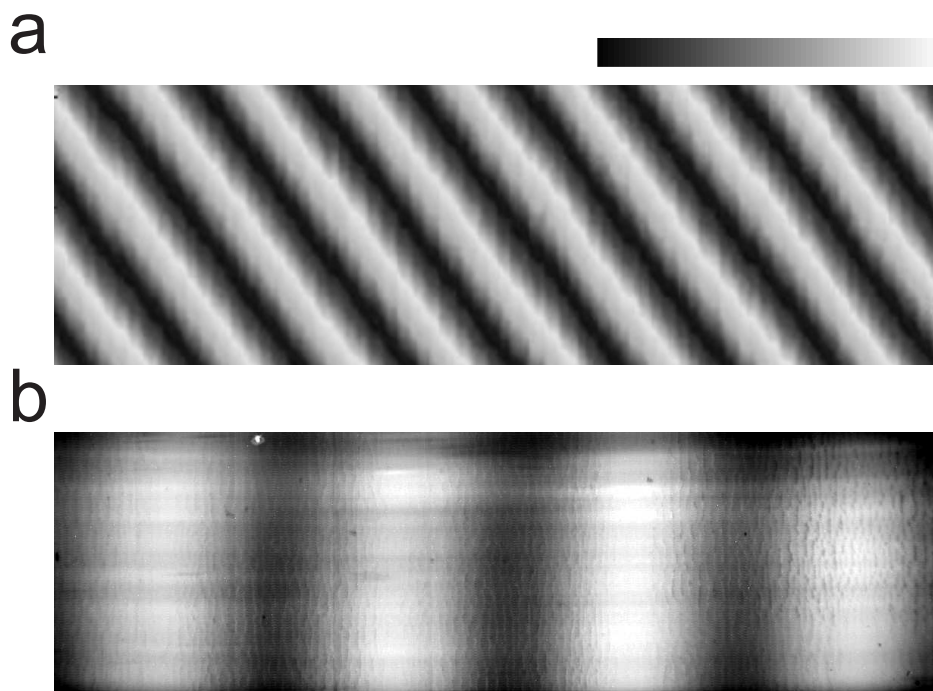


Figure B.1.: Image of the moiré fringes before (a) and after (b) the alignment procedure. The field of view is 30 (horizontal) \times (vertical) 5 mm and the gray values scale from black to white from 10 to 55×10^3 counts.

C. Grating production

The grating interferometer designed during this work consists of three gratings, the source gold grating G_0 , the beam splitter silicon grating G_1 , and the analyser gold grating G_2 . The periods and the heights of the gratings, as well as the mechanism behind the grating interferometer are described in Chapter 3. Here, the grating production is explained involving fabrication processes like photolithography, anisotropic wet etching, and electroplating. The gratings G_0 and G_1 were produced by the Laboratory for Micro- and Nanotechnology (LMN) at PSI in Switzerland using fabrication processes described by C. David *et al.* [25]. The grating G_2 is fabricated by the Karlsruhe Institute of Technology (KIT). Due to different requirements to the grating performances for each of the three gratings a different fabrication process was chosen.

Fabrication of the source grating G_0

Typical periods of the source grating G_0 are on the order 15-150 μm depending on the geometry of the setup, that makes it easier to produce them. When placed directly in front of the source it needs only to cover the area of the source. In our case, the G_0 is placed 45 m downstream the wiggler source, where it has to cover the whole field of view size of maximum 7 mm \times 30 mm (height \times width). The main requirement on the source grating is the height of the gold structures that has to be high enough for corresponding x-ray energy for sufficient absorption. For x-ray energies in the range of 22-30 keV as used in this work a height of the gold structures of 40-45 μm is sufficient that corresponds to a transmission of only few percent.

Figure C.1 is kindly provided by C. David (PSI, Switzerland) and shows schematically the fabrication steps of the source grating G_0 . The same fabrication method as described by C. David *et al.* [25] for the production of the analyser grating G_2 was used for the source grating production. A silicon grating with a period of 22.3 μm and a duty cycle¹ of 0.5 on the one half of the wafer and 0.7 on the other half is used as substrate. The two different DCs of the source grating G_0 allow for choosing between higher flux and higher fringe visibility. The grating grooves were then filled with gold by electroplating. It is essential that the filling starts only at the bottom of the grooves to ensure a complete, uniform filling. For this purpose, a 200 nm thick sacrificial layer of aluminium is evaporated under a sloped angle with respect to the grating structures (see Figure C.1(a)-(c)). Then the plating base consisting of a 15 nm thick adhesive layer of chromium and a 50 nm thick layer of gold is evaporated onto the sample under normal incidence (Figure C.1(d)). By etching away the aluminium in phosphoric acid, the gold is removed from the ridges of the grating lines, whereas the plating base remains on the bottom of the grooves. The gold structures with heights of $\approx 50 \mu\text{m}$ are plated onto the sample from a cyanide based plating bath (Autronex CC-AF-B by Enthone

¹Duty cycle is the ratio between the widths of the stages and the grooves of a grating. The duty cycle can change without changing the period of the structure.

C. Grating production

Omi) using a current density of 3.5 mA/cm^2 (Figure C.1(e)-(f)). A picture and a scanning electron micrograph of the resulting structures are shown in Figure C.2. This procedure was successful for the fabrication of structures with aspect ratios² up to 12, i.e. , a groove of $1 \text{ }\mu\text{m}$ can be filled with gold up to $12 \text{ }\mu\text{m}$.

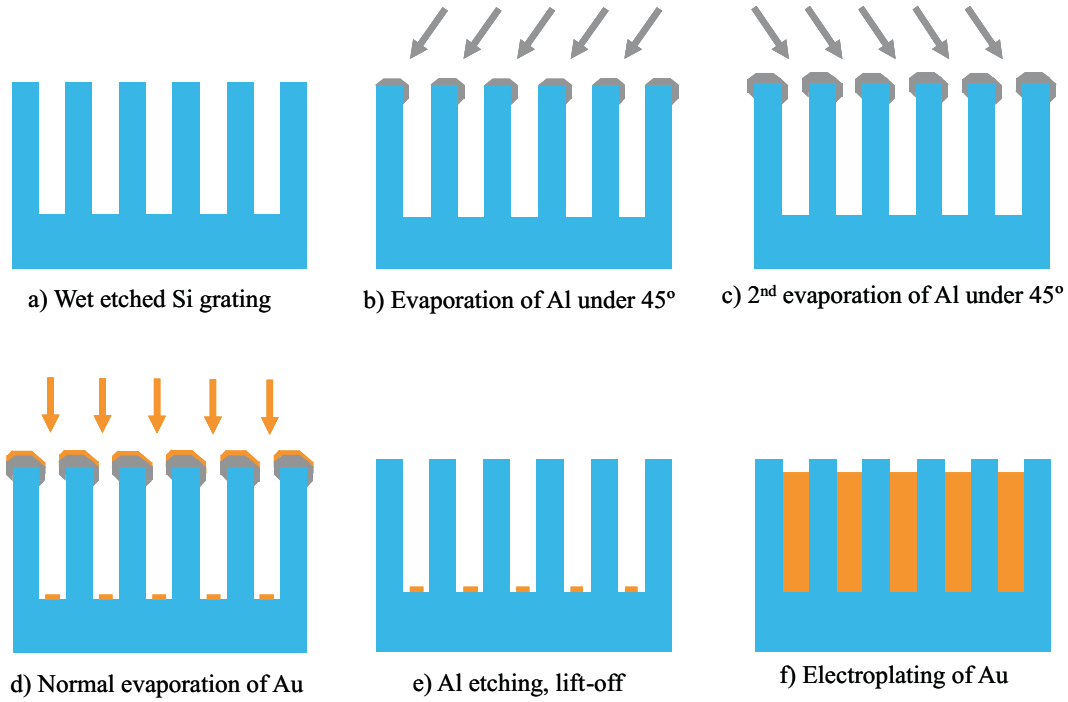


Figure C.1.: (a) The schematic of the fabrication process of the source gold grating G_0 consisting of six steps (a) wet etched silicon wafer, (b) evaporation of Al under 45° , (c) 2nd evaporation of 45° , (d) normal evaporation of Au, (e) Al etching, lift-off, and (f) electroplating of Au.

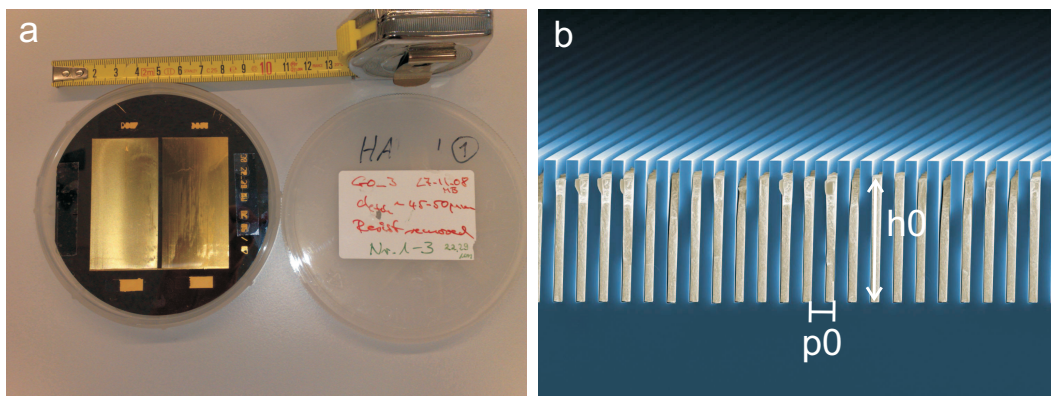


Figure C.2.: (a) Picture of the source gold grating G_0 produced on a silicon wafer (100 mm diameter). (b) A scanning electron micrograph of the grating G_0 showing the gold-filled silicon stages of the period $p_1 = 22.3 \text{ }\mu\text{m}$ and the height $h_1 \approx 50 \text{ }\mu\text{m}$.

²Aspect ratio is the ratio between the groove width and the structure height. The smaller the groove size the harder it is to achieve larger structure heights.

Fabrication of the beam-splitter grating G_1

The requirements for the beam splitter grating G_1 are more challenging than those for the source grating. It consists of low absorbing, phase shifting structures with a small period p_1 of $4.33 \mu\text{m}$. The best performance of the grating interferometer can be achieved when the structures have a duty cycle of 0.5, and when the height is chosen such that they introduce a phase shift of π at the design x-ray energy. Furthermore, the grating area has to cover the field of view of the imaging device, that is in the range of several centimetres. A $100 \text{ mm} < 110 >$ oriented and $280 \mu\text{m}$ thick silicon wafer with both sides polished is chosen as substrates. The wafer size limits the area of the grating to $64 \text{ mm} \times 64 \text{ mm}$.

The grating fabrication process is shown schematically in Figure C.3(a)-(d) also kindly provided by C. David (PSI, Switzerland). The grating structures are wet etched into the silicon substrates. First, the photo resist pattern is transferred into a thin oxide layer (Figure C.3(a)), which then after Reactive Ion Etching (RIE) serves as a mask for the anisotropic wet etching process in 20 % aqueous KOH solution (Figure C.3(b)-(c)). At $76 \text{ }^\circ\text{C}$ an etch rate of $1.68 \mu\text{m}/\text{min}$ is obtained in the $< 110 >$ direction. The etch rate along the $< 111 >$ directions is about 80 times slower, resulting in nearly perpendicular side walls of the structures that is confirmed by an inspection of the structures. The oxide masking layer has been removed in buffered oxide etch (BOE) before inspection (Figure C.3(d)). Figure C.4(a) shows picture of the beam splitter grating G_1 used at the new setup at the beamline W2 and with a structure height of $35 \mu\text{m}$, which corresponds to a phase shift of π for 27.3 keV x-ray energy. In Figure C.4(b) an SEM image of the grating is shown.

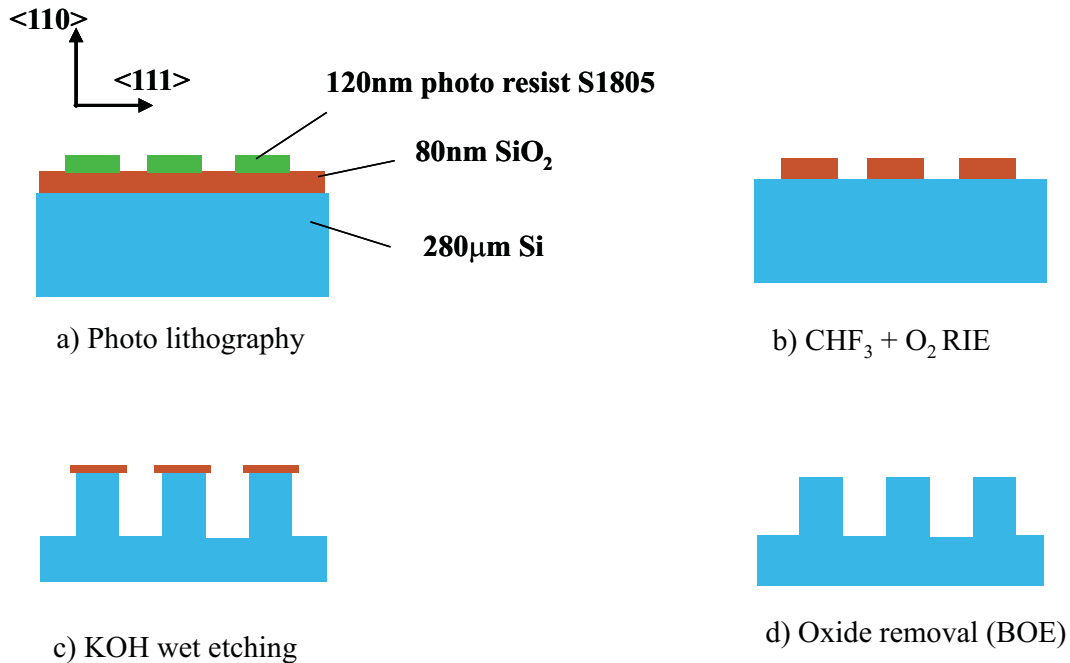


Figure C.3.: (a) The schematic of the fabrication process of the beam-splitter grating G_1 consisting of four steps (a) photo lithography, (b) reactive ion etching (RIE) with gases $\text{CHF}_3 + \text{O}_2$, (c) wet etching in 20 % aqueous KOH solution, and (d) removal of the oxide masking layer in buffered oxide etch (BOE).

C. Grating production

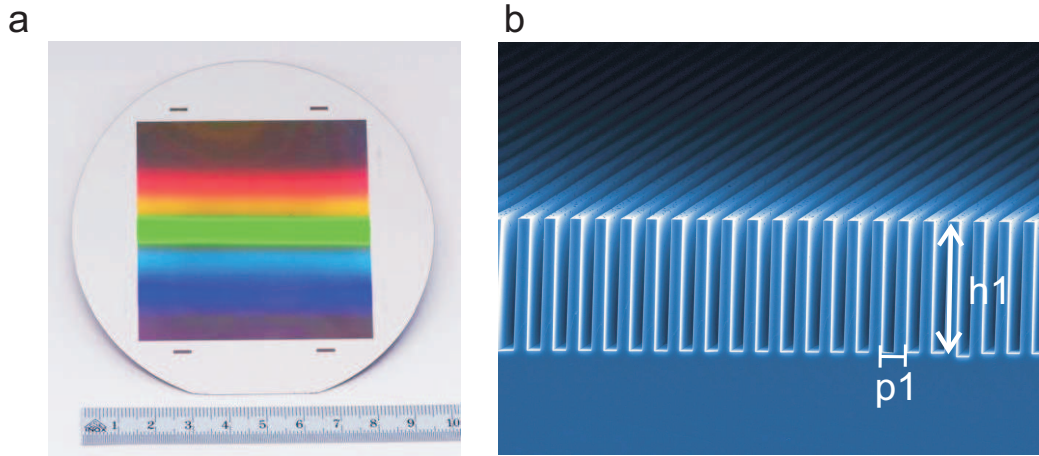


Figure C.4.: (a) Picture of the beam-splitter grating G_1 produced on a silicon wafer (100 mm diameter). b) An SEM picture of the grating G_1 showing the stages of the period $p_1 = 4.3 \mu\text{m}$ and the height h_1 , which are different for every photon energy.

Fabrication of the analyser gold grating G_2

The fabrication of the analyser grating G_2 is the most challenging of the whole setup. As the beam-splitter grating G_1 produces an interference pattern with double the period of itself, the grooves of $1.2 \mu\text{m}$ width have to be filled with sufficient height of gold. For the new setup at the beamline W2 the analyser gold grating with a period of $2.4 \mu\text{m}$ and a structure height of $30.8 \mu\text{m}$ was produced by KIT (Karlsruhe, Germany) using the LIGA process [87]. The description of the fabrication process is provided by E. Reznikova (KIT, Germany).

The amplitude gratings were made of electroplated Au within SU-8 polymer matrix with a period of $2.4 \mu\text{m}$ with aspect ratio of the grating lamellae up to 50. The quasi-solid SU-8(10) epoxy mono- and multi-layers were structured using X-ray lithographic exposure at the ANKA LITHO-1 station. For the x-ray lithography, a special x-ray mask was fabricated with a $4 \mu\text{m}$ thickness of Au absorber and a polyimide photo-electron internal filter, providing the proximity between the mask and the SU-8 layer close to zero. The sub-micron periodical lamellar structures of solid SU-8 ester net-polymer are formed during post-exposure baking process at lower temperature and gaseous pressure. The metal electroplating were done in a $55 \text{ }^\circ\text{C}$ heated solution with stirring and with pulsed current for gold deposition. Figure C.5(a) shows a picture of the analyser grating used in the setup at the beamline W2 with a period $p_2 = 2.4 \mu\text{m}$ and height $h_2 = 30.8 \mu\text{m}$, and (b) shows an SEM image of a similar gold grating kindly provided by E. Reznikova (KIT).

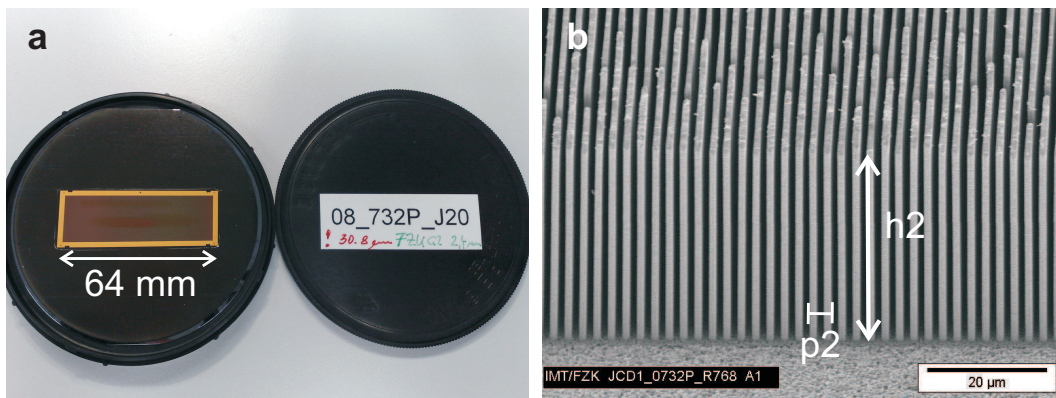


Figure C.5.: (a) Picture of the absorbing analyser grating G_2 produced on a silicon wafer (100 mm diameter), the grating is the golden structure in the middle. b) An SEM picture of the grating G_2 showing the gold structures of the period $p_2 = 2.4 \mu\text{m}$ and height $h_2 = 30.8 \mu\text{m}$.

D. Publications related to the work

This list presents a selection of publications coming out during the user support at the beamline W2 during this work. It contains not only the publications in peer-reviewed journals, but also in conference proceedings and the HASYLAB user reports. The publications with the author as coauthor including conference proceedings but without HASYLAB reports will be presented as a list in the end of the bibliography.

A study on the quantitiveness of the grating-based phase-contrast tomography using a conventional x-ray tube and a self-made fluid phantom, performed during the research stay at PSI, was published in [49]. The results of the corresponding measurement using the new grating setup at the synchrotron wiggler beamline W2 were published in the report [45].

Several SR μ CT studies in absorption mode on different materials were performed at the beamlines W2 and BW2 at DORIS during this work in collaboration with GKSS internal and external research groups. The publications in reviewed journals or several selected conference proceedings based on these studies will be listed here. The publications in HASYLAB annual reports¹ will be denoted as report.

The results of a region-of-interest SR μ CT study of crack visualisation in laser-welded aluminium alloy T-joints in absorption-contrast mode, performed at the beamline W2 during this work, were published in [47] and in reports [44, 48]. Another report [46] deals with the characterisation of titanium/aluminium friction joints with SR μ CT.

SR μ CT studies on biological specimens included a study of sponges published by J. U. Hammel *et al.* in [43], in the Proceedings of SPIE by M. Nickel *et al.* [75], and as reports in [41, 42]. Other studies made on insects were published as reports in [61, 62], and on amphibians published in [56] and in several reports [57, 60]. Human specimens have also been investigated. The results on determining the mineral distribution in flouritic teeth were published by F. Neues *et al.* [74], and on visualising interfaces inside the teeth by M. Dalstra *et al.* in [22]. Several reports treat the visualisation of human teeth in [23, 24] and bones in [15, 51, 52].

The results of a microtomography study in absorption mode on normal and pathological cranial sutures in children has been published recently in the Journal of Neurosurgery by J. Regelsberger *et al.* in [85] and as a report in [90]. The microtomography results in combination with ultra-small angle neutron scattering on hydroxyapatite microporous materials intended for use for bone regeneration has been published by C. Ritzoulis *et al.* in [88].

¹HASYLAB annual reports are available online at: http://hasylab.desy.de/annual_report/. [visited March, 2nd 2010]

Bibliography

- [1] DABAX library. <http://ftp.esrf.eu/pub/scisoft/xop2.3/DabaxFiles/>.
- [2] J. Als-Nielsen. *Elements of Modern x-ray Physics*. John Wiley & Sons, Chichester, 2008.
- [3] B. D. Arhatari, K. Hannah, E. Balaur, and A. G. Peele. Phase imaging using a polychromatic X-ray laboratory source. *Optics Express*, 16 (24):19950–19956, 2008.
- [4] H. H. Barrett and W. Swindell. *Radiological Imaging; The Theory of Image Formation, Detection, and Processing*. Academic Press Inc., 1981.
- [5] F. S. Bayraktar, P. Staron, M. Kocak, and A. Schreyer. Analysis of residual stress in laser-welded aerospace aluminium T-joints by neutron diffraction and finite element modeling. *Mater. Sci. Forum*, 571-572:355–360, 2008.
- [6] M. Bech. *X-ray imaging with a grating interferometer*. PhD thesis, Faculty of Science, University of Copenhagen, 2009.
- [7] F. Beckmann. *Untersuchung der Möglichkeiten der Mikrotomographie an konventionellen Röntgenquellen*. Diploma's thesis, Universität Dortmund, 1993.
- [8] F. Beckmann. *Entwicklung, Aufbau und Anwendung eines Verfahrens der Phasenkontrast-Mikrotomographie mit Röntgen-Synchrotronstrahlung*. PhD thesis, Universität Dortmund, 1998.
- [9] F. Beckmann, U. Bonse, F. Busch, and O. Günnewig. X-ray microtomography (μ CT) using phase contrast for the investigation of organic matter. *Journal of Computer Assisted Tomography*, 21(4):539–553, 1997.
- [10] F. Beckmann, T. Donath, J. Fischer, T. Dose, T. Lippmann, L. Lottermoser, R.V. Martins, and A. Schreyer. New developments for synchrotron-radiation-based microtomography at DESY. In *Proc. of SPIE; Developments in X-Ray Tomography V*, edited by Ulrich Bonse, 6318, 631810, 2006.
- [11] F. Beckmann, T. Dose, T. Lippmann, R. V. Martins, and A. Schreyer. The new materials science beamline HARWI-II at DESY. In *AIP Conference Proceedings, SRI 2006*, 2007.
- [12] F. Beckmann, R. Grupp, A. Haibel, M. Huppmann, M. Nöthe, A. Pyzalla, W. Reimers, A. Schreyer, and R. Zettler. In-situ synchrotron X-ray microtomography studies of microstructure and damage evolution in engineering materials. *Adv. Eng. Mater.*, 9(11):939–950, 2007.
- [13] F. Beckmann, K. Heise, B. Kölsch, U. Bonse, M. F. Rajewsky, M. Bartscher, and T. Biermann. Three-dimensional imaging of nerve tissue by X-ray phase-contrast microtomography. *Biophysical Journal*, 76:98102, 1999.

Bibliography

- [14] F. Beckmann, T. Lippmann, J. Metge, T. Dose, T. Donath, M. Tischer, K. D. Liss, and A. Schreyer. HARWI-II, the new high-energy beamline for materials science at HASYLAB/DESY. In *Synchrotron Radiation Instrumentation: Eighth International Conference*, edited by T. Warwick et al., 2004.
- [15] R. Bernhardt, C. Rentsch, B. Rentsch, A. Breier, A. Biewener, F. Beckmann, J. Herzen, D. Scharnweber, and H. Zwipp. SR μ CT analysis of bone regeneration based on biomimetically coated scaffolds in critical size defects of the sheep tibia. *HASYLAB annual report*, 2007.
- [16] U. Bonse, F. Busch, O. Günnewig, F. Beckmann, R. Pahl, G. Delling, M. Hahn, and W. Graeff. 3D computed X-ray tomography of human cancellous bone at 8 μ m. *Bone and Mineralogy*, 25:25–38, 1994.
- [17] U. Bonse and M. Hart. An X-ray interferometer. *Appl. Phys. Lett.*, 6:155–156, 1965.
- [18] O. Brunke, K. Brockdorf, S. Drews, B. Müller, T. Donath, J. Herzen, and F. Beckmann. Comparison between X-ray tube based and synchrotron radiation based μ CT. *Proceedings of SPIE*, 7078:70780U1–12, 2008.
- [19] F. Busch. *Auflösungsvermögen einer Mikrotomographie-Kamera für Röntgen-Synchrotronstrahlung*. PhD thesis, Universität Dortmund, 1994.
- [20] P. Cloetens, R. Barrett, J. Baruchel, J. Guigay, and M. Schlenker. Phase objects in synchrotron radiation hard x-ray imaging. *J. Phys. D: Appl. Phys.*, 29:133–146, 1996.
- [21] P. Cloetens, W. Ludwig, J. Baruchel, D. van Dyck, J. van Landuyt, J. P. Guigay, and M. Schlenker. Holotomography: Quantitative phase tomography with micrometer resolution using hard synchrotron radiation x rays. *Applied Physics Letters*, 75:2912–2914, 1999.
- [22] M. Dalstra, P. M. Cattaneo, J. Herzen, and F. Beckmann. Visualizing the root-PDL-bone interface using high-resolution microtomography. *Proceedings of SPIE*, 7078:70780L1–10, 2008.
- [23] M. Dalstra, P.M. Cattaneo, T. Donath, J. Herzen, and F. Beckmann. Microtomography of a human jaw segment at the newly rebuilt W2 beamline. *HASYLAB annual report*, 2006.
- [24] M. Dalstra, P.M. Cattaneo, J. Herzen, and F. Beckmann. Visualizing the root-PDL-bone interface - The key to understanding alveolar bone remodelling. *HASYLAB annual report*, 2007.
- [25] C. David, J. Bruder, T. Rohbeck, C. Grünzweig, C. Kottler, A. Diaz, O. Bunk, and F. Pfeiffer. Fabrication of diffraction gratings for hard X-ray phase contrast imaging. *Microelectronic Engineering*, 84:11721177, 2007.
- [26] T.J. Davis, T.E. Gureyev, D. Gao, A. W. Stevenson, and S.W. Wilkins. X-ray image contrast from a simple phase object. *Physical Review Letters*, 74(16):3173–3177, 1995.

- [27] F.A. Dilmanian, Z. Zhong, B. Ren, X.Y. Wu, L.D. Chapman, I. Orion, and W.C. Thomlinson. Computed tomography of x-ray index of refraction using the diffraction enhanced imaging method. *Physics in Medicine and Biology*, 45:933–946, 2000.
- [28] T. Donath. *Quantitative X-ray Microtomography with Synchrotron Radiation*. PhD thesis, Fachbereich Physik der Universität Hamburg, 2006.
- [29] M. Engelhardt, J. Baumann, M. Schuster, C. Kottler, F. Pfeiffer, O. Bunk, and C. David. High-resolution differential phase contrast imaging using a magnifying projection geometry with a microfocus x-ray source. *Applied Physics Letters*, 90:224101, 2007.
- [30] M. Engelhardt, C. Kottler, O. Bunk, C. David, C. Schroer, J. Baumann, M. Schuster, and F. Pfeiffer. The fractional Talbot effect in differential x-ray phase-contrast imaging for extended and polychromatic x-ray sources. *Journal of Microscopy*, 232 (1):145–157, 2008.
- [31] G. W. Faris and R. L. Bye. Three-dimensional beam-deflection optical tomography of a supersonic jet. *Applied Optics*, 27:5202–5212, 1988.
- [32] R. W. Fonda, J. F. Bingert, and K. J. Colligan. Development of grain structure during friction stir welding. *Scripta Materialia*, 51:243–248, 2004.
- [33] F. Friedrich, H.W. Pohl, F. Hünefeld, F. Beckmann, J. Herzen, and R.G. Beutel. SR μ CT-based study of external and internal structures of adults and larvae of Endopterygota (Hexapoda). *HASYLAB annual report*, 2007.
- [34] G. H. Glover. Compton scatter effects in CT reconstructions. *Medical Physics*, 9:860–867, 1982.
- [35] J. W. Goodman. *Introduction to Fourier Optics. Third Edition*. Viva Books Private Limited, 1996.
- [36] W.H.H. Gränicher. *Messung beendet - was nun?: Einführung und Nachschlagewerk für die Planung und Auswertung von Messungen*. vdf, Hochschul.-Verl. an der ETH Zürich; Teubner Verlag, 1996.
- [37] L. Grodzins. Critical absorption tomography of small samples - Proposed applications of synchrotron radiation to computerized tomography ii. *Nuclear Instruments and Methods*, 206:547–552, 1983.
- [38] L. Grodzins. Optimum energies for X-ray transmission tomography of small samples - Applications of synchrotron radiation to computerized tomography i. *Nuclear Instruments and Methods*, 206:541–545, 1983.
- [39] C. Grünzweig. *Neutron Grating Interferometry for Imaging Magnetic Structures in Bulk Ferromagnetic Materials*. PhD thesis, Eidgenössischen Technischen Hochschule Zürich, 2009.
- [40] T. E. Gureyev, C. Raven, A. Snigirev, I. Snigireva, and S. W. Wilkins. Hard X-ray quantitative non-interferometric phase-contrast microscopy. *Journal of Physics D*, 32:563567, 1999.

Bibliography

- [41] J. U. Hammel, J. Herzen, F. Beckmann, and M. Nickel. Morphogenesis during asexual bud formation and growth in the poriferan *Tethya wilhelma*. *HASYLAB annual report*, 2007.
- [42] J. U. Hammel, J. Herzen, F. Beckmann, and M. Nickel. High density resolution SR X-ray microtomography reveals spatiotemporal patterning of asexual reproduction in sponges. *HASYLAB annual report*, 2008.
- [43] J. U. Hammel, J. Herzen, F. Beckmann, and M. Nickel. Sponge budding is a spatiotemporal morphological patterning process: Insights from synchrotron radiation-based X-ray microtomography into the asexual reproduction of *Tethya wilhelma*. *Frontiers in Zoology*, 6:19, 2009.
- [44] J. Herzen, F. Beckmann, T. Donath, F. S. Bayraktar, S. Riekehr, M. Kocak, and A. Schreyer. Microtomography study of crack propagation within laser welded Al-alloy T-joints. *HASYLAB annual report*, 2007.
- [45] J. Herzen, F. Beckmann, T. Donath, M. Ogurreck, C. David, F. Pfeiffer, H. Burmester, R. Kirchhof, T. Dose, J. Mohr, E. Reznikova, A. Haibel, M. Mller, and A. Schreyer. Grating-based phase-contrast imaging at the beamline HARWI II. *HASYLAB annual report*, 2009.
- [46] J. Herzen, F. Beckmann, T. Donath, V. Ventzke, K.-H. Bohm, P. Merhof, W. Watzlaw, M. Kocak, and A. Schreyer. Characterization of Ti6Al4V/Al 7020-T6 friction welds using SR μ CT. *HASYLAB annual report*, 2007.
- [47] J. Herzen, F. Beckmann, S. Riekehr, F. S. Bayraktar, A. Haibel, P. Staron, T. Donath, S. Utcke, M. Kocak, and A. Schreyer. SR μ CT study of crack propagation within laser-welded aluminum-alloy T-joints. *Proceedings of SPIE*, 7078:70781V, 2008.
- [48] J. Herzen, F. Beckmann, S. Riekehr, F. S. Bayraktar, A. Haibel, P. Staron, M. Koak, and A. Schreyer. Crack visualization within laser-welded aluminium-alloy T-joints using SR μ CT. *HASYLAB annual report*, 2008.
- [49] J. Herzen, T. Donath, F. Pfeiffer, O. Bunk, C. Padeste, F. Beckmann, A. Schreyer, and C. David. Quantitative phase-contrast tomography of a liquid phantom using a conventional X-ray tube source. *Optics Express*, 17(12):10010–10018, 2009.
- [50] G. Illing, J. Heuer, B. Reime, M. Lohmann, R.H. Menk, L. Schildwächter, W.-R. Dix, and W. Graeff. Double beam bent Laue monochromator for coronary angiography. *Rev. Sci. Instrum.*, 66(2):1379–1381, 1995.
- [51] B.C. Johansson, J. Lindblad, H. Sarve, R. Bernhardt, F. Beckmann, J. Herzen, G. Borgefors, and D. Scharnweber. Improving the knowledge of integration of medical devices in bone; a comparison of 3D SR μ CT data to histomorphometrical data obtained on cut and ground sections. *HASYLAB annual report*, 2007.
- [52] C.B. Johansson, J. Lindblad, H. Sarve, R. Bernhardt, F. Beckmann, J. Herzen, G. Borgefors, and D. Scharnweber. Improving the knowledge of integration of medical devices in bone; a comparison of 3D SR μ CT data to histomorphometrical data obtained on cut and ground sections. *HASYLAB annual report*, 2006.

- [53] A. C. Kak and M. Slaney. *Principles of Computerized Tomography*. IEEE Press, New York, 1987.
- [54] P. Kirkpatrick and A.V. Baez. Formation of optical images by x-rays. *J. Opt. Soc. Am.*, 38:766–774, 1948.
- [55] J Kirz and C Jacobsen. The history and future of x-ray microscopy. *Journal of Physics: Conference Series*, 186(1):012001, 2009.
- [56] T. Kleinteich, Beckmann, J. Herzen, A. P. Summers, and A. Haas. Applying X-ray tomography in the field of vertebrate biology: form, function, and evolution of the skull of caecilians (Lissamphibia: Gymnophiona). *Proceedings of SPIE*, 7078:7078D1–10, 2008.
- [57] T. Kleinteich, F. Beckmann, J. Herzen, and A. Haas. SR μ CT in comparative anatomy and biomechanics of amphibian skulls. *HASYLAB annual report*, 2008.
- [58] C. Kottler, F. Pfeiffer, O. Bunk, C. Grünzweig, J. Bruder, R. Kaufmann, T. Tlustos, H. Walt, I. Briod, T. Weitkamp, and C. David. Phase contrast X-ray imaging of large samples using an incoherent laboratory source. *Physica Status Solidi A*, 204:2728–2733, 2007.
- [59] T. Koyama, H. Takano, Y. Tsusaka, and Y. Kagoshima. Tomographic quantitative phase measurement by hard X-ray micro-interferometer with 250 nm spatial resolution. *Spectrochimica Acta B*, 62:603–607, 2007.
- [60] S. Kuehnel, J. Vetter, T. Kleinteich, J. Herzen, F. Beckmann, and A. Kupfer. Synchrotron based high resolution X-ray computed microtomography of freeze dried amphibians and evolutionary reproductive morphology. *HASYLAB annual report*, 2008.
- [61] M. Kühbacher, B. Gruenewald, G. Falkenberg, E. Welter, J. Herzen, F. Beckmann, and A. Kyriakopoulos. Chemical and morphological characterisation of insect brains. *HASYLAB annual report*, 2007.
- [62] M. Kühbacher, B. Grünewald, G. Falkenberg, T. Donath, J. Herzen, F. Beckmann, and A. Kyriakopoulos. Neuroimaging with synchrotron-based methods. *HASYLAB annual report*, 2006.
- [63] E. Lau. Beugungserscheinungen an Doppellrastern. *Annalen der Physik*, 6:417, 1948.
- [64] D. R. Lide, editor. *CRC Handbook of Chemistry and Physics (60th Edition)*. Taylor and Francis, Boca Raton, FL, 1980.
- [65] A. W. Lohmann, H. Knuppertz, and J. Jahns. Fractional Montgomery effect: a self-imaging phenomenon. *Journal of the Optical Society of America A*, 22(8):1500–1508, 2005.
- [66] M. Lohmann, W.-R. Dix, J. Metge, and B. Reime. Instrumentation for diffraction enhanced imaging experiments at HASYLAB. *AIP Conf. Proc. SRI 03 San Francisco, California*, 705:392, 2004.
- [67] W. Machold, P. Staron, F. S. Bayraktar, S. Riekehr, M. Kocak, and A. Schreyer. Influence of the welding sequence on residual stresses in laser-welded T-joints of an airframe aluminium alloy. *Mater. Sci. Forum*, 571-572:375–380, 2008.

Bibliography

- [68] P. J. McMahon, A. G. Peele, D. Paterson, J. J. A. Lin, T. H. K. Irving, I. McNulty, and K. A. Nugent. Quantitative X-ray phase tomography with sub-micron resolution. *Optics Communications*, 217:53–58, 2003.
- [69] A. Momose. Demonstration of phase-contrast X-ray computed tomography using an X-ray interferometer. *Nuclear Instruments and Methods A*, 352:622–628, 1995.
- [70] A. Momose. Phase-sensitive imaging and phase tomography using X-ray interferometers. *Optics Express*, 11:2303–2314, 2003.
- [71] A. Momose. Recent advances in X-ray phase imaging. *Japanese Journal of Applied Physics*, 44:6355–6367, 2005.
- [72] W. D. Montgomery. Self-imaging objects of infinite aperture. *Journal of the Optical Society of America*, 57:772–778, 1967.
- [73] F. Natterer. *The Mathematics of Computerized Tomography*. Soc. for Industrial & Applied Math., 2001.
- [74] F. Neues, A. Klocke, F. Beckmann, J. Herzen, J.P. Loyola-Rodriguez, and M. Epple. Mineral distribution in highly fluorotic and in normal teeth: A synchrotron microcomputer tomographic study. *Mat.-wiss. u. Werkstofftech.*, 40(4):294–296, 2009.
- [75] M. Nickel, J. U. Hammel, J. Herzen, E. Bullinger, and F. Beckmann. High density resolution synchrotron radiation based X-ray microtomography (SR μ CT) for quantitative 3D-morphometrics in zoological sciences. *Proceedings of SPIE*, 7078:70781W1–11, 2008.
- [76] K. A. Nugent, T. E. Gureyev, D. F. Cookson, D. Paganin, and Z. Barnea. Quantitative phase imaging using hard x rays. *Physical Review Letters*, 77:2961–2964, 1996.
- [77] D. M. Paganin. *Coherent X-ray Optics*. Oxford University Press, New York, 2006.
- [78] K. Patorski. The self-imaging phenomenon and its applications. *Progress in Optics*, 27:1–108, 1989.
- [79] F. Pfeiffer, M. Bech, O. Bunk, P. Kraft, E. F. Eikenberry, C. Brönnimann, C. Grünzweig, and C. David. Hard-X-ray dark-field imaging using a grating interferometer. *Nature Materials*, 7:134–137, 2008.
- [80] F. Pfeiffer, O. Bunk, C. Kottler, and C. David. Tomographic reconstruction of three-dimensional objects from hard X-ray differential phase contrast projection images. *Nuclear Instruments and Methods in Physics Research*, A 580:925–928, 2007.
- [81] F. Pfeiffer, O. Bunk, T. Weitkamp, J. F. van der Veen, and I. K. Robinson. Shearing interferometer for quantifying the coherence of hard X-ray beams. *Physical Review Letters*, 94:164801, 2005.
- [82] F. Pfeiffer, C. Kottler, O. Bunk, and C. David. Hard X-ray phase tomography with low-brilliance sources. *Physical Review Letters*, 98:108105, 2007.
- [83] F. Pfeiffer, T. Weitkamp, O. Bunk, and C. David. Phase retrieval and differential phase-contrast imaging with low-brilliance X-ray sources. *Nature Physics*, 2:258, 2006.

- [84] E. F. Plechaty, D. E. Cullen, and R. J. Howerton. *Tables and graphs of photon-interaction cross sections from 0.1 keV to 100 MeV derived from the LLL evaluated-nuclear-data library*. Lawrence Livermore National Laboratory, 1981.
- [85] J. Regelsberger, T. Schmidt, B. Busse, J. Herzen, M. Tsokos, M. Amling, and F. Beckmann. Synchrotron-microcomputed tomography studies of normal and pathological cranial sutures: further insight. *Journal of Neurosurgery: Pediatrics*, 5(3):238–242, 2010.
- [86] W. Reimers, A. R. Pyzalla, A. Schreyer, and H. Clemens, editors. *Neutrons and Synchrotron Radiation in Engineering Materials Science*. Wiley-VCH, 2008.
- [87] E. Reznikova, J. Mohr, M. Boerner, V. Nazmov, and P.-J. Jakobs. Soft X-ray lithography of high aspect ratio SU8 submicron structures. *Microsystem Technologies*, 14:16831688, 2008.
- [88] C. Ritzoulis, M. Strobl, C. Panayiotou, G. Choinka, C. Tsiptsias, C. Vasiliadou, V. Vasiliakos, F. Beckmann, J. Herzen, and T. Donath. Ultra-small angle neutron scattering and x-ray tomography studies of caseinate-hydroxyapatite microporous materials. *Materials Chemistry and Physics*, 123(1):77 – 82, 2010.
- [89] J. D. Robson, N. Kamp, and A. Sullivan. Microstructural modelling for friction stir welding of aluminium alloys. *Materials and Manufacturing Processes*, 22:450–456, 2007.
- [90] T. Schmidt, J. Herzen, F. Beckmann, and J. Regelsberger. Micro-CT studies of normal and pathological cranial sutures - a new insight. *HASYLAB annual report*, 2007.
- [91] N. J. Schneiders and S. C. Bushong. Single-step calculation of the MTF from the ERF. *Medical Physics*, 5(1):31–33, 1978.
- [92] A. Snigirev, I. Snigireva, V. Kohn, S. Kuznetsov, and I. Schelokov. On the possibilities of x-ray phase contrast microimaging by coherent high-energy synchrotron radiation. *Rev. Sci. Instrum.*, 66:5486–5492, 1995.
- [93] H. F. Talbot. Facts relating to optical science. no IV. *Philosophical Mag., J. Sci.*, 9:401–407, 1836.
- [94] T. Weitkamp. XWFP: An X-ray wavefront propagation software package for the IDL computer language. *Proceedings of SPIE*, 5536:181–189, 2004.
- [95] T. Weitkamp, C. David, C. Kottler, O. Bunk, and F. Pfeiffer. Tomography with grating interferometers at low-brilliance sources. *Proceedings of SPIE*, 6318:63180S, 2006.
- [96] T. Weitkamp, A. Diaz, C. David, F. Pfeiffer, M. Stampanoni, P. Cloetens, and E. Ziegler. X-ray phase imaging with a grating interferometer. *Optics Express*, 13:6296–6304, 2005.
- [97] S. Wilkins, T. Gureyev, D. Gao, A. Pogany, and A. Stevenson. Phase-contrast imaging using polychromatic hard X-rays. *Nature*, 384:335–338, 1996.
- [98] K. Wille. *Physik der Teilchenbeschleuniger und Synchrotronstrahlungsquellen; Eine Einführung*. Teubner Verlag, 1996.
- [99] W. Yao and K. Leszczynski. Depth distribution of multiple order X-ray scatter. *Radiation Physics and Chemistry*, 77:381–390, 2008.

Bibliography

- [100] Z. Zhong, W. Thomlinson, D. Chapman, and S. Sayers. Implementation of diffraction-enhanced imaging experiments: at the NSLS and APS. *Nuclear Instruments and Methods in Physics Research A*, 450:556–567, 2000.

List of publications

- O. Brunke, K. Brockdorf, S. Drews, B. Müller, T. Donath, J. Herzen, and F. Beckmann. Comparison between X-ray tube based and synchrotron radiation based μ CT. *Proceedings of SPIE*, 7078:70780U1–12, 2008.
- M. Dalstra, P. M. Cattaneo, J. Herzen, and F. Beckmann. Visualizing the root-PDL-bone interface using high-resolution microtomography. *Proceedings of SPIE*, 7078:70780L1–10, 2008.
- S. Drews, F. Beckmann, J. Herzen, O. Brunke, P. Salmon, S. Friess, A. Laib, B. Koller, T. Hemberger, M. Müller-Gerbl, and B. Müller. Comparative micro computed tomography study of a vertebral body. *Proceedings of SPIE*, 7078:70780C1–14, 2008.
- A. Haibel, B. Beckmann, T. Dose, J. Herzen, S. Utcke, T. Lippmann, N. Schell, and A. Schreyer. The GKSS beamlines at PETRA III and DORIS III. *Proceedings of SPIE*, 7078:70780Z1–10, 2008.
- J. U. Hammel, J. Herzen, F. Beckmann, and M. Nickel. Sponge budding is a spatiotemporal morphological patterning process: Insights from synchrotron radiation-based X-ray microtomography into the asexual reproduction of *Tethya wilhelma*. *Frontiers in Zoology*, 6:19, 2009.
- J. Herzen, F. Beckmann, S. Riekehr, F. S. Bayraktar, A. Haibel, P. Staron, T. Donath, S. Utcke, M. Kocak, and A. Schreyer. SR μ CT study of crack propagation within laser-welded aluminum-alloy T-joints. *Proceedings of SPIE*, 7078:70781V, 2008.
- J. Herzen, T. Donath, F. Pfeiffer, O. Bunk, C. Padeste, F. Beckmann, A. Schreyer, and C. David. Quantitative phase-contrast tomography of a liquid phantom using a conventional X-ray tube source. *Optics Express*, 17(12):10010–10018, 2009.
- T. Kleinteich, Beckmann, J. Herzen, A. P. Summers, and A. Haas. Applying X-ray tomography in the field of vertebrate biology: form, function, and evolution of the skull of caecilians (Lissamphibia: Gymnophiona). *Proceedings of SPIE*, 7078:7078D1–10, 2008.
- F. Neues, A. Klocke, F. Beckmann, J. Herzen, J.P. Loyola-Rodriguez, and M. Epple. Mineral distribution in highly fluorotic and in normal teeth: A synchrotron microcomputer tomographic study. *Mat.-wiss. u. Werkstofftech.*, 40(4):294–296, 2009.
- M. Nickel, J. U. Hammel, J. Herzen, E. Bullinger, and F. Beckmann. High density resolution synchrotron radiation based X-ray microtomography (SR μ CT) for quantitative 3D-morphometrics in zoological sciences. *Proceedings of SPIE*, 7078:70781W1–11, 2008.
- M. Nickel, C. Scheer, J. U. Hammel, J. Herzen, and F. Beckmann. Evolution of body contractility in basal metazoans: contraction in porifera mediated by the pinacoderm. submitted to BMC Evolutionary Biology, June 2010.

List of publications

J. Regelsberger, T. Schmidt, B. Busse, J. Herzen, M. Tsokos, M. Amling, and F. Beckmann. Synchrotron-microcomputed tomography studies of normal and pathological cranial sutures: further insight. *Journal of Neurosurgery: Pediatrics*, 5(3):238–242, 2010.

C. Ritzoulis, M. Strobl, C. Panayiotou, G. Choinka, C. Tsiptsias, C. Vasiliadou, V. Vasiliakos, F. Beckmann, J. Herzen, and T. Donath. Ultra-small angle neutron scattering and x-ray tomography studies of caseinate-hydroxyapatite microporous materials. *Materials Chemistry and Physics*, 123(1):77 – 82, 2010.

B. Saldamli, J. Herzen, F. Beckmann, J. Tübel, J. Schauwecker, R. Burgkart, P. Jürgens, H.-F. Zeilhofer, R. Sader, and B. Müller. Internal structures of scaffold-free 3D cell cultures visualized by synchrotron radiation-based micro computed tomography. *Proceedings of SPIE*, 7078:70781X, 2008.

